
Electronic Thesis and Dissertation Repository

12-13-2019 10:30 AM

Numerical and Semi-Analytical Estimation of Convective Heat Transfer Coefficient for Buildings in an Urban-Like Setting

Anwar Demsis Awol, *The University of Western Ontario*

Supervisor: Bitsuamlak, Girma T., *The University of Western Ontario*

Co-Supervisor: Tariku, Fitsum, *British Columbia Institute of Technology*

A thesis submitted in partial fulfillment of the requirements for the Doctor of Philosophy degree in Civil and Environmental Engineering

© Anwar Demsis Awol 2019

Follow this and additional works at: <https://ir.lib.uwo.ca/etd>



Part of the [Architectural Engineering Commons](#), [Civil and Environmental Engineering Commons](#), [Computational Engineering Commons](#), [Fluid Dynamics Commons](#), [Heat Transfer, Combustion Commons](#), and the [Urban, Community and Regional Planning Commons](#)

Recommended Citation

Awol, Anwar Demsis, "Numerical and Semi-Analytical Estimation of Convective Heat Transfer Coefficient for Buildings in an Urban-Like Setting" (2019). *Electronic Thesis and Dissertation Repository*. 6750. <https://ir.lib.uwo.ca/etd/6750>

This Dissertation/Thesis is brought to you for free and open access by Scholarship@Western. It has been accepted for inclusion in Electronic Thesis and Dissertation Repository by an authorized administrator of Scholarship@Western. For more information, please contact wlsadmin@uwo.ca.

Abstract

Urban building arrangements such as packing density, orientation and size are known to influence the microclimate surrounding each building. Studies on the impact of urban microclimatic changes on convective heat transfer coefficient (CHTC) from a stock of buildings, however, have been rare in surveyed literature. The present study focusses on numerical and analytical investigation of CHTC from building-like models with homogeneous and quasi-heterogeneous arrangement of obstacles. Consequently, the study discusses the CHTC response in relation to broader changes in the urban surface form. Part of the process involves the development of a simplified one-dimensional semi-analytical CHTC model based on a simplified analytical mean wind velocity flow profile for urban canopies. The remaining portion consists of performing sets of CFD simulations to obtain CHTC values for a broader range of packing densities. Analysis and results of the study reveal that CHTC is affected both by changes in planar as well as frontal densities. These changes might lead to up to 2.5 times higher or approximately an order lower CHTC compared to the conventional u_{10} formulations (based on upstream reference conditions at 10 m from the ground), which are mostly done without considering packing density effects. It is observed that the least CHTC values lie at higher planar densities, whereas the highest CHTC corresponds to the combination of the lowest planar and highest frontal densities for the windward and leeward surfaces. An increase in planar area density increases the CHTC at smaller frontal densities for top and lateral surfaces. The study reveals the CHTC estimate from conventional models may have mostly been overestimated compared with

the values for buildings in city neighborhoods. New correlations for estimating CHTC for three canopy flow regimes are proposed. A relationship is also recognized between CHTC and the land-use class assignment of an urban neighborhood. The simplified analytical model, proposed correlations and the semi-analytical model are expected to enable estimation of CHTC for buildings located in urban neighborhoods based on the built area density or land-use class.

Keywords

Roughness sublayer flow (RSL), Canopy flow, Mean velocity profile, Wind speed, Urban microclimate, Flow regimes, Packing density, Frontal area density, Planar area density, Turbulence, Turbulence intensity, Convective heat transfer coefficient (CHTC), building energy consumption, Computational Fluid Dynamics (CFD).

Summary for Lay Audience

Building heating/cooling energy consumption saving measures help decrease the operating cost and tackle the issue of climate change through reducing greenhouse gas emission. An aspect of this saving strategy is the proper measurement of the various energy fluxes. One way a building loses energy is through convection. Convection is the energy the building loses when wind blows over its surface. As such, a high-intensity wind, thus, takes more heat than a low-intensity wind. However, wind effect on a building that is standing alone (or near few buildings) is different from a building that is surrounded by many nearby buildings. The strength of convective heat loss is often represented by a parameter known convective heat transfer coefficient (CHTC). This parameter is usually only related to the wind intensity (velocity). The current research attempts to develop an accurate estimate of this CHTC based on how buildings are packed (packing density) in a neighborhood, besides the wind speed. Through the findings of this research and the proposed correlations, one can now estimate CHTC (and hence convective heat loss) for buildings with various packing densities (neighborhoods such as residential, downtown, industrial, etc.).

Co-Authorship Statement

The thesis has been prepared as per the regulation for an Integrated-Article format thesis by the Graduate and Postgraduate studies, Western University and has been co-authored as:

Chapter 2: “A New analytical model for wind flow in sparse canopies” is submitted for publication to the Journal of Boundary Layer Meteorology under the co-authorship of Anwar D. Awol, Girma T. Bitsuamlak, and Fitsum Tariku.

Chapter 3: “Numerical estimation of external convective heat transfer coefficient for buildings in an urban-like setting” is submitted for publication to the Journal of Building and Environment under the co-authorship of Anwar D. Awol, Girma T. Bitsuamlak, and Fitsum Tariku.

Chapter 4: “Semi-analytical estimation of external convective heat transfer coefficient for buildings in an urban-like setting” is submitted for publication to the Journal of Building Physics under the co-authorship of Anwar D. Awol, Girma T. Bitsuamlak, and Fitsum Tariku.

Chapter 5: “External convective heat transfer coefficient for building-like stocks in quasi-heterogenous setting” is prepared for submission to the Journal of Building Performance Simulation under the co-authorship of Anwar D. Awol, Girma T. Bitsuamlak, and Fitsum Tariku.

To my respected parents.

To my inspirational Sisters and brothers.

To my darling wife, Shikuriyat.

To my adorable daughters, Alfiya and Neba.

Acknowledgment

First, I can't express my ultimate gratitude to the Almighty Allah for the strength and patience He gave me throughout.

I would like to express my earnest gratefulness to my supervisors Prof. Girma Bitsuamlak and Prof. Fitsum Tariku for their admirable supervision, guidance, and unmatched motivation during this study period. Their support, understanding, and encouragement throughout the process have been considerable assistance, and it will remain an inspiration in my future as well.

I would like to especially thank the Alan G. Davenport wind-engineering group, the Department of Civil and Environmental Engineering at Western University; its faculty and staff. Much appreciation goes to the research support from the Ontario Center of Excellence (OCE) through the Early Career Award, Natural Sciences and Engineering Research Council of Canada (NSERC) Collaborative Research Development, and the South Ontario Smart Computing Innovation Platform (SOSCIP) grants. I would like to thank the SharcNet and Compute/Calcul Canada for the High-Performance Computation (HPC) facility and excellent support from their technical staff.

I am grateful to all my friends and colleagues in our research team, who are still in Western or out, with whom I have had the pleasure to work during this program years. I am especially indebted to Tibebu and Dr. Meseret who have provided me extensive personal and professional support at various times.

Nobody has been more central to me in the pursuit of this endeavor than the members of my family here or elsewhere. I would like to thank my parents, sisters, and brothers; whose love and guidance are with me in whatever I pursue. Most importantly, I wish to thank my

supportive and loving wife, Shikuriya, and my two wonderful children, Alfiya and Neba, who provide me with unending inspiration.

Table of Contents

| | |
|--|-----|
| Abstract..... | ii |
| Summary for Lay Audience | iv |
| Co-Authorship Statement | v |
| Acknowledgment | vii |
| Table of Contents..... | ix |
| List of Tables | xi |
| List of Figures | xii |
| Nomenclature | xvi |
| Chapter 1..... | 1 |
| 1 Introduction | 1 |
| 1.1 Motivation..... | 1 |
| 1.2 Theoretical background | 2 |
| 1.3 Research gap | 11 |
| 1.4 Research scope | 13 |
| 1.5 Organization of the thesis..... | 14 |
| References | 16 |
| Chapter 2..... | 24 |
| 2 A new analytical model for wind flow in sparse canopies..... | 24 |
| 2.1 Introduction | 24 |
| 2.2 Model Derivation | 30 |
| 2.3 Validation of the model | 40 |
| 2.4 Discussion..... | 43 |
| 2.5 Conclusion..... | 45 |
| References | 46 |
| Chapter 3..... | 52 |
| 3 Numerical estimation of external convective heat transfer coefficient for buildings in an urban-like setting..... | 52 |
| 3.1 Introduction | 52 |
| 3.2 Computational evaluation of CHTC on building in urban-like setup | 59 |
| 3.3 CFD Validation..... | 67 |
| 3.4 Results and discussion | 75 |

| | | |
|-----------------------|--|-----|
| 3.5 | Conclusion..... | 87 |
| | References | 89 |
| Chapter 4..... | | 98 |
| 4 | Semi-analytical estimation of external convective heat transfer coefficient for buildings in an urban-like setting | 98 |
| 4.1 | Introduction | 98 |
| 4.2 | Semi-analytical CHTC model derivation..... | 103 |
| 4.3 | Verification of the model | 114 |
| 4.4 | Conclusion..... | 117 |
| | References | 118 |
| Chapter 5..... | | 127 |
| 5 | External convective heat transfer coefficient from surfaces of building stocks in quasi-heterogeneous setting..... | 127 |
| 5.1 | Introduction | 127 |
| 5.2 | Validation of the CFD model | 130 |
| 5.3 | Description of simplified quasi-heterogeneous urban model | 135 |
| 5.4 | Results and discussions..... | 142 |
| 5.5 | Discussion..... | 146 |
| 5.6 | Conclusion..... | 157 |
| | References | 158 |
| Chapter 6..... | | 165 |
| 6 | Conclusion and future work..... | 165 |
| 6.1 | Conclusion..... | 165 |
| 6.2 | Future work..... | 169 |
| Appendices..... | | 170 |
| Appendix A:..... | | 170 |
| Appendix B..... | | 172 |
| Curriculum vitae..... | | 172 |

List of Tables

| | |
|---|-----|
| Table 1.1 Flow regimes at different canopy density with a schematic description | 9 |
| Table 3.1 Flow regimes at different canopy density with a schematic description | 57 |
| Table 3.2 Density and size of cubes considered from each regime | 60 |
| Table 3.3 The equations required to fit the data in Figure 3.15..... | 79 |
| Table 3.4 The equations required to fit the data in Figure 3.19..... | 83 |
| Table 3.5 The equations required to fit the data in Figure 3.20..... | 84 |
| Table 3.6 Summary of proposed correlations | 85 |
| Table 3.7. A power-law expression for the test case at $\lambda = 0.075$ | 87 |
| Table 4.1 The equations required to fit the data in Figure 4.4..... | 113 |
| Table 4.2 Model constants for windward and top surfaces | 114 |
| Table 5.1 The sets of simulations conducted based on constant λ_p or λ_f | 137 |
| Table 5.2 Coefficients for the polynomials fit for the simulated CHTC data..... | 152 |
| Table 5.3 Practical frontal and planar density combinations of various neighborhoods of North American cities | 153 |

List of Figures

Figure 1.1 Convective flux from a hot surface (u and T are fluid velocity and temperature respectively; u_∞ and T_{ref} are reference free-stream velocity and temperature of the undisturbed flow) 3

Figure 1.2 Reference locations considered in various CHTC correlations..... 4

Figure 1.3 Existing CHTC correlations based on various reference velocities a) u_{10} , b) u_s , and c) u_H 5

Figure 1.4 Comparison CHTC from windward surfaces against CFD various studies..... 6

Figure 1.5 a) The urban boundary layers, b) local scale (adapted from Piringer et al. 2002), c) The upstream PBL profile, d) displaced log-law UBL profile and e) UBL and UCL profile (PBL: planetary boundary layer; UBL: urban boundary layer; UCL: urban canopy layer) 8

Figure 1.6 Description of areas used to determine a density parameter a) heterogeneous obstacles b) simplified homogeneous obstacles. 10

Figure 2.1 Packing density parametrization of idealized homogeneous canopy formed by a) plants b) buildings..... 25

Figure 2.2 Normalized canopy mean velocity profile generated by using a) Inoue’s model (Eq.1.2) b) Cowan’s model (Eq.1.3)..... 29

Figure 2.3 Normalized canopy mean velocity profile a) Inoue’s model (Eq. 2.1) b) Cowan’s model (Eq.2.7) c) present model (Eq.2.18) d) all models at selected values of the shear length scale 35

Figure 2.4 Plot of H/L_s from experimental data against frontal area density (data from Raupach et al. (1996), Novak et al. (2000), Poggi et al. (2004) and Pietri et al. (2009)). 36

Figure 2.5 Plot of ϕ from experimental data against frontal area density (data from Raupach et al. (1996), Novak et al. (2000), Poggi et al. (2004) and Pietri et al. (2009)). 38

Figure 2.6 Plot of drag coefficients, height averaged mean velocity from the current model and the exponentially fitted canopy flux parameter..... 39

Figure 2.7 Plot of normalized canopy mean velocity profile from experimental data (Poggi et al. 2004) against that of the present model, and sensitivity to +/- 33% of the λ_f 41

Figure 2.8 Comparison of normalized canopy mean velocity profile from the present analytical model with experimental data: a) Bohm et al. (2013), b) Brunet et al. (1994). 42

Figure 2.9 Sensitivity of the normalized mean velocity for three different densities with +/-10% variation in shear length scale, L_s/H 43

Figure 2.10 Sensitivity of the normalized mean velocity for three different densities at three z_o/H values (short and long dash: $z_o/H = 10^{-4}$, solid: $z_o/H = 10^{-5}$, dash: $z_o/H = 10^{-7}$). 43

| | |
|--|----|
| Figure 2.11 Sensitivity of the mean drag coefficient for different values of z_0/H | 44 |
| Figure 3.1 Description of areas used to determine a density parameter. | 58 |
| Figure 3.2 The building array with the study section (broken lines) and spacing parameters indicated on a) plan and b) elevation views. | 61 |
| Figure 3.3 The computational domain, its dimensions and boundary conditions (H height of cubic = 21.25 m)..... | 62 |
| Figure 3.4 The inlet profiles a) mean velocity and b) the principal components of Reynolds stress..... | 64 |
| Figure 3.5 Elevation view of a sample mesh section..... | 65 |
| Figure 3.6 The sensitivity of surface average CHTC for various grid resolution for all surface orientations | 66 |
| Figure 3.7 Schematic drawing of a) each cubical element, b) the setup of the experimental tunnel..... | 68 |
| Figure 3.8 a) The adopted mean inlet velocity, b) turbulent kinetic energy profiles (solid line: experimental data; broken line: from re-cycling method; symbol: input to CFD) ... | 71 |
| Figure 3.9 CFD implementation of the Meinders (1998) experimental setup a) the tunnel chamber b) each cubical shell element. | 71 |
| Figure 3.10 Comparison of simulated and experimental results along the paths: a) ABCD b) EFGHE | 72 |
| Figure 3.11 Comparison CHTC from windward surfaces against CFD studies by Kahsay et al. (2018), Montazeri et al. (2015), Defraeye et al. (2010), Blocken et al. (2009) | 74 |
| Figure 3.12 Velocity contours on vertical and horizontal section planes for $\lambda = 0.01$ | 75 |
| Figure 3.13 Velocity contours on vertical and horizontal section planes for $\lambda = 0.1$ | 77 |
| Figure 3.14 Velocity contours on vertical and horizontal section planes for the case of $\lambda = 0.25$ | 77 |
| Figure 3.15 Heat transfer coefficient versus wind speed for an isolated cube | 79 |
| Figure 3.16 CHTC variation on the windward surface of each cube at several densities from upstream to downstream (i.e., cube 1 - 14)..... | 81 |
| Figure 3.17 CHTC versus canopy density for each building surface | 82 |
| Figure 3.18 Contour plots of CHTC on surfaces of the cube at selected densities | 82 |
| Figure 3.19 Heat transfer coefficient versus wind speed in the isolated flow regime | 83 |
| Figure 3.20 Heat transfer coefficient versus wind speed in the interference and skimming flow regimes..... | 84 |
| Figure 3.21 CHTC plots based on the proposed correlation in Table 3.6 (all orientations) | 86 |

| | |
|---|-----|
| Figure 3.22 Power-law curve fit between CHTC and u_{10} for the test case $\lambda = 0.075$ (all surfaces) | 87 |
| Figure 4.1 Description of areas used to determine a density parameter | 100 |
| Figure 4.2 Iterative solution data and curve fit representation for z_{avg}/H Eq.4.23..... | 110 |
| Figure 4.3 Curve fit equation for u_H/u_{10} from CFD simulation | 111 |
| Figure 4.4 Heat transfer coefficient versus wind speed for an isolated cube | 113 |
| Figure 4.5 Comparison of CHTC data from model prediction and CFD simulation | 116 |
| Figure 4.6 The scatter plot for CHTC of two surfaces | 116 |
| Figure 4.7 Sensitivity of H/z_o on CHTC for the windward and top surfaces | 117 |
| Figure 5.1 Definitions of frontal and planar density a) the schematic heterogeneous form b) the simplified homogeneous representation | 129 |
| Figure 5.2 Schematic drawing of a) each cubical element, b) the setup of the experimental tunnel (plan view). | 131 |
| Figure 5.3 CFD implementation of the Meinders (1998) experimental setup a) the tunnel chamber b) each cubical shell element. | 132 |
| Figure 5.4 A) The adopted mean inlet velocity and B) turbulent kinetic energy profiles (solid line: data from the experiment; broken line: obtained from re-cycling method; symbol: input implemented in CFD) | 133 |
| Figure 5.5 Comparison of simulated and experimental results along the paths: a) ABCD b) EFGHE | 135 |
| Figure 5.6 plot of λ_p versus λ_f showing the extent of the simulation set conducted | 136 |
| Figure 5.7 The building array with the study section (broken lines) and spacing parameters indicated on a) plan and b) elevation views. | 139 |
| Figure 5.8 The computational domain, its dimensions, and boundary conditions (H height of cubic = 21.25 m)..... | 140 |
| Figure 5.9 The inlet profiles of mean velocity and the principal components of Reynolds stress..... | 141 |
| Figure 5.10 Elevation view of a sample mesh section..... | 142 |
| Figure 5.11 CHTC trend on each cube along the longitudinal direction for three densities in each category | 143 |
| Figure 5.12 CHTC trend per planar/frontal density at each frontal/planar density regime for all surfaces..... | 145 |
| Figure 5.13 CHTC trend per frontal density at each planar density regime for each surface..... | 146 |
| Figure 5.14 3D plots of CHTC for each surface per the value at the isolated condition | 147 |

| | |
|---|-----|
| Figure 5.15 Contour plots of CHTC for each surface per the value at the isolated condition | 148 |
| Figure 5.16 Contour plots of CHTC for each surface along with schematic representation densities at various corners | 150 |
| Figure 5.17 Contour and 3D plots of the global CHTC value per the value at the isolated condition | 151 |
| Figure 5.18 Contour plots of CHTC for each surface per the windward CHTC value at the same density..... | 151 |
| Figure 5.19 Plots practical frontal and planar density combinations of various city neighborhoods..... | 155 |
| Figure 5.20 CHTC plots for each surface and distribution of density of urban neighborhoods (by land-use class)..... | 156 |

Nomenclature

Abbreviations

| | |
|----------|---|
| ASHRAE | American Society of Heating, Refrigerating and Air-Conditioning Engineers |
| ESDU | Engineering Standard Data Unit |
| CFD | Computational Fluid Dynamics |
| CHTC | Convective Heat Transfer Coefficient |
| HPC | High-Performance Computing |
| RANS | Reynolds Averaged Navier-Stokes |
| LES | Large Eddy Simulation |
| 1D/2D/3D | One/Two/Three Dimensional |
| NSERC | Natural Sciences and Engineering Research Council of Canada |
| SOSCIP | South Ontario Smart Computing Innovation Platform |
| SharcNet | Shared Hierarchical Academic Research Computing Network |
| ABL | Atmospheric Boundary Layer |
| RSM | Reynolds Stress Model |
| WW | Windward Surface |
| LW | Leeward Surface |

symbols

| | |
|----------------------|--|
| A | Coefficient in turbulent intensity correlation |
| A_d | Unit underlying lot area on the ground surface (array of uniform buildings) |
| $A_{d,i}$ | Unit underlying lot area on the ground surface per each building in a group (non-uniform buildings) |
| A_F | Total sum of frontal surface areas of group of buildings |
| A_f | Frontal area (array of uniform buildings) |
| $A_{f,i}$ | Frontal area of each building in a group (non-uniform buildings) |
| A_P | Total sum of top surface areas of group of buildings |
| A_p | Planar area (array of uniform buildings) |
| $A_{p,i}$ | Planar area of each building in a group (non-uniform buildings) |
| A_1, A_2 and A_3 | Constants of the curve fit for L_s/H |
| a | Density parameter (general) |
| a_1 | coefficient in CHTC correlations |
| a_o | Vertically-uniform frontal density parameter |
| a_1 and a_2 | Curve fit constants for z_{ave}/H |
| B_1, B_2 and B_3 | Curve fit Constants for φ |
| b | Value of L_s/H corresponding to the aerodynamic roughness z_o/H , and without the urban scale canopy |
| C_s | Surface/orientation coefficient when building is in a dense building scenario |
| $C_{s,i}$ | Surface/orientation coefficient in isolated building scenario |
| C_d | Sectional drag coefficient (general) |
| C_{do} | Vertically-uniform sectional drag |

| | |
|------------------|---|
| C_μ | Constant related to the choice of turbulence models |
| C_{dH} | Drag coefficient based on velocity at the mean roughness height |
| $\overline{C_d}$ | Height averaged mean drag coefficient |
| D | Logarithmic displacement height |
| f | An arbitrary function dependent on λ only |
| f_D | Total sectional drag force per unit mass |
| G | Factor refers to the length scale alteration due to the presence of the canopy |
| G_H | Value of the canopy length scale contribution factor corresponding to H (top of the canopy) |
| g | An arbitrary function dependent on λ only |
| H | Canopy height or the mean roughness height |
| h_{dense} | CHTC at a given canopy density |
| h_{iso} | CHTC at the isolated building case |
| h | Surface averaged external convective heat transfer coefficient |
| I_u | Turbulent intensity |
| K | Thermal conductivity |
| k | Turbulent kinetic energy |
| l_m | Turbulent mixing length |
| L_{ii} | Component of length scale tensor |
| L | Turbulent length scale |
| L_s | Shear length scale |

| | |
|--------------|---|
| m | Exponent of u in CHTC correlations |
| Nu | Nusselt number |
| p | Pressure |
| Pr_t | Turbulent Prandtl number |
| Re | Reynolds number |
| S | Spacing between adjacent buildings/cubes |
| u_{10} | Velocity at 10 m height from ground |
| u' | Turbulent fluctuation velocities in the streamwise (x) direction |
| u | Time-averaged mean streamwise velocity |
| u_H | Velocity at mean roughness (canopy) height, H |
| $u_{10,met}$ | Velocity at 10 m from the ground at the measurement station |
| u_m | Dynamical velocity (the velocity scale corresponding to the eddy-viscosity) |
| u_* | Friction velocity |
| u_{ref} | Reference velocity measured at ζ_{ref} |
| $U(z)$ | Normalised mean stream-wise wind speed at location z from the ground |
| U_H | Normalised wind velocity at the canopy top ($z = H$) |
| u_i, u_j | Velocity components in the directions of i and j |
| u'_i, u'_j | Turbulent fluctuation velocities in i and j directions |
| U_{10} | Normalised velocity at 10 m height from ground at the measurement station |
| w' | Turbulent fluctuation velocities in the z (vertical) directions |

| | |
|------------|---|
| x_i, x_j | Components of the position vector in the i and j direction; |
| z | Vertical axis/distance from the ground |
| z_{10} | $z = 10$ m |
| z_0 | Aerodynamic roughness scale |
| H/z_0 | relative roughness scale, Jensen Number |
| z_{ref} | Reference height |

Greek letters

| | |
|----------------|---|
| α_1 | <i>Attenuation coefficient</i> introduced by Inoue |
| α_2 | <i>Attenuation coefficient</i> as per Cowan's Model |
| ρ | Density of air |
| ν | Kinematic viscosity |
| τ_t | Turbulent shear stress |
| τ_v | Surface shear term imparted by the fluid due to its molecular diffusivity |
| K | Eddy diffusivity |
| κ | von Karman constant |
| ϕ | Canopy flux parameter, $= u_* / u_H$ |
| λ_f | Frontal area density (frontal area index) |
| λ_p | Planar area density (planar area index) |
| λ | <i>Canopy density</i> (when $\lambda_f = \lambda_p$) |
| α | <i>Attenuation parameter</i> as per current Model |
| δ_{met} | Boundary layer thickness at the meteorological station |

| | |
|----------------|--|
| δ | Boundary layer thickness at the study building site |
| α_{met} | Power law wind profile exponent at the meteorological station site |
| α_s | Power law wind profile exponent at the study building site |
| ε | Dissipation rate |
| ζ | Distance from the ground normalized by H ; |
| ζ_o | Aerodynamic roughness height of the flow normalized by H |
| ζ_{ref} | Reference height (commonly 10 m above ground) |
| θ | Temperature |
| θ^* | Dynamical temperature scale (i.e., the temperature variance normalized by the friction velocity) |
| θ_{ref} | Reference temperature measured at the location of reference |

Subscripts

| | |
|--------------|--|
| $s,$ | subscript, is for values at the surface of the bluff body |
| $i,$ | subscript, longitudinal (streamwise) direction |
| $j,$ | subscript, vertical (normal to the ground) direction, |
| <i>local</i> | refers to the values of the terms at a specific location in the canopy |
| <i>avg</i> | represents canopy average values of the variables |
| ref | for values reference location |
| met | for values at the metrological measurement location |
| iso | for isolated building case |
| dense | for dense building case |
| p | Planar |
| f | Frontal |

Chapter 1

1 Introduction

1.1 Motivation

In recent decades, building performance research has been one of the major areas of interest due to heightened demand for sustainability and energy use awareness. A World Bank report shows 70% of the greenhouse gas emission is caused in cities (UN-Habitat 2011). In North America, more than 30% and in Europe more than 50% of the energy produced each year is consumed in buildings respectively. Of this, over 50% is for conditioning of spaces. As UN report indicates, more than 66% of the world population starts to live in urban places by 2050 (UN - DESA 2018). The International Energy Agency (IEA 2011) declares energy use in buildings is expected to double by 2050 unless effective remedial actions are taken. Bordass and Leaman (2013) indicated that there is still ‘disappointing disparity’ between energy performance evaluations performed during buildings’ operation against performance predictions at the design stage.

An aspect of the effort to improve energy modeling in buildings is through finding consistent convective heat transfer coefficient (CHTC) of the building surfaces that allows for flexibility due to changes in the local microclimate. A feature of the urban surface form is how it transforms the upstream wind flow into a specific airflow flow field near buildings. Oke (1988) identified different flow regimes corresponding to varying levels of aggregation between idealized building-like obstacles. Therefore, the urban surface form

is a contributing factor to the variations in CHTC (Lui et al. 2013) in different sections of urban places.

1.2 Theoretical background

1.2.1 Convective heat transfer

The convective heat flux from a surface is, generally, accounted for using Newton's law of cooling. i.e.,

$$q'' = h (T_s - T_{ref}) \quad \text{Eq.1.1}$$

where q'' is the convective heat flux from the surface [w/m^2]; h is the CHTC [w/K.m^2]; T_s is temperature of the surface, and T_{ref} is the reference temperature. The CHTC characterizes the thermal resistance of the fluid layer near the surface. It is usually determined from controlled experiments or numerical simulations with given heat flux and $\Delta T (= T_s - T_{ref})$. This resistance term forms part of the overall thermal resistance of the building system, in combination with the conductive resistance of the thermal massing of the building.

The convective heat transfer coefficient can be related to the velocity and temperature profiles (Figure 1.1) in the near-wall fluid film through Fourier's law of heat conduction. i.e.,

$$q'' = k_f dT/dy \quad \text{Eq.1.2}$$

where k_f is the thermal conductivity of the fluid film, and y is a distance normal to the surface.

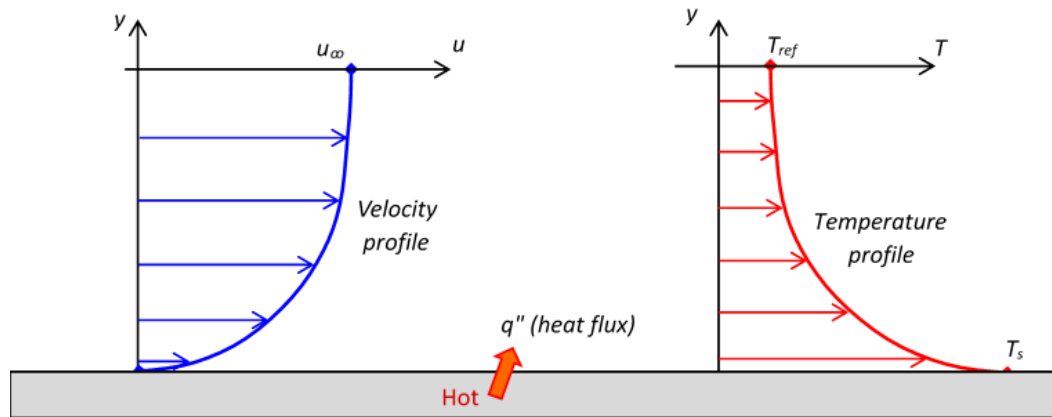


Figure 1.1 Convective flux from a hot surface (u and T are fluid velocity and temperature respectively; u_∞ and T_{ref} are reference free-stream velocity and temperature of the undisturbed flow)

1.2.2 CHTC correlations for buildings

Experimental and CFD studies on CHTC from building surfaces has resulted in dozens of correlations that are currently in use (Mirsadeghi et al. 2013, Defraeye et al. 2011, and Palyvos 2008). In general, the CHTC is related to the wind velocity by a power-law relation. However, there are some earlier exceptions (Palyvos 2008) that put the relationship as linear (especially for models with natural convection).

Surveyed literature indicates there is notable variability in the value of CHTC obtained from different correlations. The variability is often associated with the specificity of the model/full-scale experimental conditions (Evangelisti et al. 2017, Mirsadeghi et al. 2013, Defraeye et al. 2011, Emmel et al. 2007); or changes in the local microscale from the upstream reference states (Chen et al. 2017). Hence, some studies adopted a local reference scale as shown in Figure 1.2 (a given distance near an elevation or a roof surface). However,

the results obtained from this effort do still have disagreements. Figure 1.3 indicated plots of various correlations against adopted reference velocities; u_s on the side of an elevation surface, u_R above the roof surface and u_H at the building height. The plots indicate the inconsistency among reported correlations for CHTC from building surfaces.

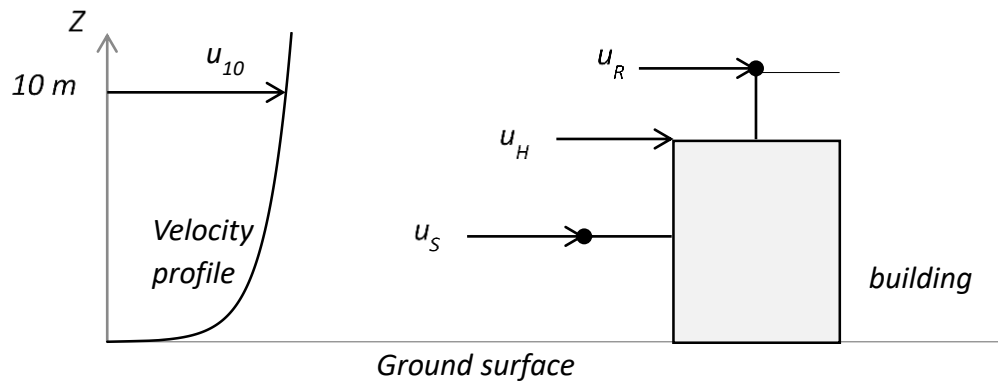
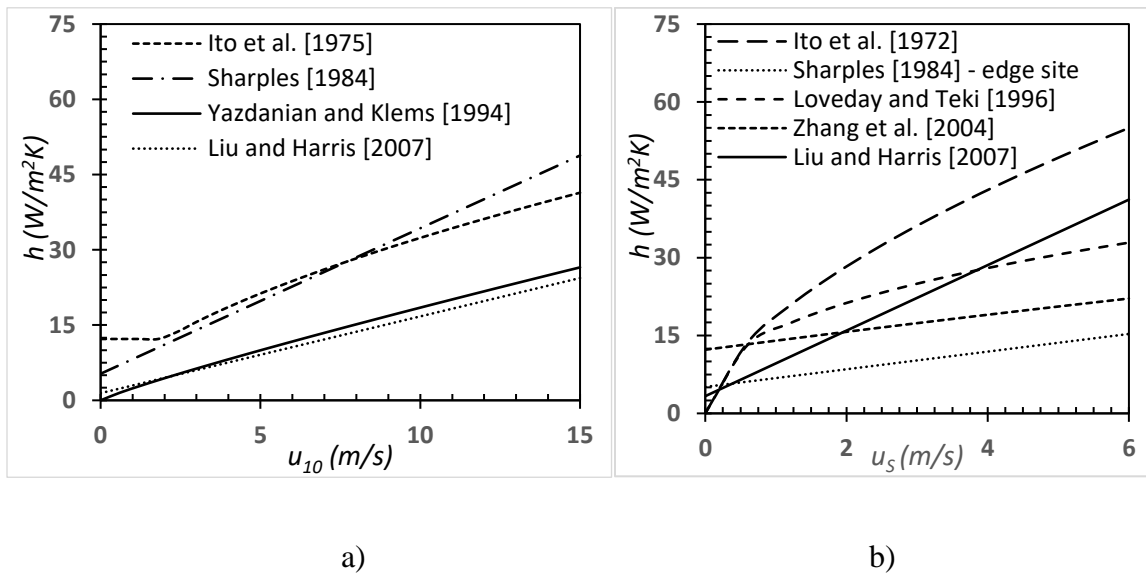
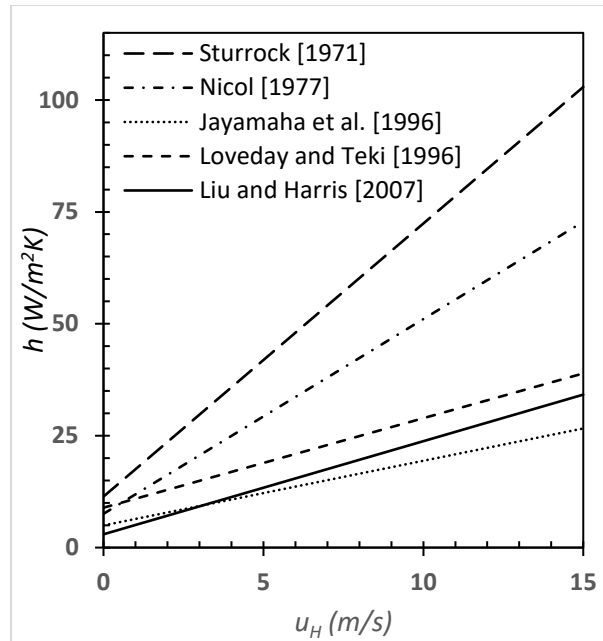


Figure 1.2 Reference locations considered in various CHTC correlations



a)

b)



c)

**Figure 1.3 Existing CHTC correlations based on various reference velocities a) u_{10} ,
b) u_s , and c) u_H**

CFD has been used as an alternative means in the estimation of the CHTC, besides the experimental methods. It is becoming a promising method of analysis because of the challenges in conducting experiments, as well as, recent improvements in computational resources. The potential and challenges of using CFD for building science applications have been discussed in Blocken (2015), and Murakami (1998). Validated CFD has been used in several recent articles in the determination of CHTC for building surfaces at different conditions (Figure 1.4), which include the impact of magnitude of wind speed (Defraeye et al., 2010, Blocken et al. 2009, Emmel et al., 2007), wind angle of attack (Blocken et al. 2009), building dimensions (Montazeri et al. 2017 and Khasay et al. 2018) and urban surroundings (Liu et al., 2013).

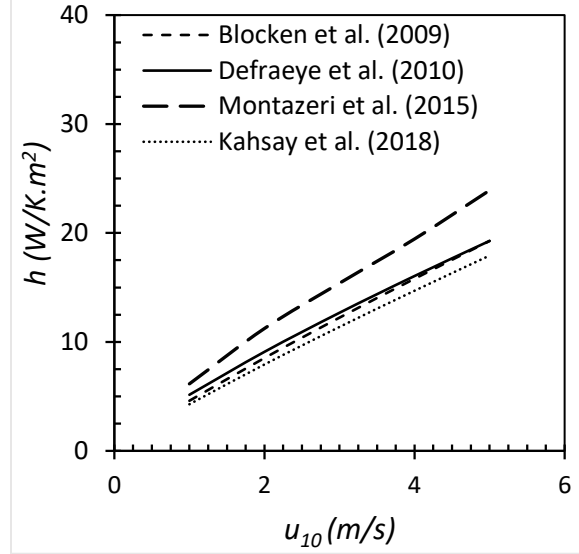


Figure 1.4 Comparison CHTC from windward surfaces against CFD various studies

1.2.3 RSM turbulence model

The second-moment turbulent closure scheme, Reynolds stress turbulence (RSM), has superiority over the other two-equation closure models for flows with significant secondary flow and extensive anisotropy (Speziale 1995, Speziale 1991, Murthy et al. The steady Reynolds average Navier-Stokes (RANS) equation can be solved by using Reynolds stress turbulence (RSM) closure scheme, and the continuity equation.

$$\frac{\partial \bar{u}_i}{\partial x_i} = 0, \quad \frac{\partial u'_i}{\partial x_i} = 0 \quad \text{Eq.1.3}$$

$$\bar{u}_i \frac{\partial \bar{u}_j}{\partial x_i} = -\frac{1}{\rho} \frac{\partial \bar{p}}{\partial x_j} + \frac{\partial}{\partial x_i} \left(\nu \frac{\partial \bar{u}_j}{\partial x_i} - \overline{u'_i u'_j} \right), \quad i, j = 1, 2, 3 \quad \text{Eq.1.4}$$

where u is the instantaneous velocity of the flow, u' is the fluctuation velocity, an overbar signifies a time averaged value. p is the pressure, ν is the kinematic viscosity, ρ is the density of air; and i and j are the component directions. In this method, a separate

conservation equation is solved for each component of the Reynolds stress tensor, $R_{ij} = \overline{u'_i u'_j}$.

In heat transfer applications, the energy equation needs to be coupled with the above system. i.e.,

$$\frac{\partial(\bar{u}_i \bar{T})}{\partial x_j} = \frac{\nu}{Pr} \frac{\partial^2 \bar{T}}{\partial x_i \partial x_j} - \overline{u'_i T'}, \quad i, j = 1, 2, 3 \quad \text{Eq.1.5}$$

where T is the temperature, and T' is the temperature fluctuation, and the turbulent heat flux, $\overline{u'_i T'}$, often modeled as: $\overline{u'_i T'} = \frac{\nu}{Pr_t} \frac{\partial \bar{T}}{\partial x_j}$. Where Pr_t is the turbulent Prandtl number commonly taken as a constant.

1.2.4 Urban canopy flow

The urban canopy layer (UCL) refers to the layer of flow roughly under the average roughness height of the urban roughness (buildings and vegetation). The planetary boundary layer (PBL) has an inertial layer (IL) starting closer to the ground and is generally represented by the log-law profile. This inertial layer is pushed up in urban spaces, and hence the mean velocity is a vertically displaced-logarithmic profile (i.e., the upper portion of the urban boundary layer - UBL). Transport in the lower part of the surface layer is associated with a drop in the mean flow speed due to the obstacle roughness. Measurement in this range is very challenging due to intensified mixing and turbulence, with reduced mean velocity (Raupach et al. 1996; Macdonald 2000). Often, the mean flow profile in this regime is obtained from simplified one-dimensional models. Figure 1.5 shows the different parts of the atmospheric boundary layer near urban spaces (Piringer et al. 2002) and some of the mean velocity profiles considered.

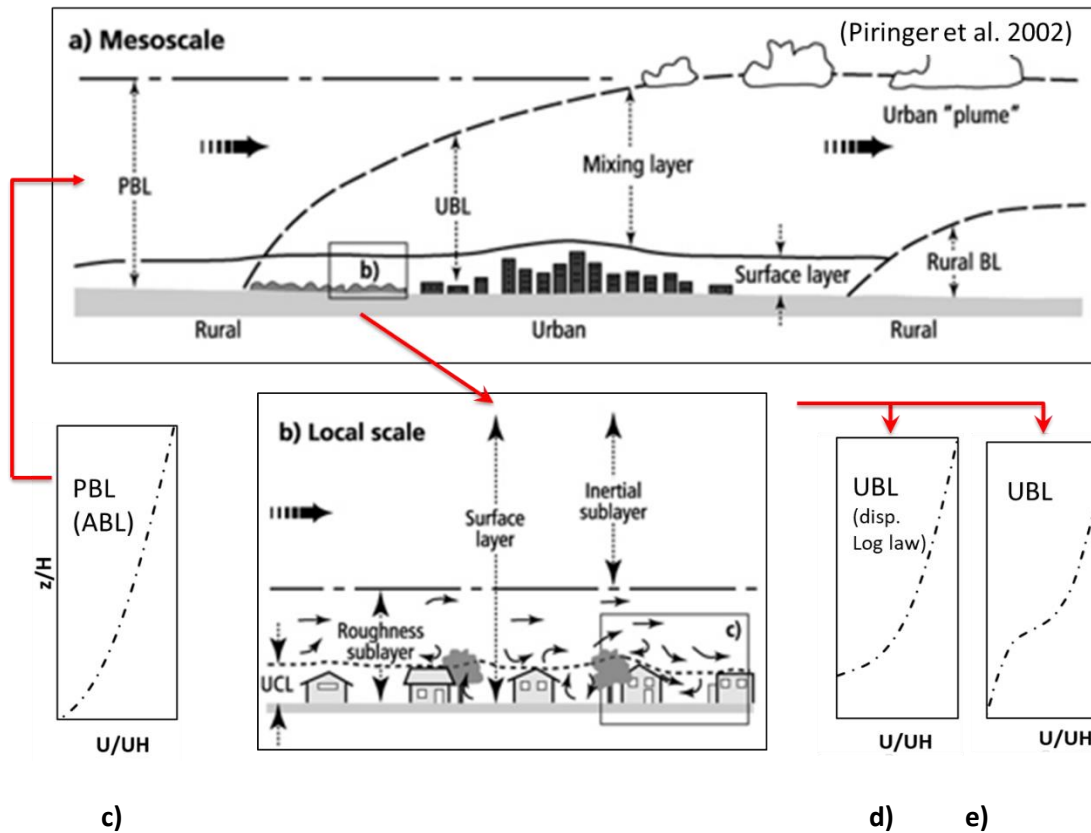


Figure 1.5 a) The urban boundary layers, b) local scale (adapted from Piringer et al. 2002), c) The upstream PBL profile, d) displaced log-law UBL profile and e) UBL and UCL profile (PBL: planetary boundary layer; UBL: urban boundary layer; UCL: urban canopy layer)

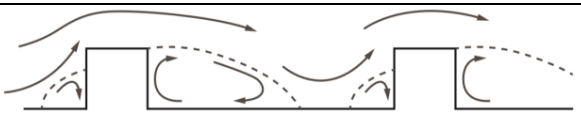
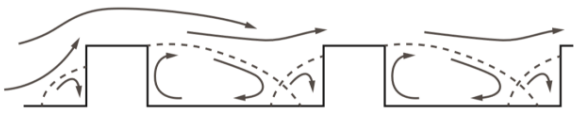
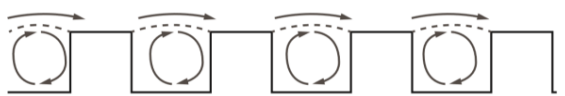
1.2.5 Flow past stoke of building-like obstacles

In a pioneer work by Oke (1988), the flow around a pack of idealized buildings is studied. Oke (1988) identified three distinct regimes of flow, having different flow structures based on proximity between the various obstacles. The first being where the spacing between buildings can be very large compared to the height (i.e., $H / S < 0.2$), in which case the wake from one of the obstacles hardly influences the flow around an obstacle downstream.

In this case, called an isolated roughness regime, the flow field starts to gradually change from that of around a purely isolated obstacle. The second flow regime is called wake interference. In this case, there is significant interaction from the wake of an obstacle on an obstacle downstream; and this condition is distinguished by pronounced mass exchange (besides momentum / turbulent shear) between the flow under the canopy and the one over it. In the third regime, the flow above the canopy skims over the obstacles and there exists a counter-current vortex trapped in the spaces between the obstacles. Exchanges in momentum due to turbulent shear at the top of the canopy are believed to drive the counter-flow under the canopy. Table 1.1 shows a summary of the flow regimes at different canopy density with schematic descriptions.

Packing density has been used as an expression of aggregation of an urban built system. There are two ways in which packing density has been defined, namely the frontal and planar forms of aggregation.

Table 1.1 Flow regimes at different canopy density with a schematic description

| H/S | Flow regime (Oke 1988) | Schematic description |
|--------------------|---------------------------|--|
| $H/S < 0.2$ | Isolated roughness |  |
| $0.2 < H/S < 0.65$ | Wake interference |  |
| $H/S > 0.65$ | Skimming |  |

The presence of bluff bodies in urban environments is commonly simulated in research by idealized roughness elements, an array of the inline or staggered arrangement of small-scale objects (e.g., cubes) mounted on a wall. Here the cube heights are meant to represent the average height of the roughness. Most of these investigations are laboratory experiments (Yang et al. 2016, Macdonald 2000, Cheng et al. 2002) and some CFD simulations (Castro 2017, Yang et al. 2016, Abdi and Bitsuamlak 2016, 2014, and Coceal et al. 2006).

Figure 1.6 and Eq.1.6 and Eq.1.7 show the frontal and planar density; and how the real urban form is translated into simplified homogeneous built arrays.

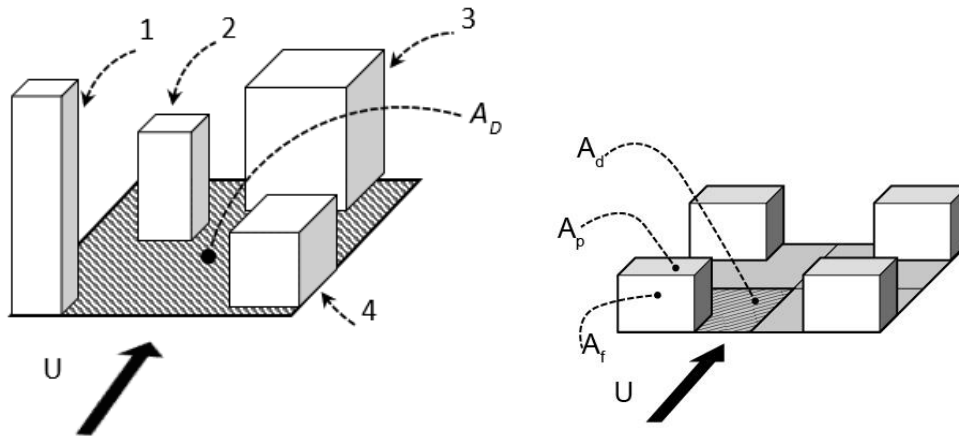


Figure 1.6 Description of areas used to determine a density parameter a) heterogeneous obstacles b) simplified homogeneous obstacles.

$$A_D = \sum_1^n A_{d,i} \quad \text{Eq.1.6}$$

$$\lambda_f = \frac{\sum_1^n A_{f,i}}{A_D} = \frac{A_F}{A_D}, \quad \lambda_p = \frac{\sum_1^n A_{p,i}}{A_D} = \frac{A_P}{A_D} \quad \text{Eq.1.7}$$

where $A_{f,i}$ is the frontal area per each building, $A_{p,i}$ is the planar, and $A_{d,i}$ is the unit underlying lot area on the ground surface per each building. The representative frontal and planar area densities at the neighbourhood level are, then, found from the ratio of the total frontal (A_F) and the total top (A_P) surface areas for the total lot area, respectively. These kinds of idealizations have helped drive mean velocity profiles for the urban and vegetated canopy layer (Inoue 1965, Cowan 1968, Wang 2012).

1.3 Research gap

Chen et al. (2017) conveyed that the most important sources of uncertainty in realizing building energy performance are the local microclimatic properties and the resulting CHTC from the building surfaces. Significant variations that exist in measured and simulated CHTC correlations are mostly attributed to the specificity of the studies (Evangelisti et al. 2017, Mirsadeghi et al. 2013, Defraeye et al. 2011, Emmel et al. 2007). The largest CHTC from one source could be 5 to 10 times the smallest in another source, for similar wind speed values (1 - 2m/s), based on models derived existing from field and lab experiments (Chen et al. 2017). This variation further widens as the wind speed becomes higher or the study building is in urban areas. The uncertainty related to microclimatic changes in urban spaces arises from the deviation of actual flow parameters at the urban site in relation to the records at the meteorological station, commonly located at airports. Surrounding terrain difference, building forms, and building arrangements affect the local urban microclimate (Moonen et al. 2012, Blocken et al. 2011, van Hoof et al. 2010, Franke et al. 2007, Coceal et al. 2004, Macdonald 2000, Stathopoulos et al. 1995, Oke 1988). Adamek et al. (2017)

have shown how a city development and related urban topology change affect microclimate near buildings.

The variation of urban morphology (as expressed by packing density) results in changes in the value of CHTC measured from building surfaces (Liu et al. 2013). However, most existing models used for estimating CHTC are derived from studies on isolated bluff body by using either CFD studies (Montazeri et al. 2015, Blocken et al. 2009, and Emmel et al. 2007) or scaled experiments (Nakamura et al. 2001, Natarajan et al. .1994; Meinders et al. 1999, Chyu et al. 1991). The effect of sheltering from neighboring buildings has only been considered in site/configuration-specific studies (Mirsadegi et al. 2013, Liu et al. 2015, Allegrini et al. 2012, Liu et al. 2007). Discussion of microclimatic changes due to perturbations of urban packing density (the nature of aggregation of the built system) is widely available (Castro 2017, Coceal et al. 2004, Macdonald 2000, Oke 1988). Researchers in urban canopy and plant canopy fields have also widely reported that the velocity profile in canopies (urban and plant) does not follow the power-law or log law form (Awol et al. 2017, Wang 2014, Coceal et al. 2004, Cheng et al. 2002, Macdonald 2000, Cowan 1968, Cionco 1965). These studies show spatially averaged velocity profile in urban canopies is dependent on the density of the urban arrangement.

The first attempt to relate urban packing density to convective heat transfer has been made by Lui et al. (2013). Lui et al. (2013) used upstream flow parameters derived for buildings placed in an urban setting, which are specifically represented by arrays of cubes. They used modified aerodynamic roughness values proposed by Macdonald (2000). However, the aerodynamic roughness values, along with the displacement height values proposed by Macdonald (2000) were to improve the estimation of the mean velocity profile in the

inertial range. The two parameters (i.e., aerodynamic roughness, and the displacement height) help obtain a displaced logarithmic mean velocity profile that better fits to the velocity profile above the canopies. With the use of these parameters, the canopy layer velocity profile may not be properly reproduced. Moreover, the use of different upstream aerodynamic roughness values and hence different upstream mean velocity profiles makes the comparison of results problematic.

The current research work intends to perform numerical analysis of CHTC from buildings located amidst an urban building stock with consistent boundary conditions.

1.4 Research scope

The thesis aims to address the research gaps stated in the section above. Accordingly, the objectives of the research are enlisted hereunder.

- Develop a numerical model for CHTC from homogeneous (equal planar and frontal densities) set of buildings in an urban-like setting
- Validate model against small scale experimental and full-scale CFD data
- Develop a simplified analytical model of wind flow in urban canopies
- Develop a simplified analytical model of CHTC from windward and top surfaces of the building in an urban-like setting
- Perform numerical analysis of CHTC from quasi-heterogeneous (unequal planar and frontal densities) set of buildings in an urban-like setting
- Analysis of CHTC from buildings located in various land-use class

1.5 Organization of the thesis

This thesis has been prepared in an “Integrated-Article” format. In Chapter 1, a review of studies on the existing-CHTC models, their effect on building energy performance, and their lack thereof in relation to urban microclimates are provided. The objectives of the thesis are addressed in detail in the following four chapters.

1.5.1 A new analytical model for wind flow in sparse canopies

In chapter 2, a new analytical model is developed for wind flow in homogenous sparse canopies by assuming that the ratio of the local Reynolds stress to the square of local space-averaged mean velocity does not vary much from the corresponding value at the top of the canopy. A tractable mathematical model is obtained after linearization of the drag parameter. The resulting new mean velocity profile predicts the near ground velocity as per the atmospheric boundary layer (ABL) profile conditions, matches the ABL conditions in the absence of plant/urban canopies. The validity of this model is ascertained by comparing it against experimental results from literature.

1.5.2 Numerical estimation of external convective heat transfer coefficient for buildings in an urban-like setting

In chapter 3, CFD simulation of flow over arrays of various packing and heated cubical buildings are simulated to investigate the effect of aggregation or rarefaction of stoke of building on the CHTC from the building surfaces. The simulation process is validated against a model scale experiment and a full-scale CFD simulation. The results indicate the CHTC trend varies in different regimes of flow. In the isolated roughness regime, the

CHTC shows a sharp change with changes in density. However, In the interference and skimming flow regimes, the CHTC decreases gradually with increasing packing density.

New correlations are presented.

1.5.3 Semi-analytical estimation of external convective heat transfer coefficient for buildings in an urban-like setting

In Chapter 4, a semi-analytical CHTC model is derived based on existing CHTC models, and a canopy level mean velocity profile. The derivation involves the adoption of a local characteristic velocity for mean wind flow in canopies corresponding to the local microclimate. The resulting model is assessed against CFD simulation data; and results of the model show a good match with the CFD data.

1.5.4 External convective heat transfer coefficient for building-like stocks in quasi-heterogeneous setting (unequal frontal and planar urban density arrangements)

In Chapter 5, an investigation is conducted to determine whether variability in planar and frontal densities of stock of buildings affects the CHTC from a building surface. To this end, sets of simulations are conducted on building-like obstacles modeled based on planar – frontal density matrix. The results indicated both frontal and planar densities have an effect on CHTC. Moreover, the resultant CHTC surface at a given reference wind velocity reveals how each surface is affected by the two densities. It is observed that the least CHTC values lie at higher planar densities, whereas the highest CHTC corresponds to the combination of the lowest planar and highest frontal densities for the windward and leeward surfaces. An increase in planar area density increases the CHTC at smaller frontal

densities for top and lateral surfaces. The study reveals the CHTC estimate from conventional models may have mostly been overestimated from the real values for buildings in city neighborhoods. New correlations for estimating CHTC in the flow three canopy flow regimes are proposed. A relationship is also recognized between CHTC and the land-use class assignment of an urban neighborhood.

Finally, in Chapter 6, the overall conclusion of the present study and avenues of future research are discussed.

References

Abdi, D. and Bitsuamlak, G.T. (2016). Wind flow simulations in idealized and real built environments with models of various levels of complexity, *Wind & Structures*, 22 (4): 503-524.

Abdi, D. and Bitsuamlak, G.T. (2014). Numerical evaluation of the effect of multiple roughness changes. *Wind and Structures*, 19(6): 585-601.

Adamek, K., Vasan, N., Elshaer, A., English, E., and Bitsuamlak, G.T. (2017). Pedestrian level wind assessment through city development: A study of the financial district in Toronto, *Sustainable Cities and Societies*, 35:178-190.

Allegrini, J., Dorer, V. Carmeliet, J. (2012). Analysis of convective heat transfer at building façades in street canyons and its influence on the predictions of space cooling demand in buildings, *J. Wind Eng. Ind. Aerod.* 104:464-473.

Awol, D.A., Bitsuamlak, G.T., Tariku, F. (2017). Consistent analytical urban canopy layer velocity profile for dense building arrangement. Americas Conference on Wind Engineering, Gainesville, United States, 21-24 May 2017

Blocken, B. (2015) 50 years of computational wind engineering: past, present and future, *J. Wind Eng. Ind. Aerodyn.* 129:69-102.

Blocken, B., Defraeye, T. Derome, D. Carmeliet, J. (2009). High-resolution CFD simulations for forced convective heat transfer coefficients at the facade of a low rise building, *Build. Environ.* 44:2396-2412.

Blocken, B., Stathopoulos, T., Carmeliet, J., Hensen, J.L.M. (2011). Application of computational fluid dynamics in building performance simulation for the outdoor environment: an overview, *Journal of Building Performance Simulation* 4:157-184.

Bordass B., Leaman, A. (2013). A new professionalism: remedy or fantasy?, *Building Research & Information*, 41:1, 1-7.

Castro, I.P. (2017) Are Urban-Canopy Velocity Profiles Exponential? *Boundary-Layer Meteorol* 164(3):337–351. DOI 10.1007/s10546-017-0258-x

Chen L., Hang J., Sandberg M., Claesson L., Di Sabatino S., Wigo H. (2017). The impacts of building height variations and building packing densities on flow adjustment and city breathability in idealized urban models, *Build. Environ.*; 118:344-361

Chen, L., Hang, J., Sandberg, M., Claesson, L., Di Sabatino, S., Wigo, H. (2017). The impacts of building height variations and building packing densities on flow adjustment and city breathability in idealized urban models, *Build. Environ*; 118:344-361

Cheng, H., Castro, I.P. (2002). Near-wall flow over urban-like roughness. *Boundary-Layer Meteorol* 104(2): 229–259

Chyu, M.K., Natarajan, V. (1991). Local heat/mass transfer distributions on the surface of a wall-mounted cube, *Trans. ASME J. Heat. Transf.* 113:851-857.

Cionco, R.M. (1965). Mathematical Model for Air Flow in a Vegetative Canopy. *J. Applied Meteorol.* 4:517–522

Coceal, O., Belcher S.E. (2004). A canopy model of mean winds through urban areas. *Q J Roy Meteorol Soc* 130(599):1349–1372

Coceal, O., Thomas, T.G., Castro, I.P., Belcher, S.E. (2006). Mean flow and turbulence statistics over groups of urban-like cubical obstacles. *Boundary-Layer Meteorol* 121:491-519

Cowan, I.R. (1968). Mass, heat and momentum exchange between stands of plants and their atmospheric environment. *Q J Roy Meteorol Soc* 94:523–544

Defraeye, T., Blocken, B., Carmeliet, J. (2011). Convective heat transfer coefficients for exterior building surfaces: Existing correlations and CFD modelling, *Energy Conversion and Management* 52:512–522

Defraeye, T., Blocken, B., Carmeliet, J. (2010). CFD analysis of convective heat transfer at the surfaces of a cube immersed in a turbulent boundary layer, *Int. J. Heat. Mass Transf.* 53:297-308.

Emmel, M.G., Abadie, M.O., Mendes, N. (2007). New external convective heat transfer coefficient correlations for isolated low-rise buildings, *Energ Build.* 39:335-342.

Evangelisti, L., Guattari, C., Gori, P., Bianchi, F. (2017). Heat transfer study of external convective and radiative coefficients for building applications, *Energ Build.* 151:429–438

Franke, J., Hellsten, A., Schlünzen, H., Carissimo B. (Eds.) (2007). Best practice guideline for the CFD simulation of flows in the urban environment, COST Office, Brussels, 3-00-018312-4.

van Hooff, T., Blocken, B. (2010). On the effect of wind direction and urban surroundings on natural ventilation of a large semi-enclosed stadium, *Computers & Fluids* 39:1146-1155.

Inoue E (1963) On the turbulent structure of air flow within crop canopies. *J Meteorol Soc Jpn* 41:317–326

IEA (2011). *Energy Technology Perspectives 2010 Findings*. Grantham Institute/International Energy Agency Workshop: The Reduction of Global Carbon Emissions in the Building Sector to 2050. London, U.K.

Ito, N., Kimura, K., Oka, J. (1972). Field experiment study on the convective heat transfer coefficient on exterior surface of a building, *ASHRAE Trans.* 78:184-192.

Jayamaha, S.E.G., Wijesundera, N. E., Chou, S. K. (1996) Measurement of the heat transfer coefficient for walls, *Build. Environ.*, 31:399-407.

Kahsay, M.T., Bitsuamlak, G.T., Tariku F. (2018). Numerical analysis of convective heat transfer coefficient for building facades. *Journal of Building Physics*, 10.1177/1744259118791207.

photovoltaic/thermal systems, *Appl. Therm. Eng.* 31:1950-1963.

- Launder, B., Reece, G. J., Rodi, W. (1975). Progress in the Development of a Reynolds Stress Turbulence Closure, *J Fluid Mech.* 68(3):537 – 566
- Leschziner, M.A. (1990). Modelling engineering flows with Reynolds stress turbulence closure, *J. Wind Eng. Ind. Aerodyn.* 35:21-47.
- Liu, J., Heidarinejad, M., Gracik, S. Srebric, J. (2015). The impact of exterior surface convective heat transfer coefficients on the building energy consumption in urban neighborhoods with different plan area densities, *Energ Build.* 86:449-463.
- Liu, J. Srebric, J. Yu, N. (2013). Numerical simulation of convective heat transfer coefficients at the external surfaces of building arrays immersed in a turbulent boundary layer, *Int. J. Heat. Mass Transf.* 61:209-225.
- Liu, Y., Harris, D.J. (2007). Full-scale measurements of convective coefficient on external surface of a low-rise building in sheltered conditions, *Build. Environ.* 42:2718-2736.
- Loveday, D.L., Taki, A.H. (1996). Convective heat transfer coefficients at a plane surface on a full-scale building facade, *Int. J. Heat. Mass Transf.* 39:1729-1742.
- Macdonald, R.W. (2000). Modelling the mean velocity profile in the urban canopy layer. *Boundary Layer Meteorol* 97(1):25–45
- Meinders, E.R., Hanjalic, K., Martinuzzi, R.J. (1999). Experimental study of the local convection heat transfer from a wall-mounted cube in turbulent channel flow, *Trans. ASME J. Heat. Transf.* 121:564-573.

Mirsadeghi, M., Costola, D., Blocken, B., Hensen, J.L.M. (2013). Review of external convective heat transfer coefficient models in building energy simulation programs: implementation and uncertainty, *Appl. Therm. Eng.* 56:134-151.

Montazeri, H., Blocken, B., Derome, D., Carmeliet, J., Hensen, J.L.M. (2015). CFD analysis of forced convective heat transfer coefficients at windward building facades: influence of building geometry, *J. Wind Eng. Ind. Aerodyn.* 146:102-116.

Moonen, P., Defraeye, T., Dorer, V., Blocken, B., Carmeliet, J. (2012). Urban physics: effect of the microclimate on comfort, health and energy demand, *Frontiers of Architectural Research* 1:197-228.

Murakami, S. (1998) Current status and future trends in computational wind engineering *Eng. Ind. Aerodyn.* 74e76 (1998) 1-24.

Murthy, B.N., Joshi, J.B. (2008). Assessment of standard k– ϵ , RSM and LES turbulence models in a baffled stirred vessel agitated by various impeller designs, *Chem Eng Sci.* 63: 5468 – 5495

Nakamura, H., Igarashi, T., Tsutsui, T. (2001). Local heat transfer around a wall mounted cube in the turbulent boundary layer, *Int. J. Heat. Mass Transf.* 44:3385-3395.

Natarajan, V., Chyu, M.K. (1994). Effect of flow angle-of-attack on the local heat/mass transfer from a wall-mounted cube, *Trans. ASME J. Heat. Transf.* 116:552-560.

Oke, T.R. (1988). Street design and urban canopy layer climate. *Energ Build* 11(1-3)103-

- Palyvos, J.A. (2008). A survey of wind convection coefficient correlations for building envelope energy systems' modeling, *Appl. Therm. Eng.* 28:801-808.
- Piringer, M., and Coauthors, (2002). Investigating the surface energy balance in urban areas - recent advances and future needs. *Water Air Soil Pollut. Focus*, 2:1–16.
- Raupach MR, Finnigan JJ, Brunei Y (1996) Coherent eddies and turbulence in vegetation canopies: the mixing-layer analogy. *Boundary-Layer Meteorol* 78(3):351–382
- Sharples, S. (1984). Full-scale measurements of convective energy losses from exterior building surfaces, *Build. Environ.* 19:31-39.
- Sparrow, E.M., Ramsey, J.W., Mass, E.A. (1979). Effect of finite width on heat transfer and fluid flow about an inclined rectangular plate, *J. Heat. Transf.* 101:199-204.
- Stathopoulos, T., Wu, H. (1995). Generic models for pedestrian-level winds in built-up regions, *J. Wind Eng. Ind. Aerodyn.* 54-55:515-525.
- Speziale, C.G. (1991). Analytical Methods for the Development of Reynolds-Stress Closures in Turbulence, *Annu Rev Fluid Mech.*, 23:107-157
- Speziale, C.G. (1995). A review of Reynolds stress models for turbulent shear flows, NASA Langley Research Center, NASA Contractor Report 195054, ICASE Report No. 95-15
- N. S. Sturrock (1971) Localized boundary layer heat transfer from external building surfaces. PhD Thesis, University of Liverpool
- UN-Habitat, *Cities and Climate Change: Global Report on Human Settlements 2011*(Earthscan: London and Washington, D.C., 2011), 92

UN Department of Economic and Social Affairs (UN - DESA): World urbanization prospectus: The 2018 revision, May 2018 New York.

Wang W (2012) An analytical model for mean wind profiles in sparse canopies. *Boundary-Layer Meteorol* 142(3):383–399.

Wang W. (2014). Analytically modelling mean wind and stress profiles in canopies. *Boundary-Layer Meteorol* 151(2)239–256

Yang, X.I.A., Sadique, J., Mittal, R., Meneveau, C. (2016). Exponential roughness layer and analytical model for turbulent boundary layer flow over rectangular-prism roughness elements. *J Fluid Mech* 789:127–165

Yazdanian, M., Klems, J.H. (1994) Measurement of the exterior convective film coefficient for windows in low-rise buildings, ASHRAE winter meeting, United States: N. p., 1993. Web.

Zhang, H., Huizenga, C., Arens, E., Wang, D. 2004. Thermal sensation and comfort in transient non-uniform thermal environments, *European Journal of Applied Physiology*, 92:728–733

Chapter 2

2 A new analytical model for wind flow in sparse canopies

2.1 Introduction

An approach to defining urban or plant morphology is in terms of the nature of packing of the obstacles. Oke (1988) identified three regimes that corresponded to different levels of obstacle packing densities. The sparsest arrangement corresponds to *isolated flow*, in which the aerodynamics of one obstacle is not influenced by the presence of another obstacle. The intermediate packing case is known as *interference flow*, for which the wake of an upstream obstacle interferes with the aerodynamics of a downstream obstacle. In the denser packing arrangement, a counter-flow vortex is trapped in between obstacles and a *skimming flow* passes over the obstacle surfaces.

In general, for canopies, the frontal density ($\lambda_f = A_f/A_d$), and/or planar density ($\lambda_p = A_p/A_d$) are used for describing the nature of packing of the obstacles. Where A_f is the frontal area, A_p is the planar area, and A_d is the unit underlying lot area on the ground surface (Figure 2.1).

There have been various analytical and numerical transport studies focused on either canopy-layer level applications (such as pedestrian level wind flow, convective heat exchange, and wind loading on components/parts of plants and built structures) or assessing the impact of plant or urban canopies on large scale atmospheric flow.

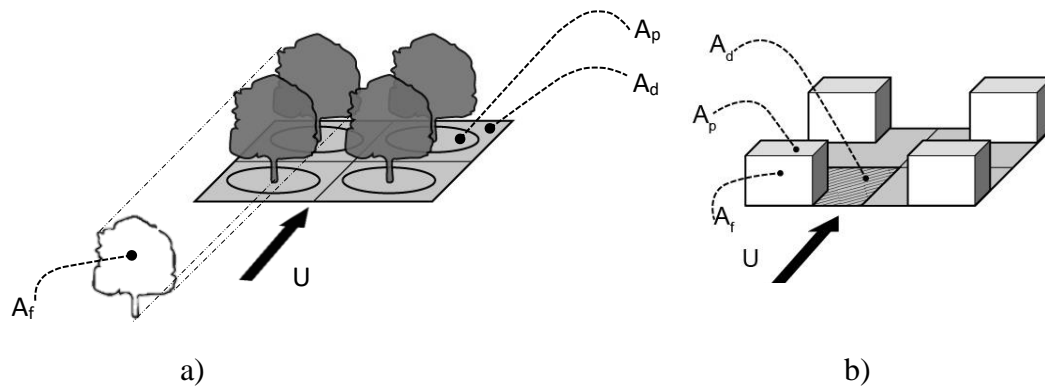


Figure 2.1 Packing density parametrization of idealized homogeneous canopy formed by a) plants b) buildings

Studies on the local roughness surface layer (RSL) flow involve the treatment of additional complexity due to roughness-induced inhomogeneous flow near the discrete obstacle surfaces (Inoue 1963, Cionco 1965, Cowan 1968, Landsberg et al. 1971, Macdonald 2000, Coceal et al. 2006, Yi 2008, Abdi and Bitsuamlak 2014, Yang and Meneveau 2016, and Castro et al. 2016). The prevailing intensified mixing and turbulence in the RSL prevent accurate measurements during experimentation (Raupach et al. 1996; Macdonald 2000). Simplified one-dimensional analytical models serve as a quick and easy alternative means of estimating flow parameters in the roughness sublayer (Inoue 1963, Cionco 1965, Wang 2012). In addition, arrays of cubes have been used in computational fluid dynamics (CFD) simulations to obtain various canopy flow parameters (Coceal et al. 2006, Brandford et al. 2011, Claus et al. 2012, Banerjee et al. 2013, Yang and Meneveau 2016, and Castro et al. 2016). These parameters provide important insight into the nature of flow in both the roughness layer and the overlying inertial layer. Canopy layer level applications have been reported in various areas such as pollution transport (Macdonald et al. 1998, Branford et al. 2011), wind loading assessment (Abdi and Bitsuamlak 2014, 2016), and heat/energy

transfer and heat island effects (Cowan 1968). The other focus of canopy studies is in assessing the impact of the roughness on the larger scale atmospheric flow (Thom 1971, Raupach and Thom 1981, Raupach et al. 1996, Brunet et al. 1994, Finnigan 2000, Cheng and Castro 2002, Cescatti and Marcolla 2004, Banerjee et al. 2013).

Earlier analytical canopy flow models have been developed for areas covered with plants (Inoue 1963, Cionco 1965, Cowan 1968, Yi 2008). These models were obtained from fundamental flow physics, and from field and laboratory observations. Later, the Cionco (1965) approach was adopted to obtain flow models for building canopies. The buildings were represented by arrays of cubes in wind-tunnel simulations (Macdonald 2000, Cheng and Castro 2002, Yang et al. 2016). However, most of these models are less reliable in sparse canopy arrangements (Wang 2012), as discussed below.

Inoue (1963) proposed the well-known exponential mean velocity profile in plant canopies. Cionco (1965), from the assumptions of constant mixing length on horizontally homogeneous and vertically-uniform plant canopies, presented the mean horizontal stream-wise wind speed, $u(z)$, at location z from the ground as given by Eq. 2.1.

$$u(z) = u_H \exp \left[\alpha_1 \left(\frac{z}{H} - 1 \right) \right] \quad \text{Eq. 2.1}$$

where H is the canopy top height above the ground, u_H is the horizontal wind velocity at the canopy top, i.e., $u(H)$, and α_1 is the *attenuation coefficient* introduced by Inoue (1963), the value of which increases with an increase in canopy density. This model, though widely used in the area of vegetation canopies and also adopted in building canopy studies, behaves unrealistically in three respects: (i) either the no-slip or the near-wall conditions (per ABL considerations) are not met if the attenuation coefficient or canopy density goes to lower values, (ii) the model does not fall to the logarithmic wind profile under a zero-

density ($\alpha_l = 0$) situation, (iii) in sparser densities the model is closer to linear than logarithmic shape. For instance, at large densities, the longitudinal momentum is expected to be the highest in the overlying layer.

Wang (2012), Ross (2008), and Yi (2008) have argued that unlike in dense canopies where the near-ground velocity is close to zero, the relatively higher near-ground velocity in sparse canopies gives rise to a non-negligible ground drag. The presence of this non-negligible drag, in turn, affects the mixing behavior in the canopies. Thus, the assumption that the turbulent mixing length is constant may be a valid case only under an ideal set of conditions. Recently, Castro (2017) questioned the validity of the exponential mean velocity profile in canopies, using data generated from various CFD simulations.

Macdonald (2000) and Coceal and Belcher (2004) have both applied the exponential velocity profile to building canopy studies. Both modified the original model, derived for vegetative canopies, to be applicable for cubic obstacle arrays; in an effort to represent the urban surface. Macdonald (2000) asserted that if the cubes were not too densely packed, the exponential velocity profile fits very well with the measured spatially-averaged mean wind profile. Moreover, the turbulence length scale was shown to decrease with an increase in the packing density. However, Raupach et al. (1991) found that RSL is a region of higher diffusivity compared to the log-layer region above it, the opposite of the finding by Macdonald (2000). The main limitation of Macdonald's work was in the case of higher packing densities. For cubical packing densities beyond the onset of skimming flow, the model (the exponential profile) was unable to capture the physical situation. For cubical arrays, the onset of a skimming flow occurs at about $\lambda_f = 16\%$ ($= \lambda_p$), which is associated with a counter-flow mean vortex structure in the lower part of street canyons. Coceal et al.

(2004) introduced a length scale relation determined from contributions of the length scales of the canopy drag and the ground drag. Pardyjak et al. (2008) further simplified Macdonald's (2000) model by forcing the velocities and slopes of the velocity profiles to be matched at the canopy height. Since Macdonald (2000), Coceal and Belcher (2004) and Pardyjack et al. (2008) employed the same exponential velocity model developed by Cionco (1965), many of the issues raised above against the exponential model at low densities are still unresolved.

For a horizontally homogeneous and vertically-uniform plant canopy, Cowan (1968) proposed a new model based on the proposition that the mean velocity profile is proportionally related to that of the eddy diffusivity profile. Even though the new model resolved the requirement of no-slip behavior near the ground, it did not fix the other two problems that were raised regarding Cionco (1965)'s model above. Cowan (1968)'s model resulted in;

$$u(z) = u_H \left[\frac{\sinh(\alpha_2 z/H)}{\sinh(\alpha_2)} \right]^{1/2} \quad \text{Eq.2.2}$$

where α_2 is the *attenuation coefficient*, a parameter related to canopy density. Even though Cowan's model (Eq.2.2) conforms to the no-slip condition, the model still approaches a linear curve as $\alpha_2 = 0$ (and not logarithmic), leading to errors in the prediction of drag for sparse canopies. Figure 2.2 shows the mean velocity profiles (according to Inoue 1965 and Cowan 1968).

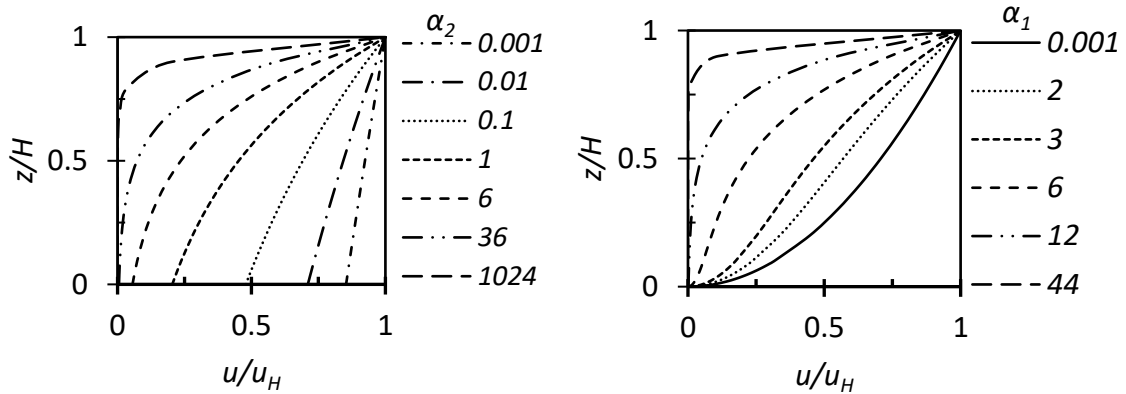


Figure 2.2 Normalized canopy mean velocity profile generated by using a) Inoue's model (Eq.1.2)
b) Cowan's model (Eq.1.3)

Albini (1981) and Landsberg and James (1971) found other forms of the mean velocity profile from assumptions with less rigor in physics. Albini (1981) assumed a non-zero velocity at the ground, in addition to a phenomenological assignment for the vertical pressure gradient dp/dz , which is that dp/dz is proportional to udu/dz . Landsberg and James (1971) presumed the velocity to be inversely proportional to the square of the vertical distance, based on observations from experimental data. Landsberg and James (1971) and Thom (1971) used a constant turbulent diffusivity assumption. The results of Albini (1981), Landsberg and James (1971) and Yi (2008) are prone to arguments raised against the exponential profile discussed above.

Wang (2012, 2014) used a first-order turbulence closure scheme and parametrized the mixing length using length scale contributions from the ground and the canopies themselves. In addition, the drag term was linearized by the velocities at a reference height (Wang 2012) or by the friction velocity (Wang 2014). The solutions presented in terms of Bessel functions have better mean velocity prediction capabilities for sparse canopy cases compared to earlier analytical solutions.

It can be deduced that many existing one-dimensional analytical models with various first-order turbulence closure schemes can be improved to fulfill one or more conditions in terms of boundary-layer physics in sparse densities. The present work develops a new one-dimensional analytical model for wind flow in low-density canopies. The new model can be used to obtain the mean wind velocity profile and drag and turbulent shear parameters. The current study retains the horizontally homogeneous and vertically-uniform canopy assumption of previous researchers but proposes a new drag parametrization approach to arrive at a consistent analytical mean wind velocity profile for a range of sparse canopies. The results from the new model are validated in comparison with experimental work from the literature. The resulting turbulence and drag parameters are further discussed.

2.2 Model Derivation

The time-averaged Navier-Stokes equation can be simplified with suitable assumptions to obtain a simplified mathematical model for flow in canopies of plants or building obstacles. In a steady and fully-developed flow past rigid horizontally homogeneous obstacles, the longitudinal momentum equation reduces to a balance of drag, and turbulent flux terms, as shown in Eq.2.3.

$$0 = -\frac{\partial(\overline{u'w'})}{\partial z} + f_D \quad \text{Eq.2.3}$$

where u' , w' are turbulent fluctuation velocities in the streamwise and vertical directions (z), and f_D is the total sectional drag force per unit mass. Parametrizations of the terms in Eq.2.3 are discussed next.

2.2.1 Turbulent shear parameterization

The first term on the right-hand side of Eq.2.3, that represents the turbulent/Reynolds shear stress, can be represented based on first-order turbulence closure scheme (Garratt 1994).

Based on the eddy viscosity model, the turbulent shear then becomes like Eq.2.4.

$$\frac{\partial}{\partial z}(\overline{u'w'}) \approx \frac{\partial}{\partial z} \left(K \frac{\partial u}{\partial z} \right) \quad \text{Eq.2.4}$$

and the eddy diffusivity, K , is represented by the mixing length theory, as shown in Eq.2.5.

$$K = l_m u_m, \quad u_m = l_m \left| \frac{\partial u}{\partial z} \right|, \quad \text{and} \quad l_m = kzS \quad \text{Eq.2.5}$$

where l_m is mixing length, u_m is dynamical velocity (the velocity scale corresponding to the eddy-viscosity), S is a factor related to the length scale alteration due to the presence of the canopy, and k is the von Karman constant.

Therefore, the turbulent shear force is approximated as in Eq.2.6.

$$\frac{\partial}{\partial z}(\overline{u'w'}) \approx \frac{\partial}{\partial z} \left[\left(kzS \frac{\partial u}{\partial z} \right)^2 \right] \quad \text{Eq.2.6}$$

2.2.2 Drag Parametrization

The total sectional drag force per unit mass (second term on the right-hand side of Eq.2.3), when expressed in terms of sectional drag coefficient (C_d), a density parameter (a) and a local mean velocity (u), is as shown in Eq.2.7.

$$f_D = \frac{1}{2} C_d(z) a(z) (u(z))^2 \quad \text{Eq.2.7}$$

The sectional density parameter is defined using the sectional frontal area (of each obstruction), dA_f between the levels z and $z + dz$, and the unit underlying lot area on the ground surface, A_d (as given in Eq.2.8).

$$a = \frac{1}{A_d} \frac{dA_f}{dz} \quad \text{Eq.2.8}$$

For uniform obstacle cross-sections, dA_f/dz becomes A_f/H , where the frontal area, A_f , represents the area of obstruction exhibited by the flow due to obstructing elements (plant or building – see Figure 2.1). Other packing density considerations may employ the planar area density, A_p , representing the average area of horizontal planar projection cast by the obstacles. In most urban canopy flow simulations, buildings are represented by arrays of cubes, implying equal frontal and planar area indices ($A_f = A_p$).

In sparse canopy scenarios, we assume the local values of the Reynolds stress per local mean velocity $(kzS(\partial u/\partial z)/(Hu))^2$, under the canopy, does not deviate much from the $(u_*/u_H)^2$ value at the top of the canopy boundary. ($\phi = u_*/u_H$, a measure of the canopy drag is known as the canopy flux parameter). Thus, we consider the mean velocity to scale with $(kzS(\partial u/\partial z)/(Hu_*/u_H))$. Hence,

$$\frac{u^2}{u_H^2} \approx k^2 z^2 S^2 \left(\frac{\partial u}{\partial z} \right) \left(\frac{\partial u}{\partial z} \right) / u_*^2 \quad \text{Eq.2.9}$$

This assumption is not very different from Wang (2014)'s partial use of $u = u_*$ in the drag parametrization. Thus, the following approximation of u^2 can be used in the drag parametrization:

$$u^2 \approx \frac{k^2}{\phi^2} z^2 S^2 \left(\frac{\partial u}{\partial z} \right) \left(\frac{\partial u}{\partial z} \right) \quad \text{Eq.2.10}$$

From Eq.2.7 and Eq.2.10, the sectional drag force is obtained, as shown in Eq.2.11.

$$f_D = \frac{1}{2} C_d(z) a(z) \frac{k^2}{\phi^2} z^2 S^2 \left(\frac{\partial u}{\partial z} \right) \left(\frac{\partial u}{\partial z} \right) \quad \text{Eq.2.11}$$

2.2.3 Governing flow model and solution

The simplified governing flow model for the turbulent-shear-driven roughness-layer flow in plant/urban canopies, based on Eq.2.5 and Eq.2.11, can be given, as shown in Eq.2.12.

$$\frac{\partial}{\partial z} \left[\left(kzS \frac{\partial u}{\partial z} \right)^2 \right] = \frac{1}{2} C_d(z) a(z) \frac{k^2}{\phi^2} z^2 S^2 \left(\frac{\partial u}{\partial z} \right) \left(\frac{\partial u}{\partial z} \right) \quad \text{Eq.2.12}$$

Equation 2.12 is not tractable into a closed-form analytical solution. Linearization of some of the parameters in this equation yields a form that can be easily integrated. To this end, we undertake linearization of the variables given in Eq.2.13.

$$C_d(z) \sim C_{do}; \quad a(z) \sim a_o = \frac{\lambda_f}{H}; \quad S(z) \sim S_H \quad \text{Eq.2.13}$$

This implies a vertically-uniform sectional drag, C_{do} , and a frontal density parameter corresponding to vertically-uniform section, a_o . In addition, the canopy length scale contribution factor, $S(z)$, will be replaced by its corresponding value at the top of the canopy, S_H .

The differential equation representing the desired canopy layer flow model is shown in Eq.2.14.

$$\frac{\partial}{\partial z} \left[\left(z \frac{\partial u}{\partial z} \right)^2 \right] = \frac{1}{2} C_{do} \lambda_f \frac{1}{\phi^2} z^2 \left(\frac{\partial u}{\partial z} \right) \left(\frac{\partial u}{\partial z} \right). \quad \text{Eq.2.14}$$

In anticipation of a simple tractable solution, the above equation (Eq.2.14) is further simplified by the assumption that the local gradient ($\partial u/\partial z$) can be replaced by its equivalent at the top of the canopy (i.e., $u_*/(kS_H H)$). In Sect. 5, the effect of this approximation will be shown to be negligible by a validation process.

Non-dimensionalizing the resulting form with $\left(\zeta = \frac{z}{H}\right)$, and $(U = u/u_H)$, Eq.2.15 is obtained.

$$\frac{\partial}{\partial \zeta} \left[\left(\zeta \frac{\partial U}{\partial \zeta} \right)^2 \right] = \alpha \zeta^2 \frac{\partial U}{\partial \zeta} \quad \text{Eq.2.15}$$

where
$$\alpha = \frac{1}{2} C_{d0} \lambda_f \frac{1}{k S_H \phi} \quad \text{Eq.2.16}$$

By considering the boundary conditions (at $\zeta = \zeta_0 = z_0/H, U = 0$; and at $\zeta = 1, U = 1$), the solution of the differential equation (Eq.2.15) is given in Eq.2.17.

$$U = (\alpha/8)\zeta^2 + (1 - \alpha/8) \frac{\ln(\zeta/\zeta_0)}{\ln(1/\zeta_0)} + \zeta_0^2 (\alpha/8) \left(\frac{\ln(\zeta/\zeta_0)}{\ln(1/\zeta_0)} - 1 \right) \quad \text{Eq.2.17}$$

z_0 is the aerodynamic roughness scale associated with the approaching wind/background flow, and the ratio H/z_0 is known as the Jensen Number. The third term on the right side of Eq.2.17 is very small, compared to the other two, due to ζ_0^2 . Thus, the mean stream-wise velocity in the canopy flow can be approximated by Eq.2.18.

$$U = (\alpha/8)\zeta^2 + (1 - \alpha/8) \frac{\ln(\zeta/\zeta_0)}{\ln(1/\zeta_0)} \quad \text{Eq.2.18}$$

This final solution form has satisfied the main drawbacks observed in conventional roughness-layer models in the sparse density range (see Figure 2.3). The current analytical model fulfills the near ground velocity condition, to the accuracy of the canonical ABL

(atmospheric boundary layer) flow model. More importantly, the velocity profile approaches the logarithmic law in sparse canopy scenarios. The profile replicates the ABL logarithmic condition in ‘no canopy’ situations. Figure 2.3d shows all models for selected common values of the shear length scale, $L_s/H = 1/(\partial U/\partial \zeta|_{\zeta=1})$.

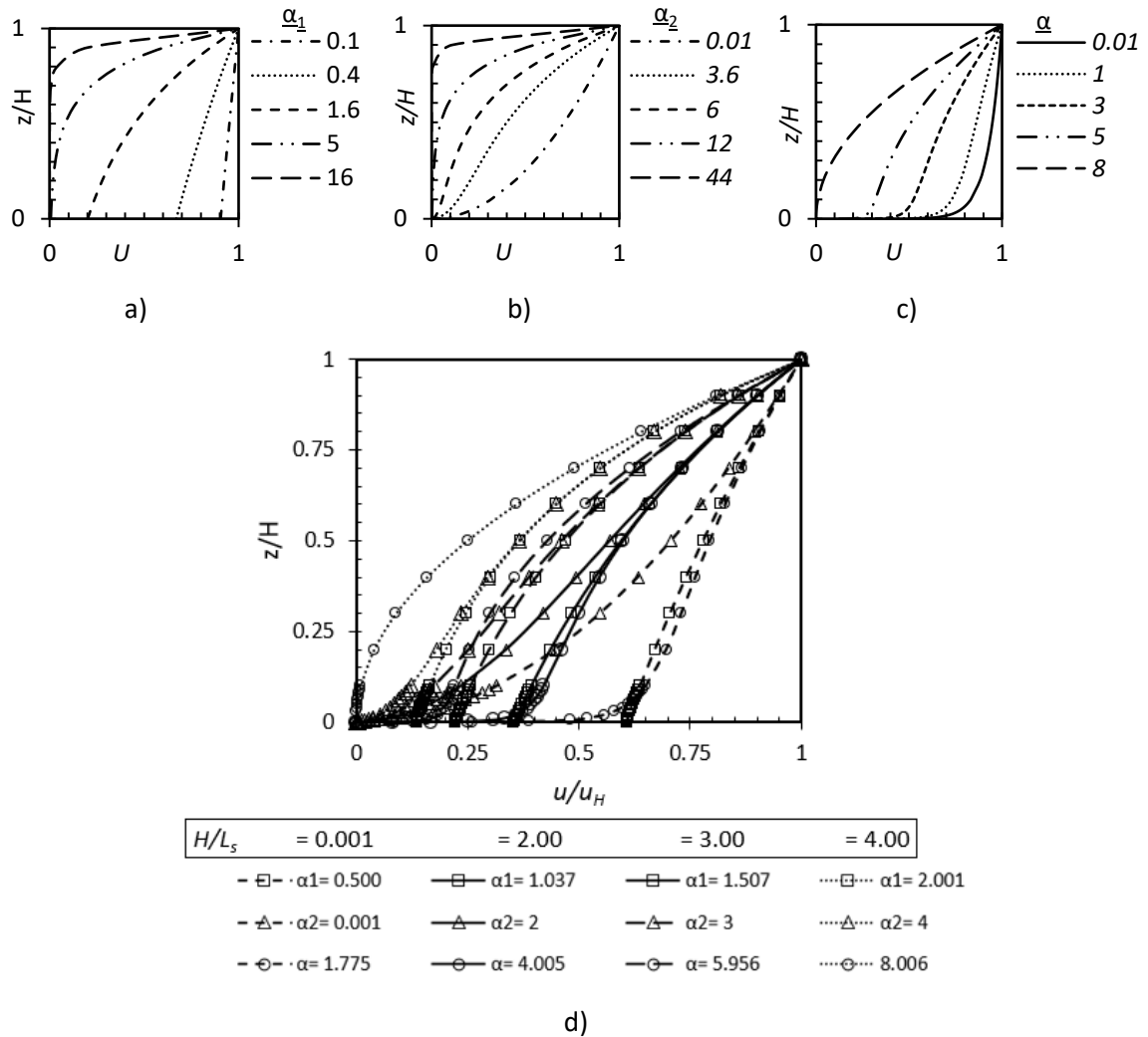


Figure 2.3 Normalized canopy mean velocity profile a) Inoue’s model (Eq. 2.1) b) Cowan’s model (Eq.2.7) c) present model (Eq.2.18) d) all models at selected values of the shear length scale

2.2.4 Relationship between the ‘attenuation coefficient’ and canopy density

The relationship between the attenuation coefficient and the packing density can be obtained from experimental data. Here, we use data from Raupach et al. (1996), Novak et al. (2000), and Pietri et al. (2009), where the shear length scale, L_s , at different packing densities, λ_f , are provided. The shear length scale is a measure of the location of the inflection point at which instabilities in the mixing layer exhibit proportionality to the magnitude of shear (Raupach et al. 1996). The normalized form of shear length scale, L_s/H , is defined as shown in Eq.2.19.

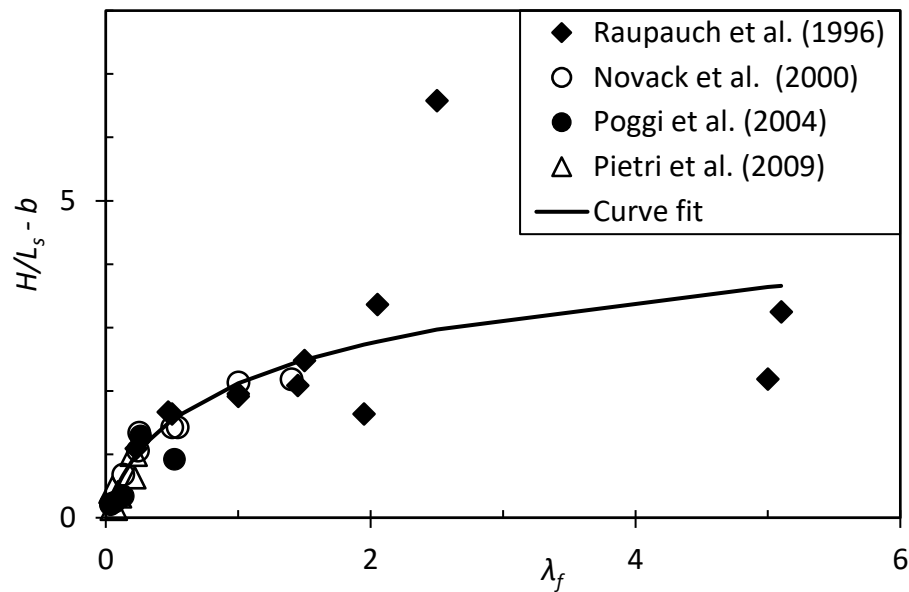


Figure 2.4 Plot of H/L_s from experimental data against frontal area density (data from Raupach et al. (1996), Novak et al. (2000), Poggi et al. (2004) and Pietri et al. (2009))

$$\frac{L_s}{H} = \frac{1}{\partial U / \partial \zeta |_{\zeta=1}}, \quad \text{Eq.2.19}$$

thus, using the current model, it can be given as shown in Eq.2.20.

$$\frac{H}{L_s} = \alpha/4 + (1 - \alpha/8)b \quad \text{Eq.2.20}$$

where

$$b = 1/\ln(1/\zeta_0) \quad \text{Eq.2.21}$$

A best-fitting log curve is sought for the experimental data from the works of Raupach et al. (1996), Novak et al. (2000), and Pietri et al. (2009) for a plot of λ_f versus H/L_s (Figure 2.4). Recognizing b is the value of H/L_s at $\lambda_f = 0$ or $\alpha = 0$. The equation that fits this curve is given in Eq.2.22 (with $A_1 \approx 1$, $A_3 \approx 2$, and $A_2 = \exp((b - A_3)/A_1) \approx \exp(b - 2)$).

$$\frac{H}{L_s} - b = A_1 * \ln(\lambda_f + A_2) + A_3 \quad \text{Eq.2.22}$$

Equations 3.20 and 3.22 can be combined to obtain the relationship between the frontal area density, λ_f , and the attenuation coefficient, α , for the current model, as shown in Eq.2.23.

$$\alpha = \frac{8}{(2 - b)} [A_1 * \ln(\lambda_f + A_2) + A_3] \quad \text{Eq.2.23}$$

2.4.1 Prediction of drag parameters

The drag coefficient, C_{dH} , based on velocity at the mean roughness height H (i.e., u_H), can be estimated by Eq.2.24.

$$k^2 S_H^2 \left(\frac{\partial U}{\partial \zeta} \right)^2 \Big|_{\zeta=1} = \frac{1}{2} C_{dH} \lambda_f = \varphi^2 \quad \text{Eq.2.24}$$

φ can be determined using data provided in Raupach et al. (1996), Novak et al. (2000), and Pietri et al. (2009). Thus,

$$C_{dH} = 2\varphi^2/\lambda_f \quad \text{Eq.2.25}$$

φ as a function of density and it can be fit to an exponential function (Figure 2.5) of $\varphi = B_1 + (kb - B_1) * \text{Exp}(-B_2\lambda_f)$, by considering the maximum value of φ at higher λ_f values approaches a value (B_1) between 0.3 and 0.4 (Masmann 1997). It should also be noted that the value of φ at $\lambda_f = 0$ is kb . The constants of the equation become; $B_1 = 0.344$, and $B_2 = 3.49$.

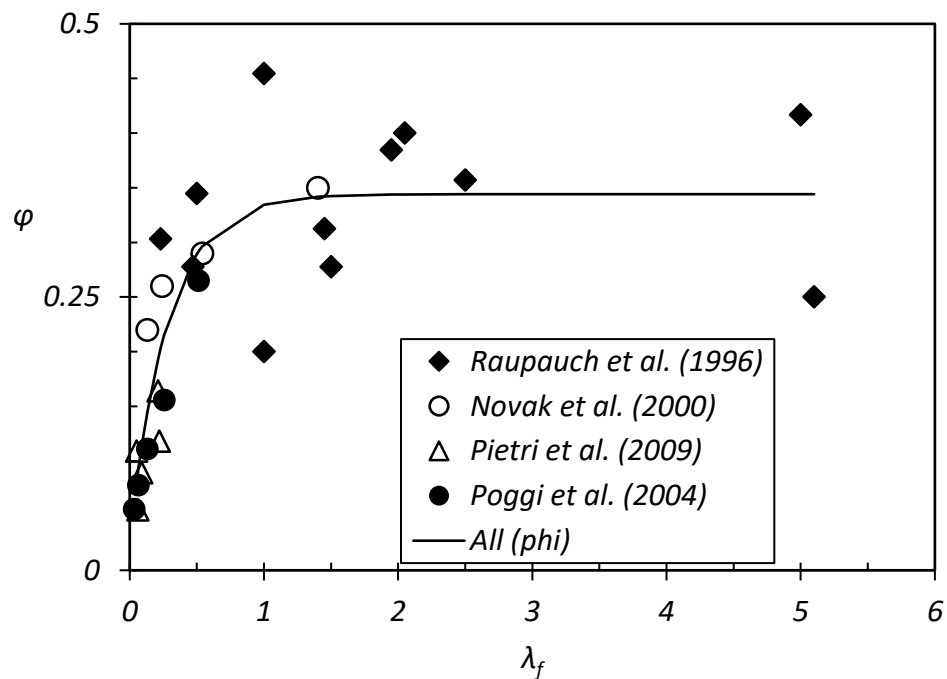


Figure 2.5 Plot of ϕ from experimental data against frontal area density (data from Raupach et al. (1996), Novak et al. (2000), Poggi et al. (2004) and Pietri et al. (2009))

Determination of the height averaged mean drag coefficient, $\overline{C_d}$, is showed by using the fact that the wall drag under the canopy is balanced by the turbulent shear at the canopy top. This is shown in Eq.2.26 and Eq.2.27.

$$k^2 S_H^2 \left(\frac{\partial U}{\partial \zeta} \right)^2 \Big|_{\zeta=1} = \frac{1}{2} \bar{C}_d \lambda_f (\bar{U})^2 = \frac{1}{2} \bar{C}_d \lambda_f \int_{\zeta_0}^1 U^2 d\zeta \quad \text{Eq.2.26}$$

and

$$\bar{C}_d = C_{dH} / (\bar{U})^2 \quad \text{Eq.2.27}$$

where

$$(\bar{U})^2 = (1/5)(\alpha/8)^2 + (2/9)(\alpha/8)(1 - \alpha/8)(3 - b) + (1 - \alpha/8)^2(1 - 2b + 2b^2).$$

Now, using Eq.2.16, and Eq.2.26; the sectional drag coefficient, C_{d0} , Eq.2.28 is obtained. i.e.,

$$C_{d0} = \bar{C}_d \alpha \left(\frac{(\bar{U})^2}{(\alpha/4) + (1 - \alpha/8)b} \right) \quad \text{Eq.2.28}$$

A plot of the three drag coefficients along with \bar{U}^2 and φ against λ_f (log scale) is shown in Figure 2.6. The mean drag coefficient is further discussed in Sec. 3.

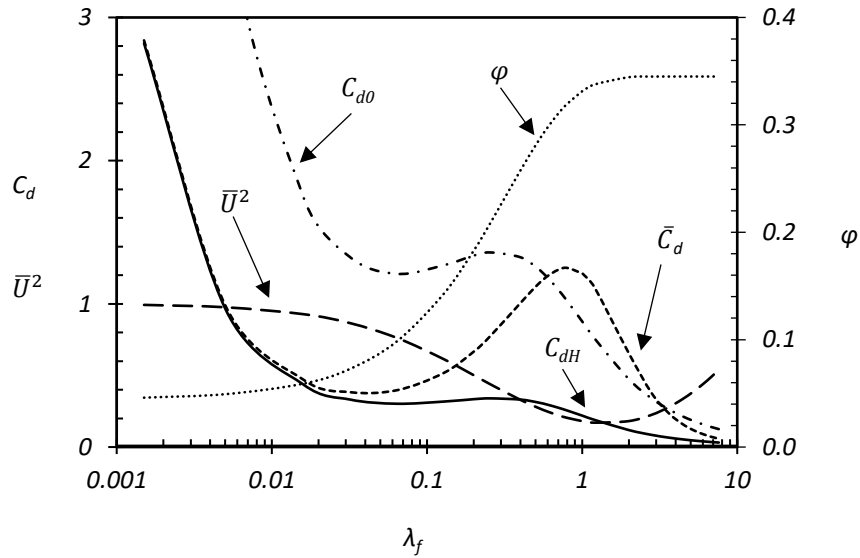
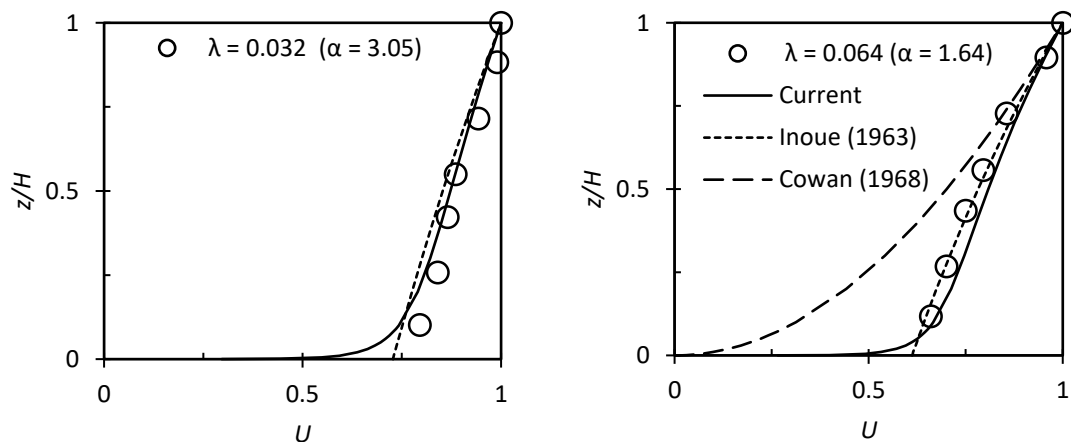


Figure 2.6 Plot of drag coefficients, height averaged mean velocity from the current model and the exponentially fitted canopy flux parameter

2.3 Validation of the model

The mean velocity profile from the present model is compared against experimental measurements by Poggi et al. (2004), Bohm et al. (2013) and Brunet et al. (1994). Measurements for five packing densities (from Poggi et al. (2004)) were used to test the predictability of the mean velocity in the canopy layer (Figure 2.7). Mean velocity profiles from Inoue (1963) and Cowan (1968) are included in the plots. Figure 2.7 indicates that the present velocity profile matches the experimental measurements very well in most of the cases. However, as shown in Figure 2.4 and Figure 2.5, measurements at higher packing densities are known to exhibit very high scatter (Raupach et al. 1996, Massman 1997, Macdonald 2000). Further assessment using measurements by Bohm et al. (2013) and Brunet et al. (1994) indicated a good match with model predictions at other densities (Figure 2.8). Though negligible, differences at very low densities may be attributed to the arbitrary value used for z_0/H (i.e., 10^{-6}). Cowan (1968) model does not produce results at very sparse densities and underestimates the mean velocity at sparse and intermediate densities. The prediction by the present model is found to be better than Inoue (1963) model for low density canopies in general.



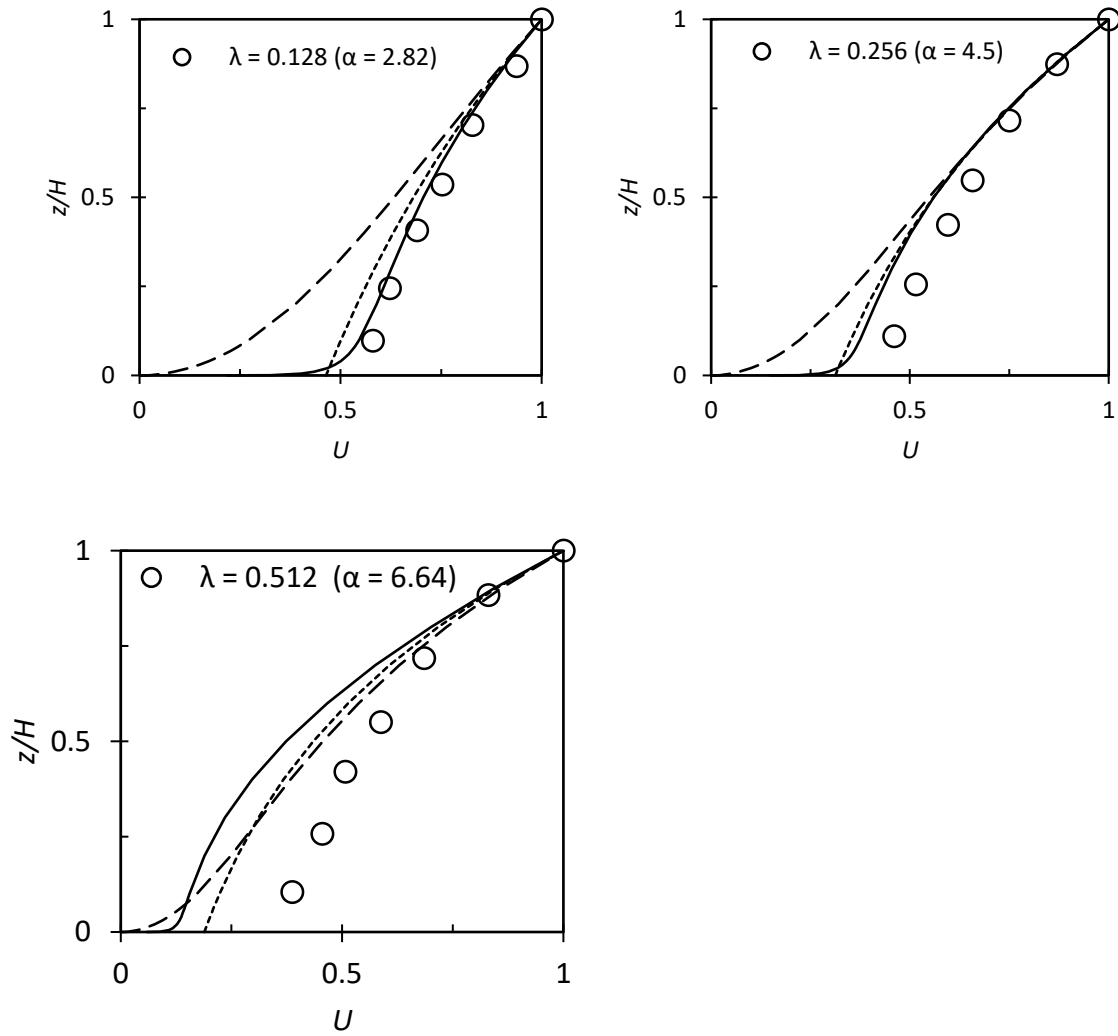


Figure 2.7 Plot of normalized canopy mean velocity profile from experimental data (Poggi et al.

2004) against that of the present model, and sensitivity to $\pm 33\%$ of the λ_f

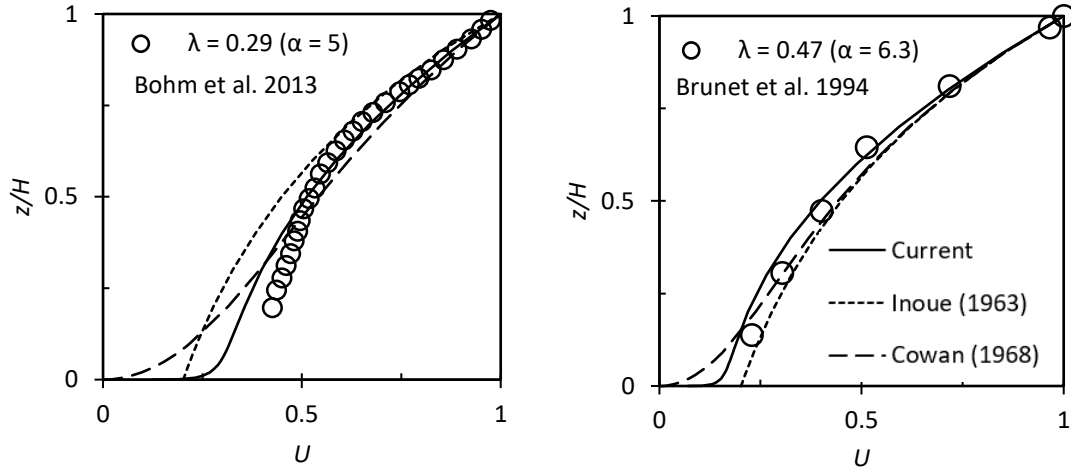


Figure 2.8 Comparison of normalized canopy mean velocity profile from the present analytical model with experimental data: a) Bohm et al. (2013), b) Brunet et al. (1994).

Figure 2.9 shows the sensitivity of the mean velocity for three different densities with a $\pm 10\%$ variation in shear length scale, L_s/H . L_s/H value has very large scatter, as shown in Figure 2.4 and Figure 2.5 at larger densities. In view of the magnitude of scatter observed in measured L_s/H values, the 10% deviation is considered as a small band. As shown in the sensitivity plots (Figure 2.9), the variations in the mean velocity at low and intermediate densities are attenuated. It is to be noted that, due to the primary assumption made in this paper, the validity of the present model is expected to be sounder in lower densities.

The sensitivity of the mean velocity for three different densities at three z_0/H values, namely 10^{-4} , 10^{-5} , 10^{-7} , are shown in Figure 2.10. Figure 2.10 indicates larger absolute changes in the mean velocity at lower densities. However, the higher percentage changes are found at higher densities, due to the very low values of mean velocity in these situations. Nonetheless, for an order of magnitude change in z_0/H (particularly large perturbation), the maximum change in the value of U/U_H is less than 10% at $z/H = 0.15$ ($\lambda = 0.55$).

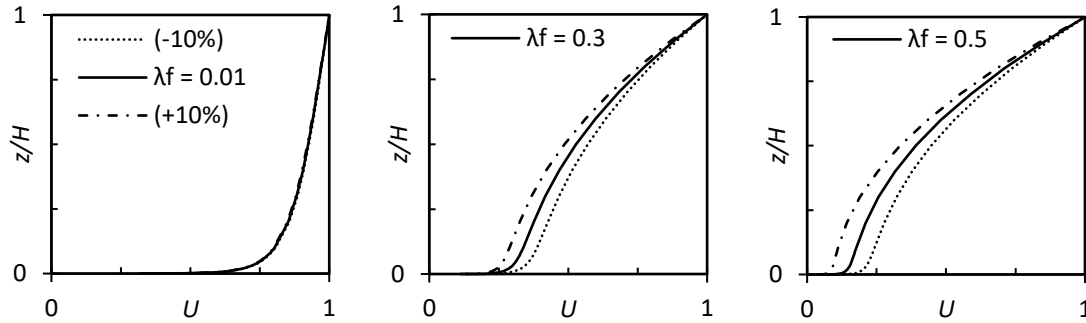


Figure 2.9 Sensitivity of the normalized mean velocity for three different densities with +/-10% variation in shear length scale, L_s/H .

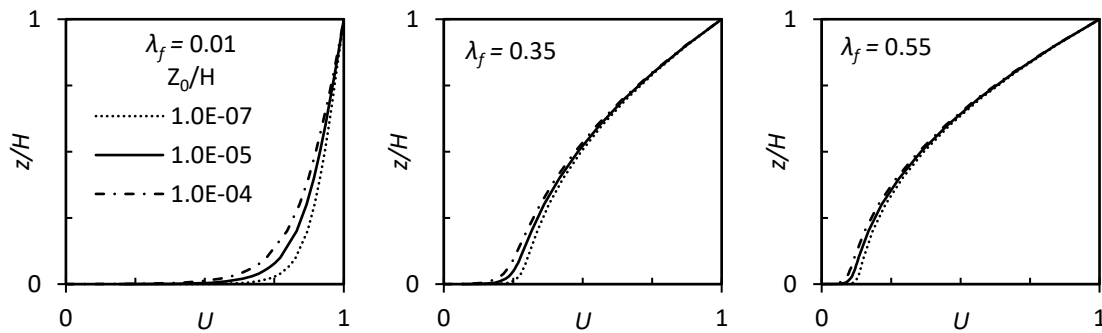


Figure 2.10 Sensitivity of the normalized mean velocity for three different densities at three z_o/H values (short and long dash: $z_o/H = 10^{-4}$, solid: $z_o/H = 10^{-5}$, dash: $z_o/H = 10^{-7}$)

2.4 Discussion

As described in Sect. 2.6, the model performed well through validation against experimental measurements of earlier studies. Considering the uncertainties of the model mentioned and the implication of the assumptions made, some features of the model are further discussed in this section.

Firstly, the trend and sensitivity of the mean drag coefficient for different values of z_o/H is conducted and plotted in Figure 2.11. The model curve matched the trend of the mean drag coefficient values obtained by Poggi et al. (2004) in the range λ_f between 0.03 and 0.7

(marked II in Figure 2.11). Despite the large scatter in Novak et al. (2004) data for the mean drag coefficient, the model is also able to predict the trend and location of inflection on the curve near $\lambda_f = 0.7$. The test indicates for changes as large as an order of magnitude in z_o/H the mean drag coefficient varies only by 6, 12, 14% at densities (λ_f) of 0.5, 0.1 and 0.01 respectively. The sensitivity of \bar{C}_d is the highest at lower densities than higher ones. This is expected because, at very low densities, the scales of canopy roughness and the background aerodynamic roughness become comparable. The Engineering Standard Data Unit (ESDU) puts the highest value of the height-averaged drag coefficient, \bar{C}_d , at about 2.8 (ESDU 1980), which is also a case projected by the current model for very sparse canopies (region I in Figure 2.11). \bar{C}_d starts to reduce indefinitely above $\lambda_f = 0.7$ (region III in the Figure 2.11).

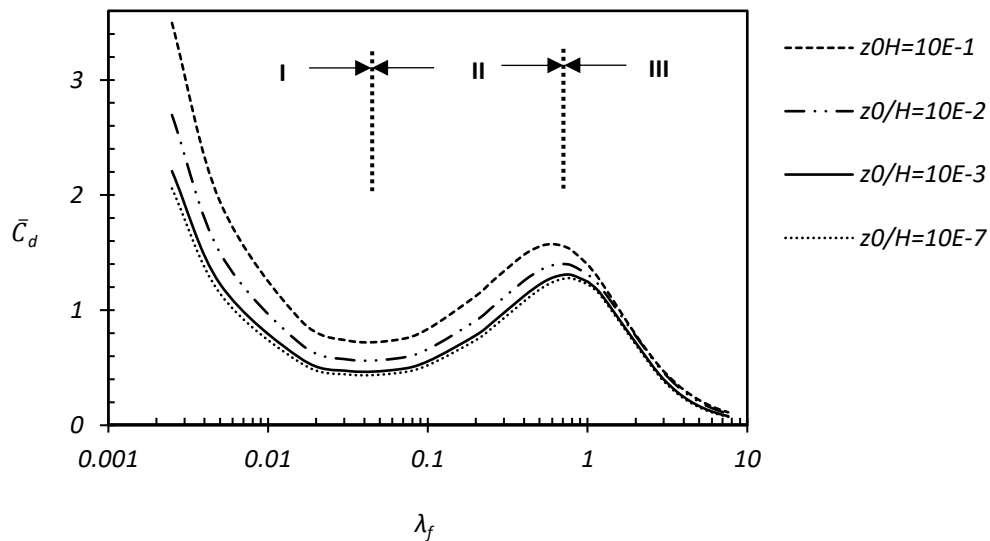


Figure 2.11 Sensitivity of the mean drag coefficient for different values of z_o/H .

The two inflection points, and hence the two transitions appear to loosely conform to the changes in flow regimes from isolated to wake interference and from wake interference to skimming flow. Thus, the mean drag may have a decreasing or increasing trend based on

the flow regime considered. This explains the differences in conclusion by Poggi et al. (2004) and Novak et al. (2000).

Secondly, Eq.2.18 appears to suggest that there is some physical relevance to $\alpha = 8$ ($\lambda_f \approx 0.7$). In Figure 2.3, $\alpha = 8$ corresponds to the second term in Eq.2.18 becoming zero, and initiation of flow reversal near the ground surface. However, in general, a near zero uniform mean velocity is expected at very high densities (and not flow reversal). Thus, $\alpha = 8$ may be taken as the point at which the current model breaks down. The parameter α can also be written as $\alpha = 8 \left(\frac{H}{L_s} - b \right) / (2 - b)$. This indicates the limiting value of H/L_s is also 2 or ($L_s/H = 0.5$).

2.5 Conclusion

A new analytical model for airflow in the canopy layer for sparse densities has been developed from first principles with few key assumptions. The one-dimensional model is obtained from the assumption of steady state, homogeneous turbulence in the roughness sublayer flow and considers sparse canopies. More importantly, it is considered that the local Reynolds stress by the square of local space-averaged mean velocity does not vary much from the corresponding value at the top of the canopy. The resulting model respects the near ground velocity predictions as per ABL considerations; and approaches the apparent log-law atmospheric boundary-layer profile at very low packing densities. These physical realities have not been demonstrated by previously developed analytical models.

The current analytical model is validated through comparison with experimental data obtained from the literature, and the sensitivity of the mean velocity profile is

investigated against changes in the shear length scale (L_s/H), and the aerodynamic roughness length scale (z_o/H). Both of these processes demonstrated the present model gives acceptable results.

These findings affect the evaluation of transport parameters in areas like convective heat transfer, mass and pollutant dispersion in vegetative and urban canopies, and other urban wind flow topics (comfort, energy, and wind-driven rain).

This new analytical model can be further investigated within topics that include the determination of displaced log-law parameters, improvement in the boundary-layer profile through better turbulent mixing-length scale representation, roughness or canopy density transitions, applications in convective heat transport, the effect of planar density (when it is not the same as frontal density) in canopy transport, etc.

References

- Abdi, D, Bitsuamlak, GT (2014) Numerical evaluation of the effect of multiple roughness changes. *Wind and Structures* 19(6): 585-601.
- Abdi, D, Bitsuamlak, GT (2016) Wind flow simulations in idealized and real built environments with models of various level of complexity. *Wind & Structures* 22 (4): 503-524.
- Albini FA (1981) A phenomenological model for wind speed and shear stress profiles in vegetation cover layers. *J Appl Meteorol* 20(11):1325–1335

- Banerjee, T, Katul, G, Fontan, S, Poggi, D, Kumar, M (2013) Mean flow near edges and within cavities situated inside dense canopies. *Boundary-layer meteorol* 149(1):19-41.
- Böhm, M, Finnigan, JJ, Raupach, MR, Hughes, D (2013) Turbulence structure within and above a canopy of bluff elements. *Boundary-Layer Meteorol* 146(3): 393-419.
- Branford S, Coceal O, Thomas TG, Belcher SE (2011) Dispersion of a point-source release of a passive scalar through an urban-like array for different wind directions. *Boundary-Layer Meteorol* 139:367–394
- Brunet Y, Finnigan JJ, Raupach M (1994) A wind tunnel study of air flow in waving wheat: single point velocity statistics. *Boundary-Layer Meteorol* 70:95–132
- Castro IP, Xie ZT, Fuka V, Robins AG, Carpentieri M, Hayden P, Hertwig D, Coceal O (2016) Measurements and computations of flow in an urban street system. *Boundary-Layer Meteorol* 162:207-230
- Castro IP (2017) Are urban-canopy velocity profiles exponential? *Boundary-Layer Meteorol* 164:337-351
- Cescatti A, Marcolla B (2004) Drag coefficient and turbulence intensity in conifer canopies. *Agric For Meteorol* 121(3– 4):197–206
- Cheng H, Castro IP (2002) Near-wall flow over urban-like roughness. *Boundary-Layer Meteorol* 104(2): 229–259
- Cionco RM (1965) Mathematical model for air flow in a vegetative canopy. *J Appl Meteorol* 4:517–522
- Cionco RM (1972) Intensity of turbulence within canopies with simple and complex roughness elements a mathematical. *Boundary-Layer Meteorol* 2:453-465

- Claus J, Coceal O, Thomas TG, Branford S, Belcher SE, Castro IP (2012) Wind direction effects on urban flows. *Boundary-Layer Meteorol* 142:265–287
- Coceal O, Belcher SE (2004) A canopy model of mean winds through urban areas. *Q J R Meteorol Soc* 130(599):1349–1372
- Coceal O, Thomas TG, Castro IP, Belcher SE (2006) Mean flow and turbulence statistics over groups of urban-like cubical obstacles. *Boundary-Layer Meteorol* 121:491–519
- Cowan IR (1968) Mass, heat and momentum exchange between stands of plants and their atmospheric environment. *Q J R Meteorol Soc* 94:523–544
- ESDU (1986), Mean Fluid Forces and Moments on Rectangular Prisms: Surface-Mounted Structures in Turbulent Shear Flow, Engineering Sciences Data Item Number 80003
- Finnigan J (2000) Turbulence in plant canopies. *Annu Rev Fluid Mech* 32(1):519–571. doi:10.1146/annurev.fluid.32.1.519
- Finnigan J, Belcher SE (2004) Flow over a hill covered with a plant canopy. *Q J R Meteorol Soc* 130(596):1–29
- Garratt JR (1994) The atmospheric boundary layer. Cambridge University Press, Cambridge, UK, 316 pp
- Hall, TC, Britter RE, Norford, LK (2012) Predicting velocities and turbulent momentum exchange in isolated street canyons *Atmos Environ* 59:75–85. doi:10.1016/j.atmosenv.2012.05.003
- Inoue E (1963) On the turbulent structure of air flow within crop canopies. *J Meteorol Soc Jpn* 41:317–326
- Landsberg JJ, James GB (1971) Wind profiles in plant canopies: studies on an analytical model. *J Appl Ecol* 8(3):729–741

- Macdonald, RW, Griffiths, RF, Hall, DJ (1998) A comparison of results from scaled field and wind tunnel modelling of dispersion in arrays of obstacles. *Atmos. Environ* 32(22):3845–3862
- Macdonald RW (2000) Modelling the mean velocity profile in the urban canopy layer. *Boundary-Layer Meteorol* 97(1):25–45
- Massman WJ (1997) An analytical one-dimensional model of momentum transfer by vegetation of arbitrary structure. *Boundary-Layer Meteorol* 83(3):407–421
- Millward-Hopkins JT, Tomlin AS, Ma L, Ingham D, Pourkashanian M (2011) Estimating aerodynamics parameters of urban-like surfaces with heterogeneous building heights. *Boundary-Layer Meteorol* 141:443–465
- Novak MD, Warland JS, Orchansky AL, Ketler R, Green S (2000) Wind tunnel and field measurements of turbulent flow in forests. Part I: Uniformly thinned stands. *Boundary-Layer Meteorol* 95(3):457–495
- Oke, TR (1988) Street design and urban canopy layer climate. *Energy and Buildings* 11(1-3):103-113
- Pardyjak ER, Speckart SO, Yin F, Veranth JM (2008) Near source deposition of vehicle generated fugitive dust on vegetation and buildings: model development and theory. *Atmos. Environ.*, 42:6442-6452
- Pietri L, Petroff A, Amielh M, Anselmet F (2009) Turbulence characteristics within sparse and dense canopies. *Environ Fluid Mech* 9(3):297–320
- Poggi D, Porporato A, Ridolfi L, Albertson JD, Katul GG (2004) The effect of vegetation density on canopy sub-layer turbulence. *Boundary-Layer Meteorol* 111(3):565–587

- Raupach, M, Thom AS (1981) Turbulence in and above plant canopies. *Annu Rev Fluid Mech* 13:97–129
- Raupach, MR, Antonia, RA, Rajagopalan, S (1991) Rough-Wall Turbulent Boundary Layers. *Appl. Mech. Rev.* 44: 1–25.
- Raupach MR (1994) Simplified expressions for vegetation roughness length and zero-plane displacement as functions of canopy height and area index. (Research Note) *Boundary-Layer Meteorol* 71: 211-216,
- Raupach MR, Finnigan JJ, Brunei Y (1996) Coherent eddies and turbulence in vegetation canopies: the mixing-layer analogy. *Boundary-Layer Meteorol* 78(3):351–382
- Ross A (2008) Large-eddy simulations of flow over forested ridges. *Boundary-Layer Meteorol* 128(1):59–7
- Thom AS (1971) Momentum absorption by vegetation. *Q J R Meteorol Soc* 97:414–428
- Tran T, Chakraborty P, Guttenberg N, Prescott A, Kellay H, Goldberg W, Goldenfeld N, and Gioia G (2010) Macroscopic effects of the spectral structure in turbulent flows. *Nature Physics* 6 (6): 438
- Yang XIA, Meneveau C (2016) Large eddy simulations and parametrisation of roughness element orientation and flow direction effects in rough wall boundary layers. *J Turbul* 17:1072–1085
- Yang XIA, Sadique J, Mittal R, Meneveau C (2016) Exponential roughness layer and analytical model for turbulent boundary layer flow over rectangular-prism roughness elements. *J Fluid Mech* 789:127–165
- Yi C (2008) Momentum transfer within canopies. *J Appl Meteorol Clim* 47:262–275

Wang W (2012) An analytical model for mean wind profiles in sparse canopies. *Boundary-Layer Meteorol* 142(3):383–399

Wang W (2014) Analytically modelling mean wind and stress profiles in canopies. *Boundary-Layer Meteorol* 151(2)239–256

Chapter 3

3 Numerical estimation of external convective heat transfer coefficient for buildings in an urban-like setting

3.1 Introduction

The discrepancy between predicted energy demand during design, and the actual measured building energy use post-occupancy has been a long-standing problem; now in the industry, it is referred as “the performance gap” (van Dronkelaar et al. 2016, Bordass et al. 2013, Burman et al. 2012, Menezes et al. 2012; Turner et al. 2008, Bordass et al. 2001). Menezes et al. (2012) have listed possible causes for this discrepancy. It is stipulated that improvements in thermo-fluid modeling of flow in and around the building envelope are consistently contributing to narrowing the performance gap. Recently, Chen et al. (2017), reported the two most important sources of uncertainty in achieving robust building performance are the convective heat transfer coefficient and microclimatic properties. There is a significant discrepancy in measured and simulated CHTC correlations (Evangelisti et al. 2017, Mirsadeghi et al. 2013, Defraeye et al. 2011, Emmel et al. 2007); attributed mainly to the specific conditions under which each study is conducted. The largest CHTC could be 5 to 10 times the smallest (at low wind speeds), based on models derived from field and lab experiments (Chen et al. 2017). This variation further widens as the wind speed becomes higher or the study building is located in urban areas. The

uncertainty related to microclimatic changes in urban spaces arises from the deviation of actual flow parameters at the urban site in relation to the records at the meteorological station, commonly located at airports. Surrounding terrain difference, building forms, and arrangements affect the local urban microclimate (Moonen et al. 2012, Blocken et al. 2011, van Hoof et al. 2010, Franke et al. 2007, Coceal et al. 2004, Macdonald 2000, Stathopoulos et al. 1995, Oke 1988). Adamek et al. (2017) have shown how a city development and related urban topology change affect microclimate near buildings.

The variation of urban morphology (as expressed by packing density) results in changes in the value of CHTC measured from building surfaces (Liu et al. 2013). However, most existing models used for estimating CHTC are derived from studies on isolated bluff body by using either CFD studies (Montazeri et al. 2015, Blocken et al. 2009, and Emmel et al. 2007) or scaled experiments (Nakamura et al. 2001, Natarajan et al. .1994; Meinders et al. 1999, Chyu et al. 1991). Some useful insights are obtained from flat plate studies (Jurges 1924; Sparrow et al. 1979). The effect of the sheltering from neighboring buildings has only been considered in site/configuration-specific studies (Mirsadegi et al. 2013, Liu et al. 2015, Allegrini et al. 2012, Liu et al. 2007). The influence of terrain conditions and the incident turbulence on buildings' CHTC has been studied by Blocken et al. (2009), and Karava et al. (2011).

Mirsadeghi et al., 2013, Defraeye et al. 2011, and Palyvos 2008 presented an extensive review of literature on the external convective heat transfer coefficient. Several CHTC correlations exist that are found from field and lab experimentation (Vereecken et al. 2018, Evangelisti et al. 2017, Liu et al. 2007, Hagishima et al. 2003, Loveday et al. 1996, Jayamaha et al. 1996, Sharples 1984, Sparrow et al. 1979, Kelnhofer and Thomas 1976,

Ito et al. 1972, Jürges 1924) or numerical simulations Kays et al. 2018, Montazeri et al. 2017, Montazeri et al. 2015, Liu et al. 2013, Defraeye et al. 2010, Blocken et al. 2011, Blocken et al. 2009, Emmel et al. 2007). In most of these correlations, the CHTC relates only to wind speed. Recently, Montazeri et al. (2015) and Kays et al., 2018; stated that CHTC is also altered by the dimensions of the building.

The most general form of CHTC correlations in surveyed literature is a power-law function of u_{10} (linear expressions also exist for CHTC expressions that include free convection conditions); as,

$$h = a_1 u_{10}^m \quad \text{Eq.3.1}$$

where h is the surface averaged external convective heat transfer coefficient, u_{10} is the velocity at 10 m height from ground at the measurement station, a_1 and m are constants.

In most of these CHTC expressions, the terrain changes from the meteorological site, where u_{10} is measured, to the study building site is not considered. One exception to this is the application of height varying CHTC because of the increase in wind speed along with height, through the account of roughness and transition between the two exposure conditions. In general, this consideration involves the assumption of the velocities at both downstream and upstream locations as power-law (or log law) profiles (ASHREA 2009). i.e.,

$$u_H/u_{10,met} = [(\delta_{met}/10)^{\alpha_{met}}(1/\delta)^{\alpha_s}]H^{\alpha_s} \quad \text{Eq.3.2}$$

where u_H is the velocity at distance H from the ground at the study building site, $u_{10,met}$ is the velocity at a distance of 10 m from the ground at the measurement station, δ_{met} is the

wind boundary layer thickness at the meteorological station, δ is the wind boundary layer thickness at the study building site, α_{met} is the power-law wind profile exponent at the meteorological station site, α_s is the power-law wind profile exponent at the study building site,

The expression in the bracket (Eq.3.2), contributing to the coefficient a_1 in Eq.3.1, represents mesoscale exposure characteristics at the two locations (Wieringa 1992, Davenport 1960). However, flow at suburban or urban exposure goes through significant microclimatic changes, especially near the building/surface level. The coefficient a_1 , in Eq.3.1, does not fully represent the compactness or lessening of built area density that may be present in an urban arrangement. Discussion of microclimatic changes due to perturbations of urban packing density (the nature of aggregation of the built system) is widely available (Castro 2017, Coceal et al. 2004, Macdonald 2000, Oke 1988). Researchers in urban canopy and plant canopy fields have also widely reported that the velocity profile in canopies (urban and plant) does not follow the power-law or log law form (Awol et al. 2017, Wang 2014, Coceal et al. 2004, Cheng et al. 2002, Macdonald 2000, Cowan 1968, Cionco 1965). These studies show spatially averaged velocity profile in urban canopies is dependent on the density of the urban arrangement. Eq.3.1 and Eq.3.2 reflect the flow above the effective aerodynamic roughness; however, they do not reflect the microscale changes in the flow within urban canopies. This is one of the major reasons for large uncertainty in the CHTC estimation models.

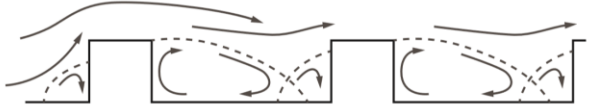
The first attempt to relate urban packing density to convective heat transfer has been made by Lui et al. (2013). Lui et al. (2013) used upstream flow parameters derived for buildings placed in an urban setting, which are specifically represented by arrays of cubes. They used

modified aerodynamic roughness values proposed by Macdonald (2000). However, the aerodynamic roughness values, along with the displacement height values proposed by Macdonald (2000), were to improve the estimation of the mean velocity profile in the inertial range. The two parameters (i.e., aerodynamic roughness, and the displacement height) help obtain a displaced logarithmic mean velocity profile that better fits to the velocity profile above the canopies. With the use of these parameters, the canopy layer velocity profile will not be properly reproduced. Moreover, the use of different upstream aerodynamic roughness values and hence different upstream mean velocity profiles makes the comparison of results problematic.

On a pioneer work by Oke (1988), the flow around a pack of idealized buildings is studied. Oke (1988) identified three distinct regimes of flow, having different flow structures based on proximity between the various obstacles. The first being where the spacing between buildings can be very large compared to the height (or $H / S < 0.2$), in which case the wake from one of the obstacles hardly influences the flow around an obstacle downstream. In this case, called an isolated roughness regime, the flow field starts to, gradually, change from that around a purely isolated obstacle. The second flow regime is called wake interference. In this case, there is significant interaction from the wake of an obstacle on an obstacle downstream; and this condition is distinguished by pronounced mass exchange (besides momentum / turbulent shear) between the flow under the canopy and the one over it. In the third regime, the flow above the canopy skims over the obstacles, and there exists a counter-current vortex trapped in the spaces between the obstacles. Exchanges in momentum due to turbulent shear at the top of the canopy are believed to drive the counter-

flow under the canopy. Table 3.1 summarizes the flow regimes at different canopy densities with a schematic description.

Table 3.1 Flow regimes at different canopy density with a schematic description

| H/S | Flow regime (Oke 1988) | Schematic description |
|--------------------|---|---|
| $H/S < 0.2$ | Isolated roughness |  |
| $0.2 < H/S < 0.65$ | Wake interference |  |
| $H/S > 0.65$ | Skimming |  |

Packing density has been used as an expression of aggregation of an urban built system. There are two ways in which packing density has been defined, namely the frontal and planar forms of aggregation.

The presence of bluff bodies in urban environments is commonly simulated in research by idealized roughness elements, an array of the inline or staggered arrangement of small-scale objects (e.g., cubes) mounted on a wall. Here the cube heights are meant to represent the average height of the roughness. Most of these investigations are laboratory experiments (Yang et al. 2016, Macdonald 2000, Cheng et al. 2002) and some CFD simulations (Castro 2017, Yang et al. 2016, Abdi and Bitsuamlak 2016, 2014, and Coceal et al. 2006).

In general for canopies, the frontal packing density (λ_f), planar packing density (λ_p) are expressed as;

$$\lambda_f = \frac{A_f}{A_d}, \lambda_p = \frac{A_p}{A_d} \quad \text{Eq.3.3}$$

where A_f is the frontal area, A_p is the planar, and A_d is the unit underlying lot area on the ground surface (Figure 3.1).

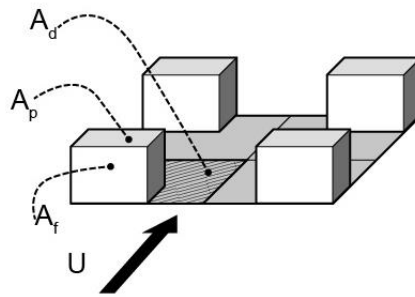


Figure 3.1 Description of areas used to determine a density parameter.

The frontal area, A_f , represents the area of obstruction exhibited by the flow due to obstructing elements. Other packing density considerations may employ the planar area density, A_p ; representing the average area of horizontal planar projection cast by the obstacles. In most urban canopy flow simulations, buildings are represented by arrays of cubes, implying equal frontal and planar area indices ($A_f = A_p$). For which,

$$\lambda_f = \frac{H^2}{(S+H)^2} = \frac{1}{\left(1 + \frac{S}{H}\right)^2} = \lambda_p \quad \text{Eq.3.4}$$

where H is the cube height, and S is the spacing between adjacent cubes.

This study aims to perform a CFD investigation of the influence of urban packing density on CHTC. A set of uniform distribution but different density cases are simulated from each flow regime. The same input conditions and the computational domain is set up for all cases. The validation, computational set up, and results of the study are discussed in the following sections.

3.2 Computational evaluation of CHTC on building in urban-like setup

Steady Reynolds Averaged Navier-Stokes (RANS) and the energy equations are implemented to solve the problem in a CFD environment. The turbulence model, computational domain set up, input preparation, grid generation and simulation procedure for the main research are presented in the following sections.

3.2.1 Turbulence model

The turbulence scheme that will be used in the study is the second-moment closure method, Reynolds stress turbulence model (RSM). This method is important for flows like the present investigation where secondary flows and anisotropic turbulence are substantial (Speziale 1991, Murthy et al. 2008, Leschziner 1990, Launder et al. 1975).

3.2.2 Computational set up of the simulated array

CHTC from surfaces of an isolated building and 13 other building densities are investigated. Out of these, 4 are from the isolated flow regime, 5 in the wake interference regime, and another 4 in the skimming flow regime. The buildings are cubical in shape

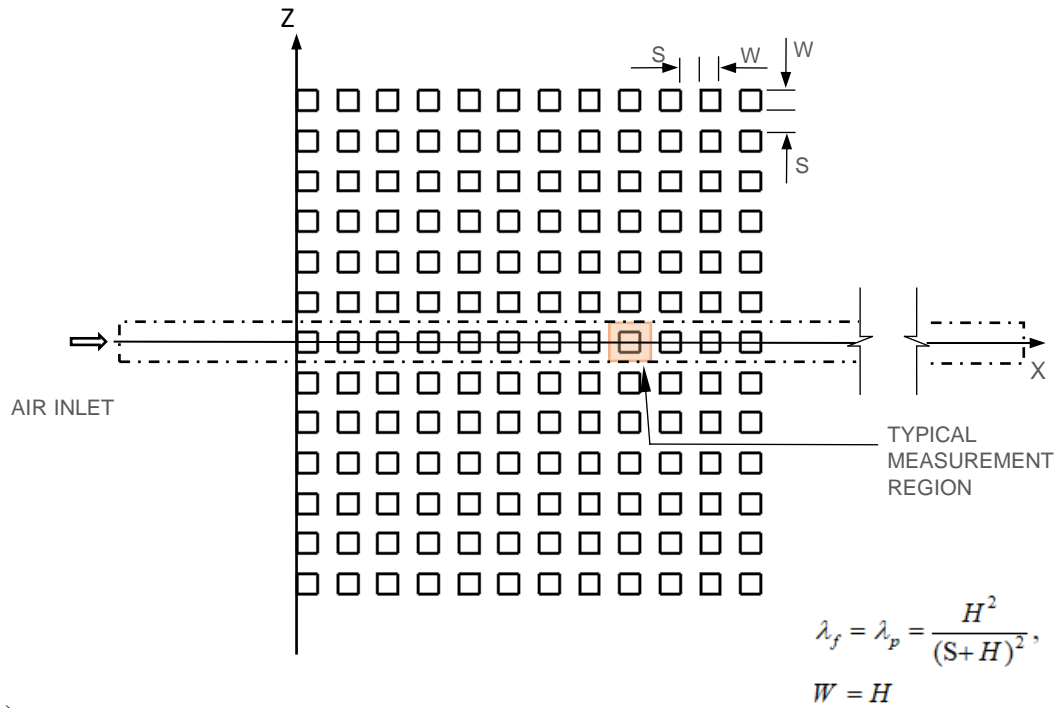
with sizes varying depending on the density. The densities and corresponding building sizes are shown in Table 3.2.

Table 3.2 Density and size of cubes considered from each regime

| Isolated flow regime | | Interference flow regime | | Skimming flow regime | |
|-----------------------------|----------|---------------------------------|----------|-----------------------------|----------|
| <i>Built Area Density</i> | <i>H</i> | <i>Built Area Density</i> | <i>H</i> | <i>Built Area Density</i> | <i>H</i> |
| A single cube | 13.45 | 0.05 | 9.5 | 0.175 | 17.78 |
| 0.01 | 4.25 | 0.075 | 11.64 | 0.02 | 19 |
| 0.015 | 5.2 | 0.10 | 13.45 | 0.225 | 20.16 |
| 0.02 | 6.01 | 0.125 | 15.03 | 0.25 | 21.25 |
| 0.025 | 6.7 | 0.15 | 16.45 | | |

Each representative urban density is obtained from a hypothetical 2D array of 14 cubical buildings stream-wise, with infinite array size in transverse. For such an array system, a representative flow can be obtained from the simulation of a longitudinal strip of the array system. This requires the assumption of a symmetry boundary condition on the two parallel planes, normal to the transverse direction, each half spacing away from the selected row of cubes for study (as shown in Figure 3.2). The limits of the simulation domain are shown in Figure 3.2, and its dimensions are shown in Figure 3.3.

a)



b)

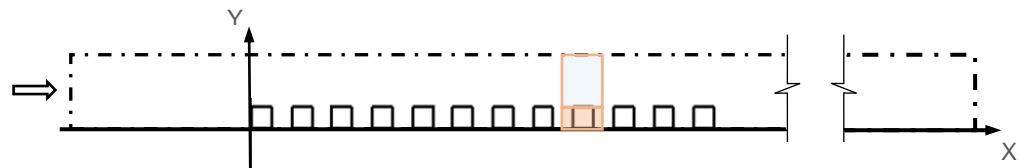


Figure 3.2 The building array with the study section (broken lines) and spacing parameters indicated on a) plan and b) elevation views.

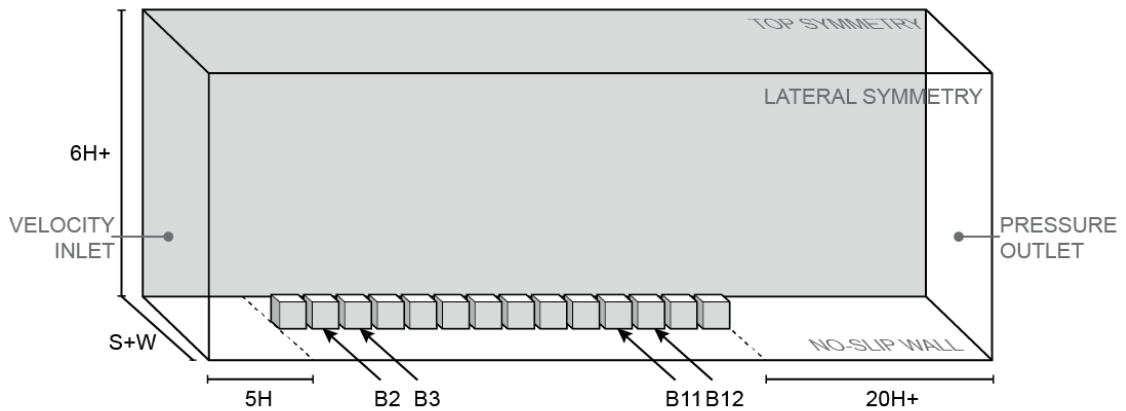


Figure 3.3 The computational domain, its dimensions and boundary conditions (H height of cubic = 21.25 m).

The choice of the cubes' dimensions is such that the same domain and boundary conditions are used for all computational simulations. Accordingly, the domain is set up for the highest density (building size) case considered using Tominaga et al. (2008) and Franke et al. (2011). The domain's downstream length is stretched to $20H$ to ensure that flow re-development is attained behind the wake region. Accordingly, the domain's height and downstream fetch may exceed the $6H$ and $15H$ values for the lower density cases.

Vertical planes running along the longitudinal direction of the flow, standing midway between buildings, are assumed symmetry planes. The top surface of the domain, as well, is kept far enough from the top of the building so that it can be assumed symmetry plane. The bottom surface of the domain is assigned an adiabatic no-slip wall. The cube surfaces are wall boundaries at a uniform temperature of $30\text{ }^{\circ}\text{C}$. A pressure outlet condition (zero longitudinal gradient) is applied at the outlet of the domain.

The inlet boundary is an atmospheric boundary layer wind extracted from Engineering Science Data Unit (ESDU). The mean velocity profile has a velocity $u_{10} \approx 4\text{ m/s}$ at 10 m height in a suburban exposure condition (of aerodynamic roughness, $z_0 = 0.1$); corresponding to an upstream open terrain profile of $u_{10} = 4.7\text{ m/s}$ at 10 m height with an aerodynamic roughness of $z_0 = 0.01$). The turbulence properties implemented at the inlet are the three principal components of the Reynolds stress tensor. These values are obtained from the components of turbulent intensity and length scale tensor values provided by ESDU (corresponding to the mean velocity and aerodynamic roughness combination

mentioned above). Figure 3.4 shows the mean velocity and the principal components of the Reynolds stress values implemented.

The Reynolds stress tensor components at the inlet are obtained using the equation,

$$R_{ii} = 2[\varepsilon L_{ii}/C_{\mu}^{3/4}]^{2/3} \quad \text{Eq.3.5}$$

where ε is the dissipation rate, L_{ii} is the component length scale obtained from the ESDU, C_{μ} is the model constant approximated, commonly, by 0.09.

The dissipation rate at inlet and can be calculated from,

$$\varepsilon = k^{3/2}/L \quad \text{Eq.3.6}$$

where the k refers to the turbulent kinetic energy, and L is the turbulent length scale at the inlet. The kinetic energy and the length scale can be found from Eq.3.7 and Eq.3.8.

$$k = \frac{1}{2} \left[\sqrt{(u_i')^2 + (u_j')^2 + (u_k')^2} \right] \quad \text{Eq.3.7}$$

$$L = \sqrt{(L_{ii})^2 + (L_{ii})^2 + (L_{ii})^2} \quad \text{Eq.3.8}$$

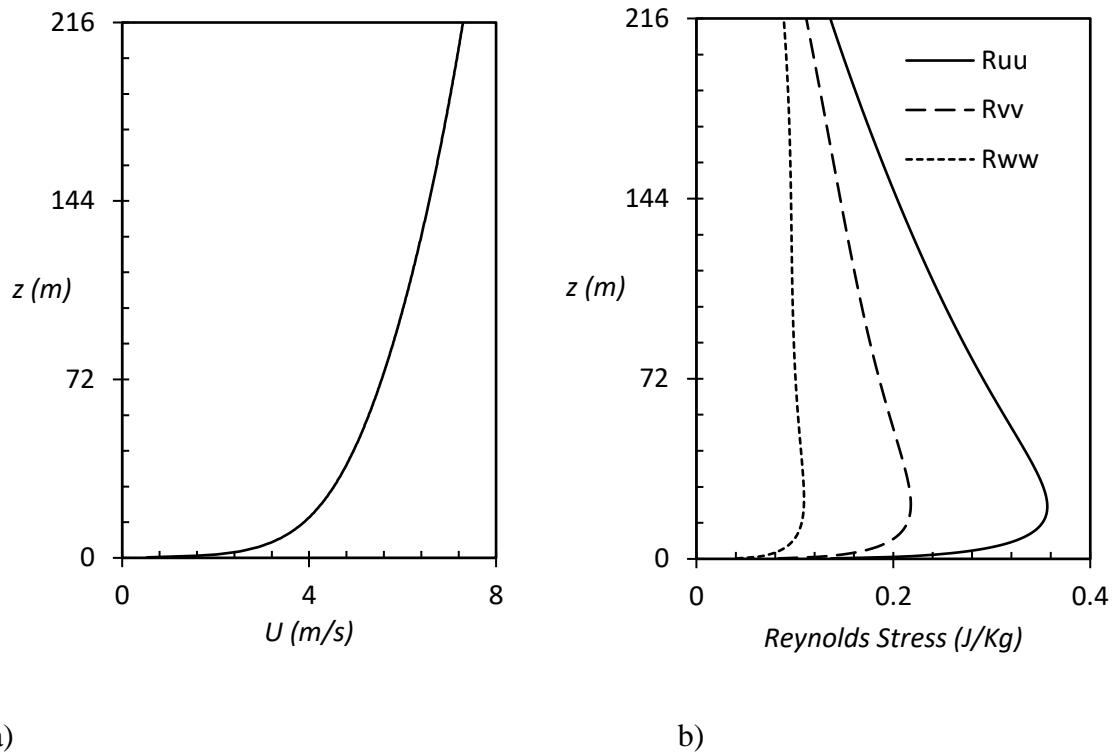


Figure 3.4 The inlet profiles a) mean velocity and b) the principal components of Reynolds stress

The mean velocity profile that has been used for the isolated building investigation case is corresponding to the value of $u_{10} = 1, 2, 3, 4$ and 5 m/s at 10 m height from the ground for an open terrain exposure with an aerodynamic roughness of $z_0 = 0.01$. The incoming air temperature in all the cases is set at 20°C .

3.2.3 Grid generation

The generated grid has approximately $1.5 \cdot 10^6 - 2.5 \cdot 10^6$ polyhedral cells. Refinements are applied to a volume around the cubes, on the cube surfaces, cube edges, to the wake region, and the computational domain wall boundary. Five layers of grid near the wall boundaries are made prismatic (i.e., running parallel to the local surface). The width of the nearest cell

to the surface is stretched by about 1.5 times its thickness. This would allow for better interpolation where the change of gradients is the highest. The ensuing computational mesh has a y^+ value of 40 - 110, where the lowest values are near the cube bases. The corresponding wall function (the 'all y^+ treatment') is adopted for the given range of y^+ values. The sensitivity of results to successive grid refinement states are checked; the converged states are used for the final simulation (Figure 3.5).

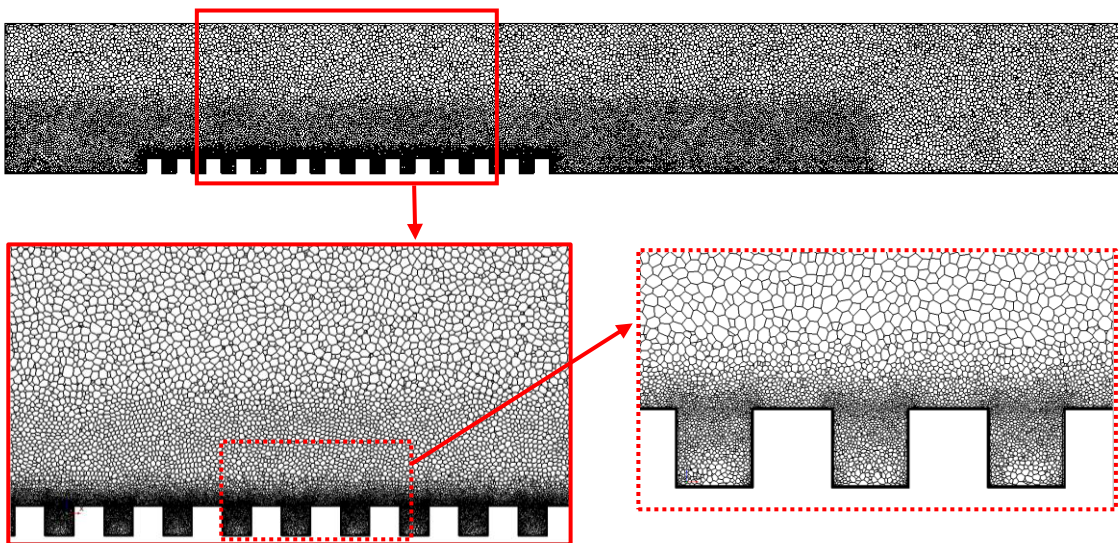


Figure 3.5 Elevation view of a sample mesh section

The grid-sensitivity for a typical simulation set with $\approx 4.5, 3.5, 2.5$ million cells (corresponding to y^+ values of $\approx 20, 30, 75$, and 90 near the building surfaces, respectively) is tested. The results obtained have shown no significant changes ($<3\%$) to the measured value of CHTC for all orientations except the leeward side (Figure 3.6). The maximum error obtained in the measured value of CHTC ($\lambda = 0.075$) on the leeward surface is 11% . This may be because the leeward surface is fully engulfed in the wake region. This may be

considered small as the leeward surface contributes the least portion to the overall CHTC of the building surfaces.

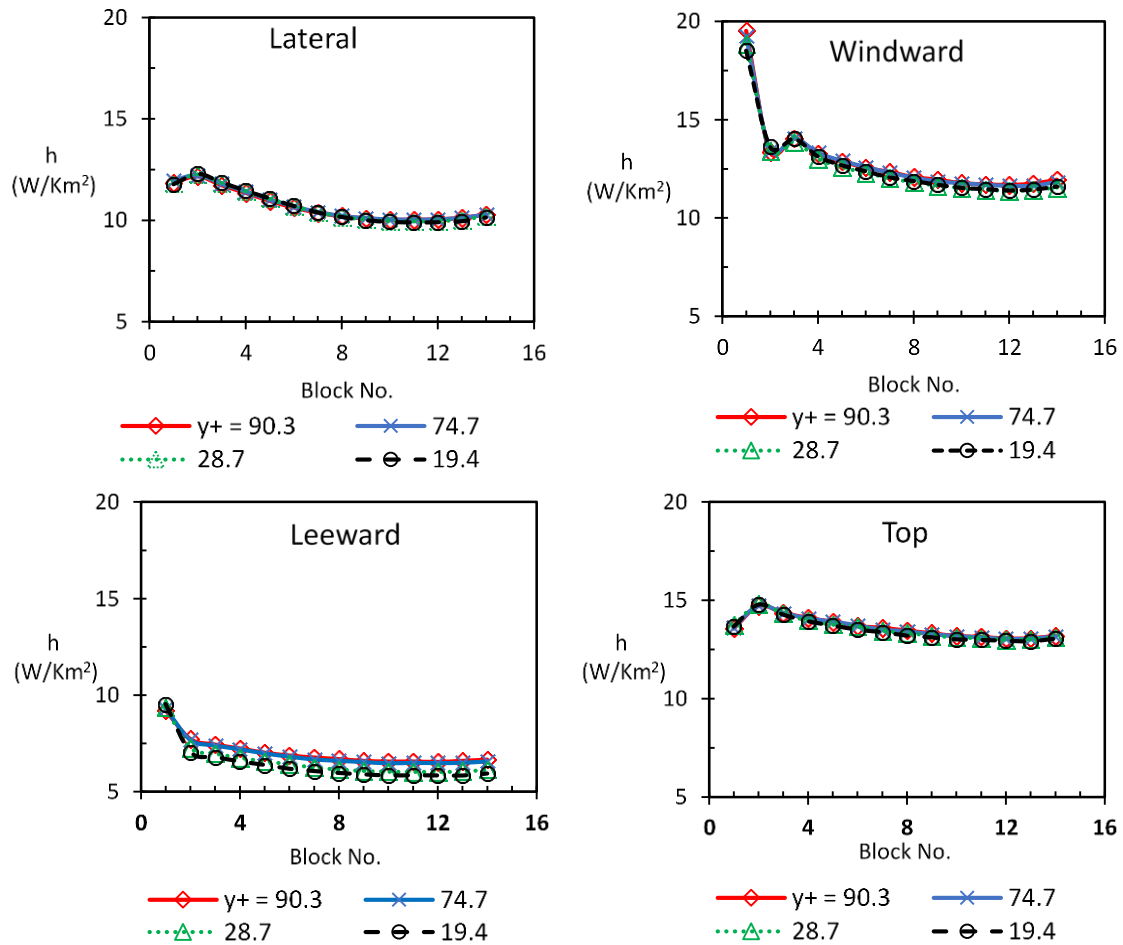


Figure 3.6 The sensitivity of surface average CHTC for various grid resolution for all surface orientations

3.2.4 Calculation of CHTC

Firstly, the nodal CHTC ($CHTC_p$) is obtained using the standard wall function formulation:

$$CHTC_p = \frac{\rho(y_p)C_p(y_p)u_*}{T^+(y^+(y_p))} \quad \text{Eq.3.9}$$

where ρ is air density, C_p is specific heat capacity of air, u_* is the friction velocity, y_p and T_p are distance along the surface normal and temperature of the near-wall cell, respectively, $y^+ = u_*y_p/\nu$ is the dimensionless wall distance, ν is the kinematic viscosity, and T^+ is the near cell dimensionless temperature obtained analytically from Kader (1981) wall function for temperature distribution.

The CHTC reported in this paper is obtained using an upstream, undisturbed, reference temperature T_{ref} , that is unaffected by the presence of the buildings. Therefore, the post-processing of the reported CHTC is based on,

$$CHTC = CHTC_p \frac{(T_s - T_p)}{(T_s - T_{ref})} \quad \text{Eq.3.10}$$

where T_{ref} the inlet flow temperature, T_s is the surface/wall temperature applied and $CHTC_p$, and T_p is determined from values at the near-wall cell in the CFD simulation.

3.3 CFD Validation

The validity of a CFD simulation is only ascertained after the results of the procedure are verified. To this end, validation is conducted against (i) an experimental finding of a closely similar setup for an array of model scale obstacles and (i) full-scale simulation for an isolated building.

3.3.1 CFD validation against experimental work

The validity of a CFD simulation is only ascertained after the results of the procedure are verified by an experimental finding of a closely similar setup. Experimental evaluation of heat transfer from surfaces of cubes in an array is performed by Meinders et al. (1998). In the present simulation, the experimental geometry of Meinders (1998) is replicated in a CFD environment. The results obtained are then compared against the experimental findings.

The Meinders (1998) experiment is performed in a wind tunnel with a 500 mm x 50 mm test section. A row of 9 (nine) cubes aligned in the streamwise direction mounted in the middle of the vertical channel wall. The cube size and the spacing between the cubes are 15 mm each. The cube is made of a 1.5 mm shell of epoxy layer and an internal copper core. The copper core is maintained at a temperature of 75 °C, and the epoxy material has a conductivity of approximately 0.24 W/m.K.

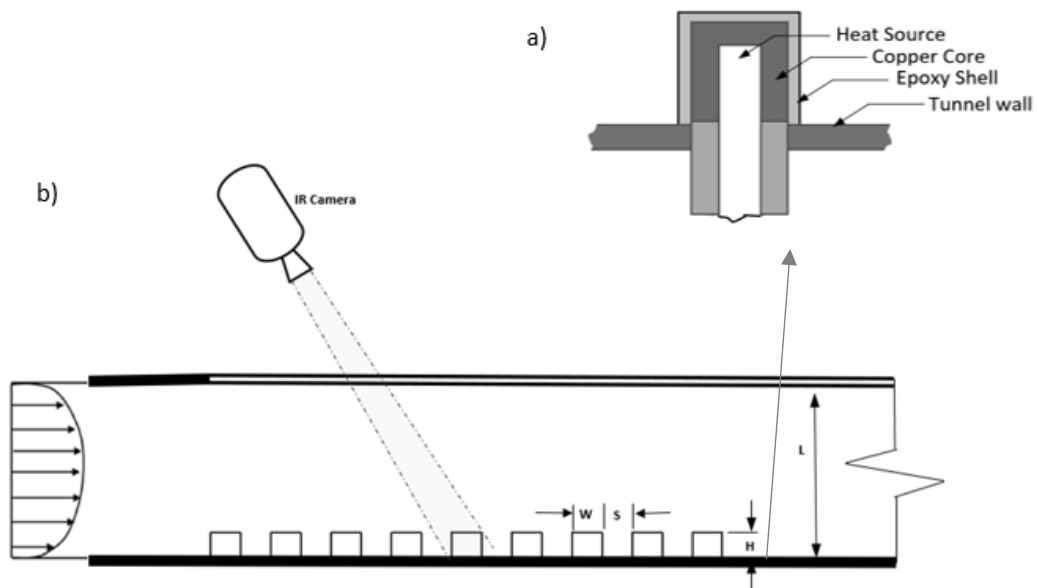


Figure 3.7 Schematic drawing of a) each cubical element, b) the setup of the experimental tunnel.

An infrared camera scans the external surfaces of the cubes to provide the temperature distribution that can again be used to calculate the convective heat transfer coefficient; after accounting for radiative losses from supply flux. The inlet is supplied with a bulk velocity of 5.1 m/s, corresponding to an approximate Reynolds number of 5065 based on the height of the cubes. The temperature of oncoming flow at the inlet is set at 21 °C. The schematic of the experimental set up is shown in Figure 3.7. Additional detail information can be found in Meinders (1998).

A 1:1 scale of the tunnel section is modeled in a CFD environment with the downstream fetch sized 20H, so that downstream wake effects are fully contained within the domain. Upstream fetch of 5H considered according to Tominaga et al. (2008) and Franke et al. (2011). The wall, on which the cubes are mounted, is oriented vertically to match the condition in the experiment, as shown in Figure 3.9. The building representation is such that a 1.5 mm thick cubical shell, of 15 mm outer size, is considered. The properties of epoxy material are used to allow for the calculation of conduction heat transfer through this shell. The inner surface of all 9 cube shells is set to be at a temperature of 75 °C. The cubes are mounted along the stream direction and spaced 15 mm apart from each other. The flow domain has an inlet and outlet surfaces at upstream and downstream of the row of cubes respectively. A temperature of 21 °C is applied to the incoming airflow. The outlet conditions are kept at zero pressure gradient. All lateral, top and bottom faces of the computational domain are considered adiabatic and no-slip wall boundaries; the same as it has been in the experiment. The outer surfaces of the cubes are set as no-slip walls, with non-adiabatic environmental conditions.

Close to 1.4 million polyhedral grid cells are generated and picked after sensitivity testing. There are about 6 layers of stretched prisms near all walls and building surfaces. Refinements are incorporated near the wall, buildings surfaces, and the wake region; to properly capture high gradient effects in these regions. The ensuing mesh produced a maximum y^+ value of around 5.

The lower near logarithmic and the middle uniform portions of the inlet velocity profiles are directly applied from the digitized table of the experimental inputs; provided in Meinders (1998). The upper laminar portion of the profile is obtained from the recycling of the profile for this portion in a smooth channel without the presence of the cubes (while fixing the lower and middle portion as given above throughout the iteration). The cycle is reiterated until the profiles at inlet and outlet have matched within 2 %. The same procedure is used to obtain the upper portion of the turbulent intensity profile, while the lower and mid sections are taken from the experiment. The velocity and turbulent kinetic energy inputs are shown in Figure 3.8.

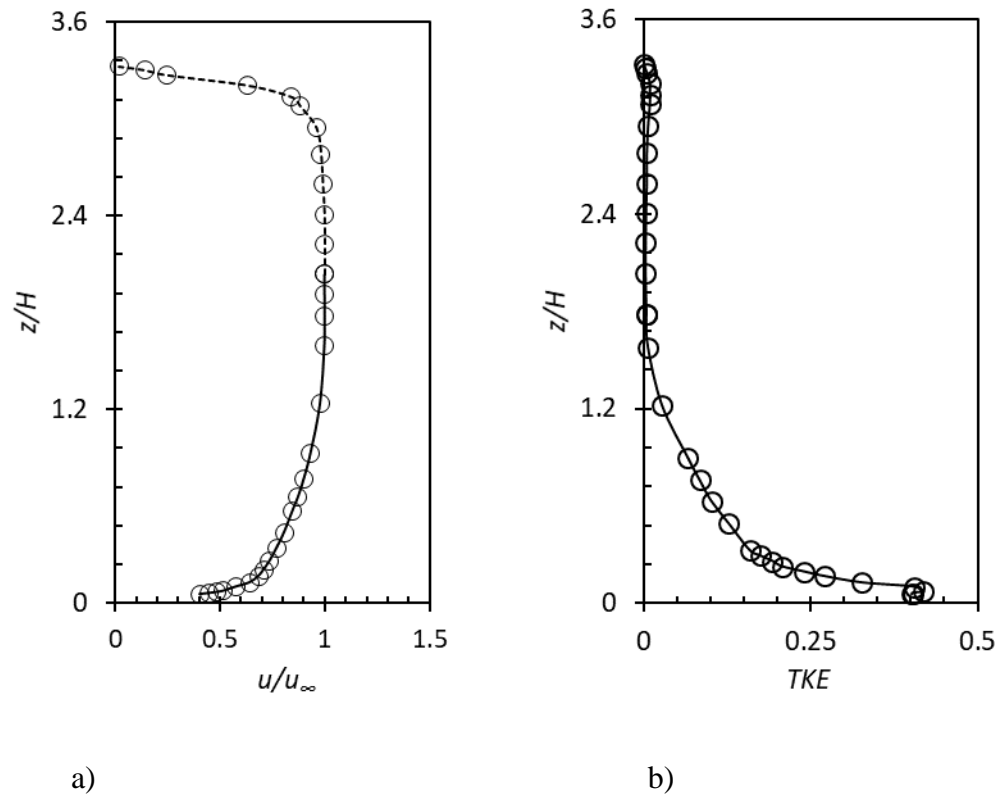


Figure 3.8 a) The adopted mean inlet velocity, b) turbulent kinetic energy profiles (solid line: experimental data; broken line: from re-cycling method; symbol: input to CFD)

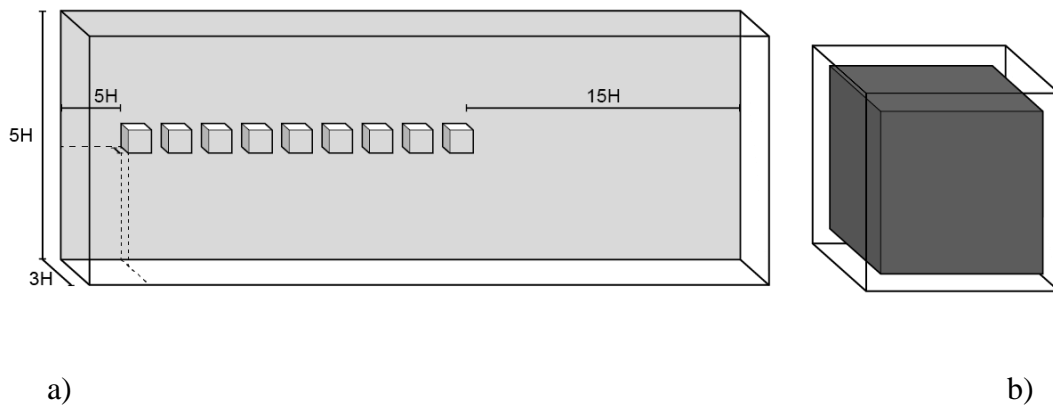


Figure 3.9 CFD implementation of the Meinders (1998) experimental setup a) the tunnel chamber b) each cubical shell element.

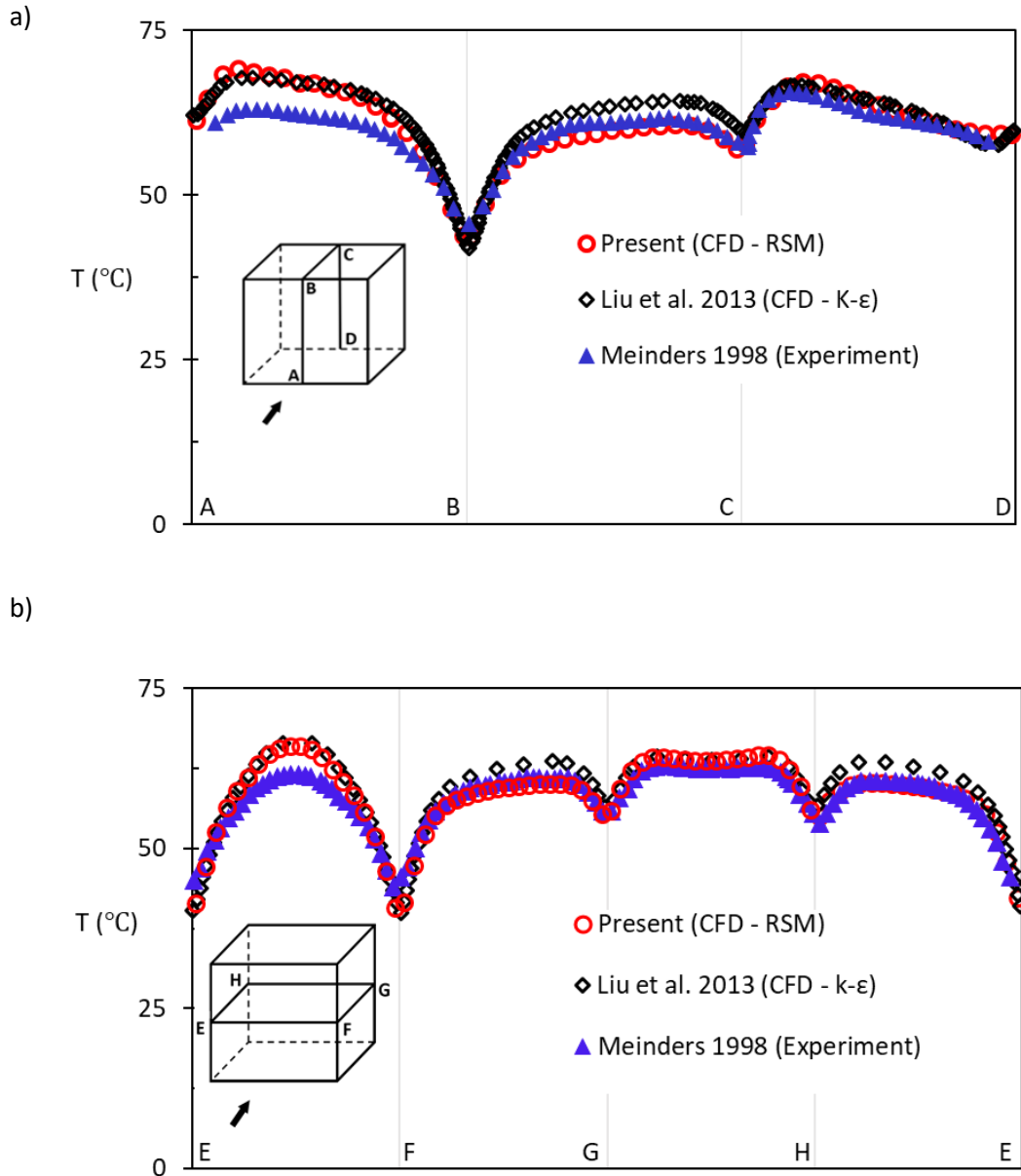


Figure 3.10 Comparison of simulated and experimental results along the paths: a) ABCD b) EFGHE

A comparison is made against the records of temperature at the surfaces of the 5th cube in the row. The results are collected at a vertical mid-line on the windward (AB) and leeward (CD) surfaces and a horizontal mid-line on the top (BC) surface of the 5th cube as shown in Figure 3.10a; corresponding to the longitudinal vertical plane section cutting midway

through the cubes. Liu et al. (2013) conducted the same measurement in a CFD environment with a k-epsilon, k-omega, and LES turbulence models. They found the k-epsilon model to perform better than the other two-equation model (k-omega). The results of the present measurement with Meinders (1998) and Liu et al. (2013), data obtained using the k-epsilon turbulence model, are indicated in Figure 3.10. On the top and leeward surfaces, the present RSM simulation can predict the experimental results well and better than the k-epsilon turbulence model simulation results. In the windward face, however, both the CFD simulations match but with a margin of error from the experimental records. This may have been due to uncertainty both from spatial coordinate (experimental cube and spacing are very small in size) and temperature measurement itself (Meinders 1998). The artificial introduction of inlet data in the uppermost boundary layer through the method of recycling may have some effects.

Additional data is collected at a horizontal mid-line on the windward (EF), lateral (FG, HE), and leeward (GH) surfaces of the 5th cube as shown in Figure 3.10b; corresponding to the horizontal section plane cutting mid-height of the cubes. The results of this data reinforce the remarks made above. In general, the present simulation reasonably predicts the temperature distribution on the surface of the building with an average deviation of less than 4 % from the experimental values.

3.3.2 CFD Validation against full-scale Numerical studies

The cubical building model is exposed to atmospheric boundary layer profile, with velocities of 1, 2, 3, 4, and 5 m/s at 10 meters from ground level. The aerodynamic roughness height is kept the same for all simulations, i.e., $z_0 = 0.01$. The detailed procedure

is as outlined in sections 3.1 - 3.4, except that a single cube with a building height of 13.5 meters is kept in the domain. The resulting windward surface CHTC value versus u_{10} data is fit to a power-law curve, as shown in the plot *Figure 3.11*. The results of these sets of simulations are compared against recent publications (Kahsay et al. 2018, Montazeri et al. 2015, Defraeye et al. 2010, Blocken et al. 2009). Among many sets, Montazeri (2015) considered simulations of CHTC for isolated cubes with heights $H = 10$ m and 20 m (with $W = H$). The coefficient and exponent of correlation obtained for the windward faces in the present simulation closely matched the values obtained by Montazeri et al. (2015), as shown in *Figure 3.11*.

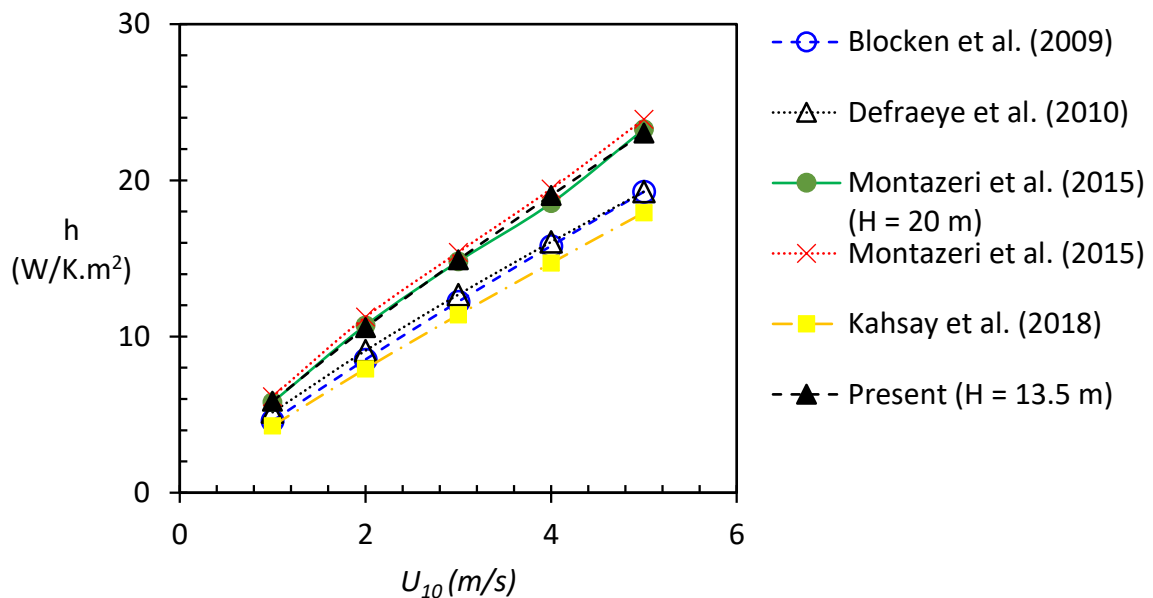


Figure 3.11 Comparison CHTC from windward surfaces against CFD studies by Kahsay et al. (2018), Montazeri et al. (2015), Defraeye et al. (2010), Blocken et al. (2009)

3.4 Results and discussion

Simulated velocity contours for three selected packing densities (0.01 from isolated flow, 0.1 from interference flow, and 0.25 from skimming flow regimes) are shown in Figure 3.12 -14.

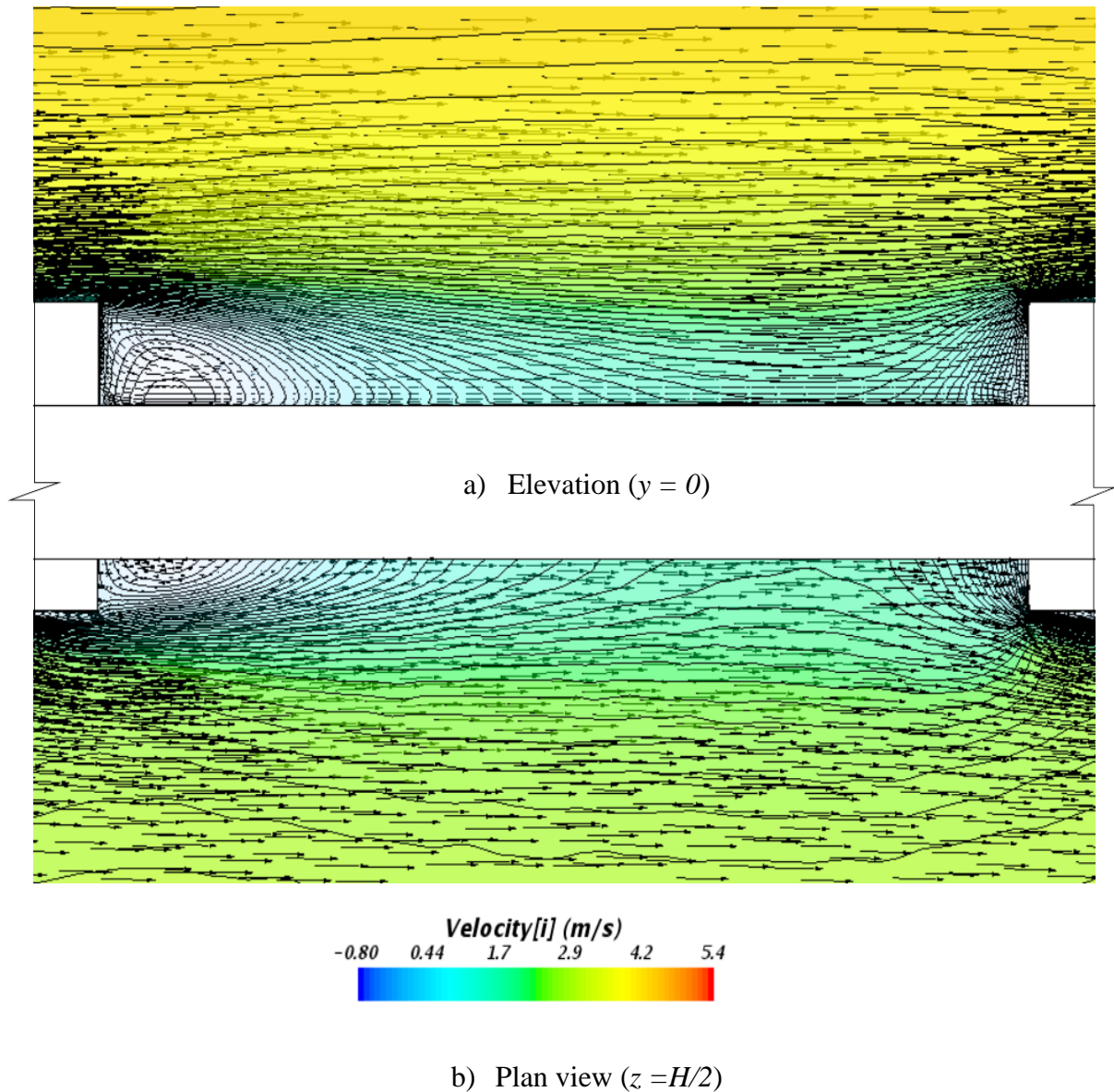
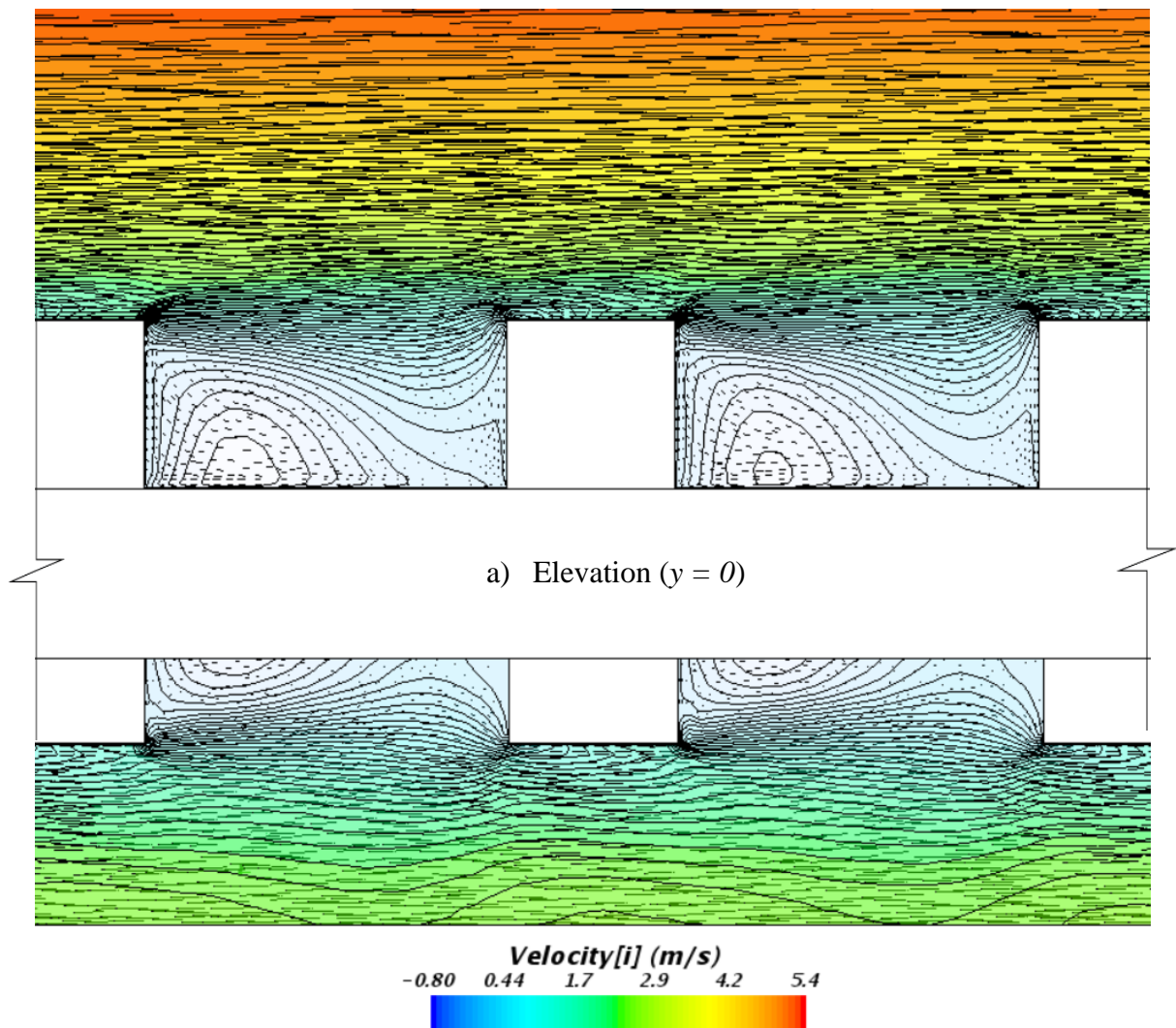


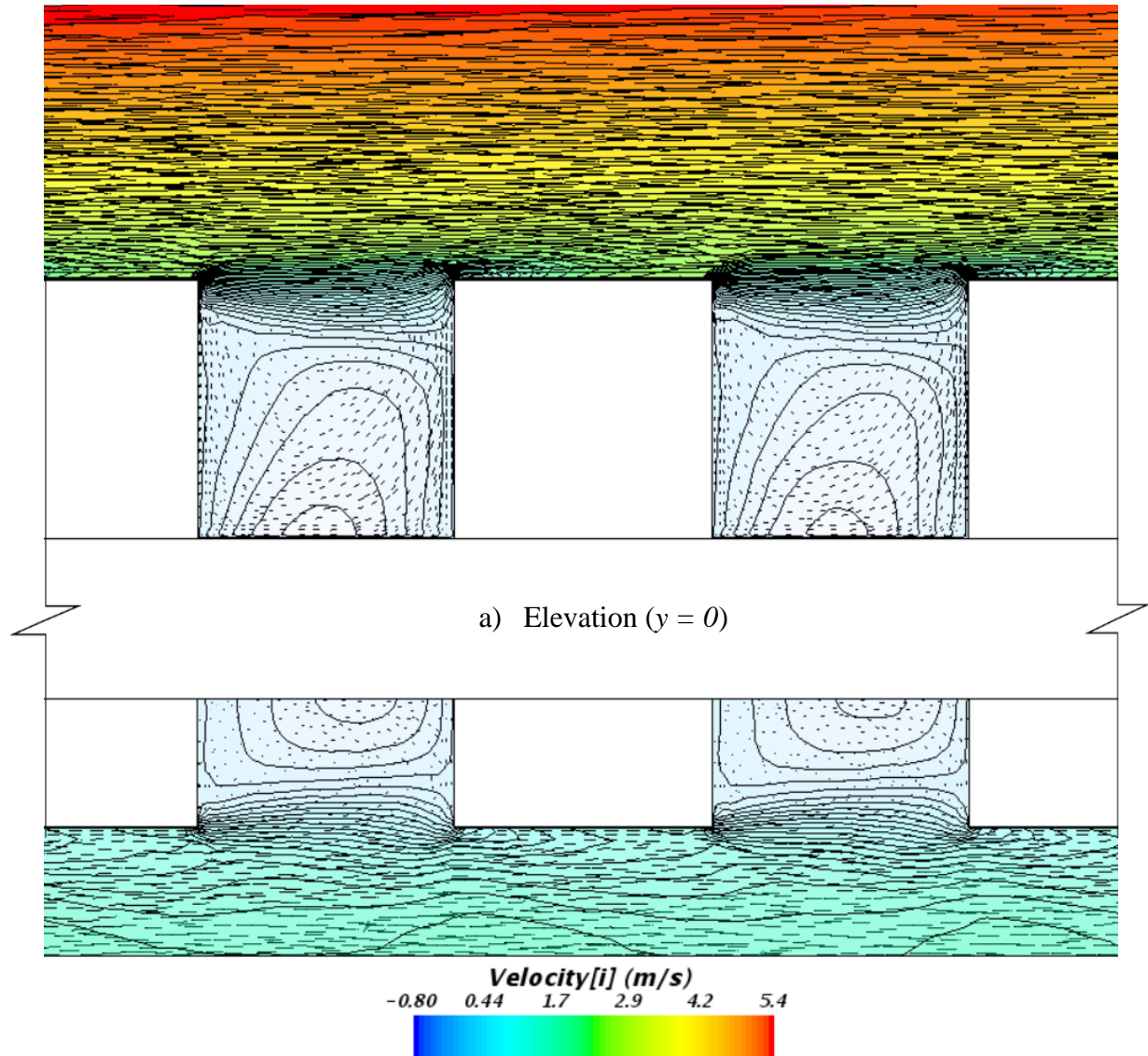
Figure 3.12 Velocity contours on vertical and horizontal section planes for $\lambda = 0.01$

In the $\lambda = 0.01$ case, it can be observed that the wake of a cube and the horseshoe vortices in front of a cube immediately downstream are physically separated, and the mean streamwise flow fills the spacing. However, in the $\lambda = 0.1$ case - corresponding to the interference flow regime, the wake and horseshoe vortices interact with each other while maintaining their locations. In larger densities, as in the case of $\lambda = 0.25$, the two vortices merge into one large counter flowing vortex trapped between the two cubes. In this scenario, the streamwise mean flow is observed to skim over the top of the vortex while driving its circulation.



b) Plan view ($z = H/2$)

Figure 3.13 Velocity contours on vertical and horizontal section planes for $\lambda = 0.1$



b) Plan view ($z = H/2$)

Figure 3.14 Velocity contours on vertical and horizontal section planes for the case of $\lambda = 0.25$

The convective heat transfer coefficient has been expressed in terms of velocity in many previous investigations. These expressions indicate the heat transfer coefficient is related to the power-law function of the wind velocity. It is noteworthy, however, that the wind velocity in urban areas is related to the aggregation or packing of the buildings in the site. Pertaining the above discussion, the following expression is hypothesized.

$$\frac{h}{u_{10}^m} \propto f(\lambda) \quad \text{Eq.3.11}$$

where the right-hand side of Eq.3.11 refers to a function dependent on the packing density, λ , and the orientation of each building surface (windward, leeward, lateral, and top).

3.4.1 Isolated building case ($\lambda = 0$)

Note that, from Eq.3.1 and Eq.3.11, $f(\lambda)$ is a constant when $\lambda = 0$ (isolated building case). This point can be, first, used to determine the value of the exponent m . Hence, the exponent m is first obtained from simulations conducted on an isolated building. The power-law fit curves for CHTC versus velocity (u_{10}) has been extracted from the CFD validation exercise on isolated cube, detailed in section 3.5. The values of m and C are found from the equations for these curves (Figure 3.15 and Table 3.4).

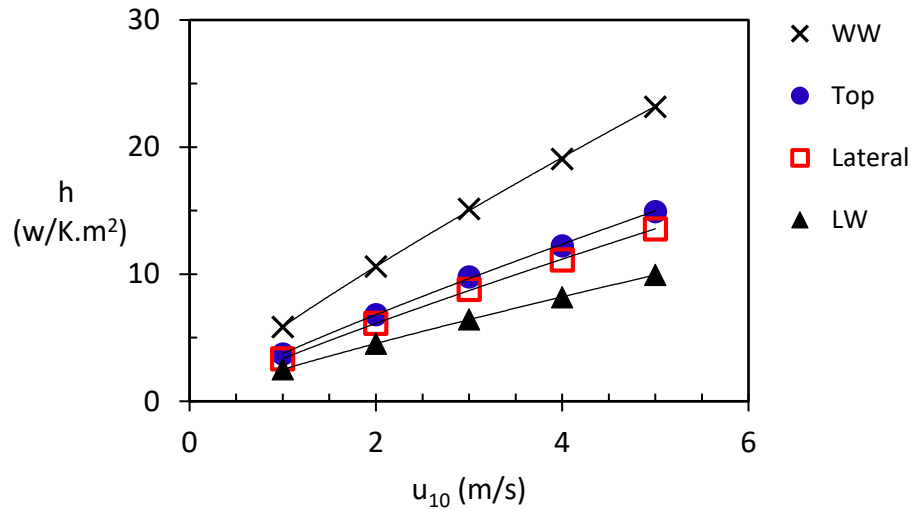


Figure 3.15 Heat transfer coefficient versus wind speed for an isolated cube

Table 3.3 The equations required to fit the data in Figure 3.15.

| Surface | Equation | Coefficient of determination (R^2) |
|-----------------|----------------------------|--|
| Windward | $h = 5.86 * u_{10}^{0.85}$ | 0.9999 |
| Top | $h = 3.75 * u_{10}^{0.86}$ | 0.9997 |
| Lateral | $h = 3.35 * u_{10}^{0.87}$ | 0.9999 |
| Leeward | $h = 2.51 * u_{10}^{0.85}$ | 1 |

The values of m obtained are 0.85, 0.86, 0.87, and 0.85 for the windward, top, lateral, and leeward surfaces respectively, as shown in the plot Table 3.4.

3.4.2 Building packing density $\lambda > 0$

According to Eq.3.11, if the upstream wind condition, u_{10} , is maintained the same for all simulations with varying density, the following holds true,

$$h \propto g(\lambda) \quad \text{Eq.3.12}$$

where the right-hand side of the Eq.3.12, $g(\lambda)$ is a function dependent on the packing density, λ , and the orientation of each building surface (windward, leeward, lateral and top). By fixing all upstream properties, the number of control variables is reduced. This enables us to establish the correct relationship between the remaining variables involved. The upstream conditions implemented in all the simulation cases are as described in section 3. Measurement of CHTC is conducted from cubes near downstream of the array (namely: 10, 11, and 12th cubes, as cubes counted from upstream), at which the flow development has been reached. Results presented in this paper are collected from the 11th cube of all cases for consistency purposes. According to Macdonald (2000) flow development is achieved at (and above) 20H from the leading cube. This can be reached at the 10th cube for the highest density tested, and earlier for the other densities. The trend of windward CHTC along the stream (along the cubes) for selected densities is shown in Figure 3.16. The values of CHTC at the downstream end of the array, where the flow is fully developed, becomes approximately constant as shown by the red box in Figure 3.16.

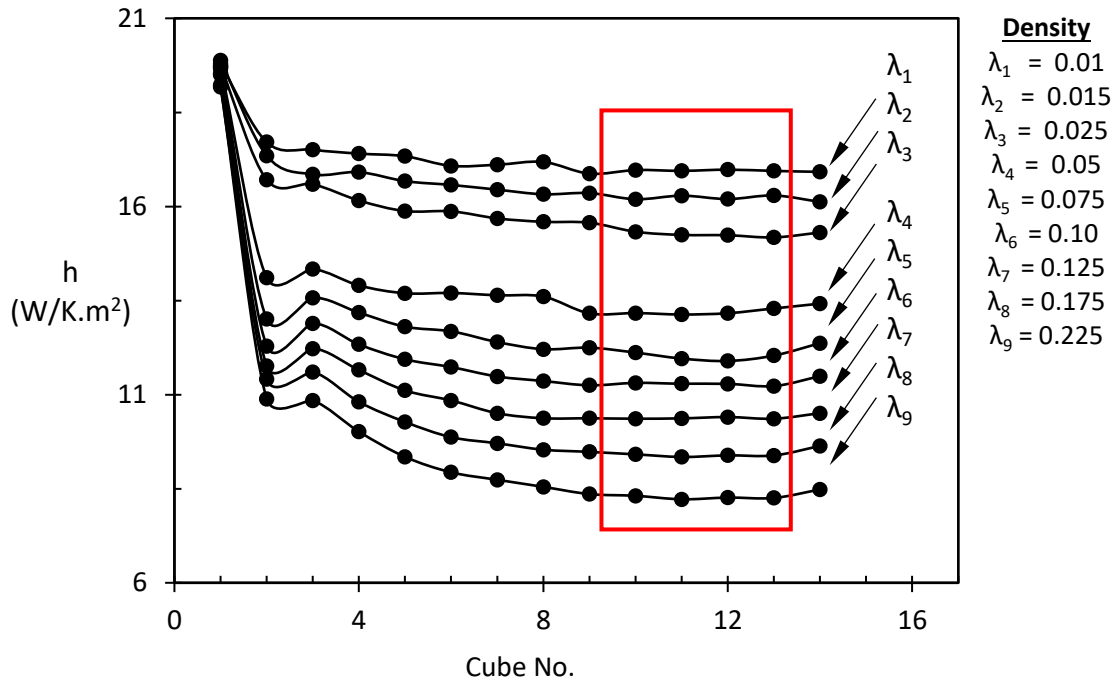


Figure 3.16 CHTC variation on the windward surface of each cube at several densities from upstream to downstream (i.e., cube 1 - 14)

The CHTC trend against density (λ) for all building surfaces is also shown in Figure 3.17 which reveals the trend of CHTC in the different flow regimes differs. More importantly, it is observed that in the *isolated flow regime*, the CHTC witnesses very drastic changes for alterations in density. Whereas CHTC in the *interference* and *skimming flow* regimes change relatively gently but with slightly different slopes. For this reason, two different simplified sets of correlations are suggested. The first for the isolated flow regime and the second for the combination of interference and skimming flow regimes. The general trend in the latter two regimes is, the CHTC decreases with an increase in density. This could reasonably be attributed to the relatively lower mean local wind velocity of flows in denser canopies. The decrease of mean velocity in denser canopies is well-known (Awol et al. 2017, Wang 2014, Coceal et al. 2004, Cheng et al. 2002, Macdonald 2000, Cowan 1968,

Cionco 1965). Contour plots in Figure 3.18 show the changes in CHTC over the surfaces for selected densities. This effect, however, has never been accounted for in widely used correlations, whose tests are based only on the investigation on isolated cubes.

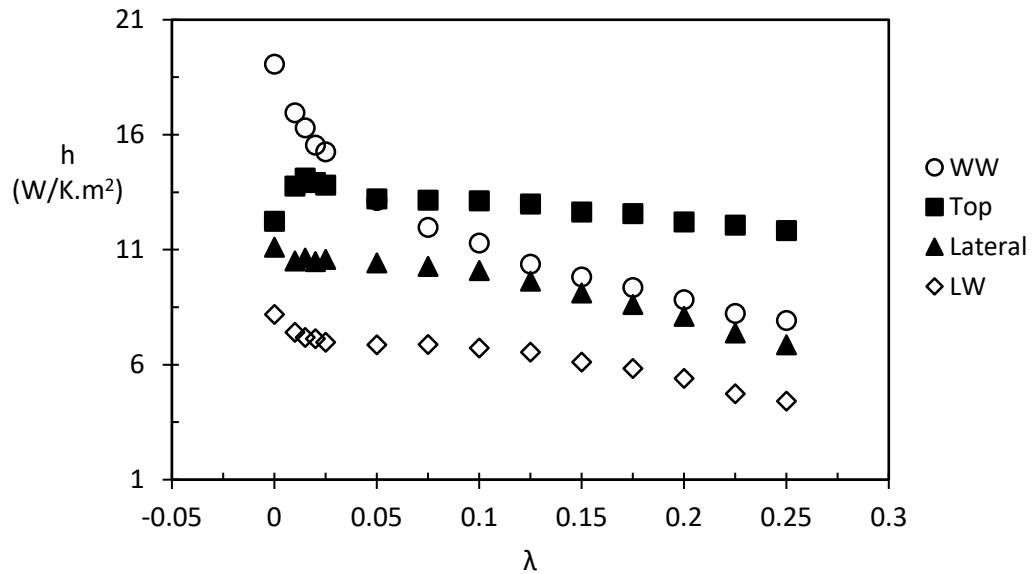


Figure 3.17 CHTC versus canopy density for each building surface

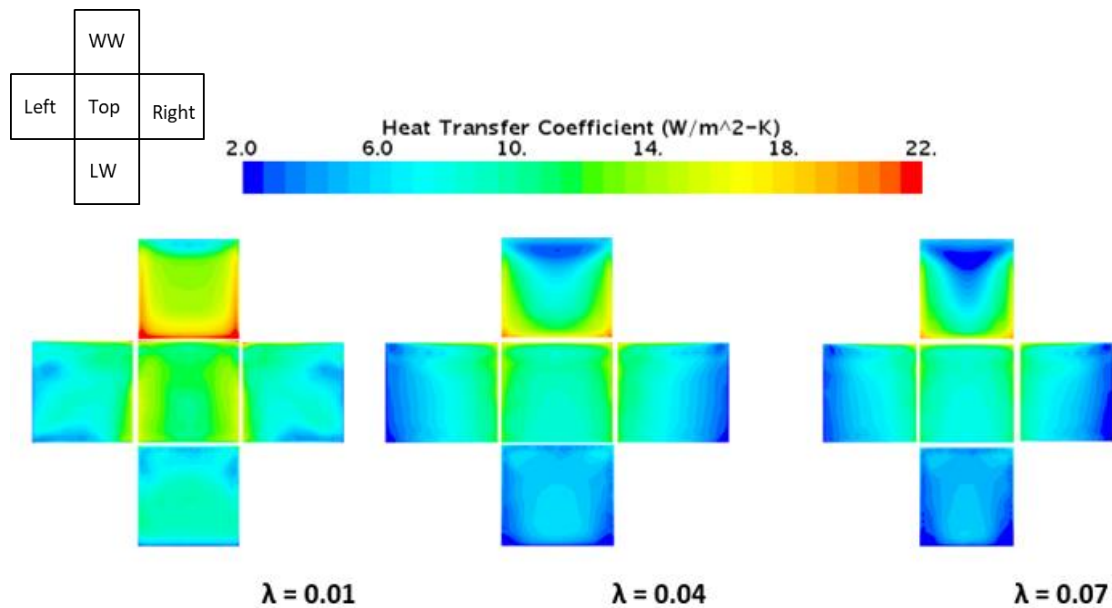


Figure 3.18 Contour plots of CHTC on surfaces of the cube at selected densities

Figure 3.19 indicates the curve fits on the simulated CHTC data in the isolated flow regime. Even though the specific trend of CHTC on each cube surface is different, a quadratic fit for each curve provides a reasonable match. Accordingly, the equation of the curves for each surface is shown in Table 3.4.

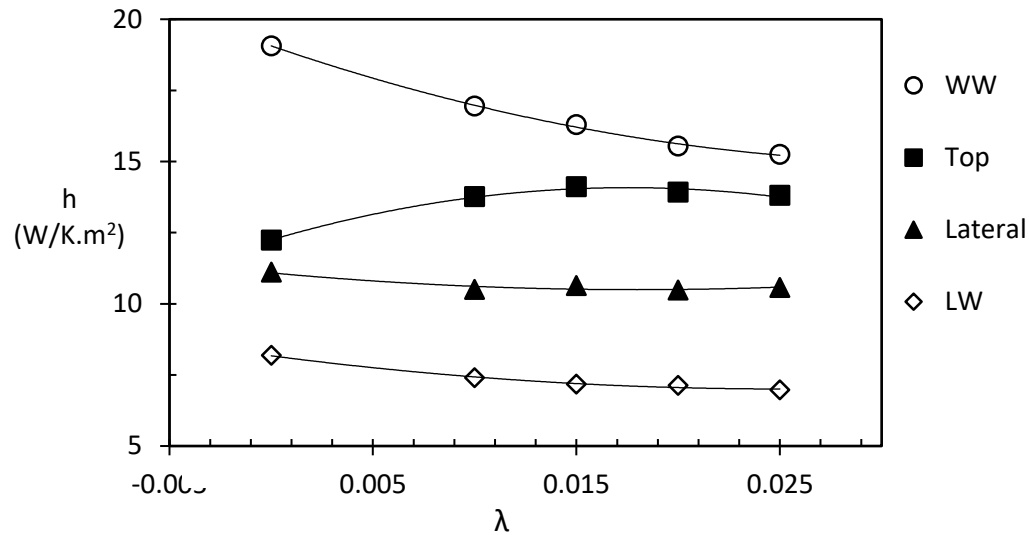


Figure 3.19 Heat transfer coefficient versus wind speed in the isolated flow regime

Table 3.4 The equations required to fit the data in Figure 3.19.

| Surface | Equation | Coefficient of determination (R^2) |
|-----------------|--|--|
| Windward | $h = 3667.4*\lambda^2 - 245.48*\lambda + 19.06$ | 0.9985 |
| Top | $h = -5973.7*\lambda^2 + 209.47*\lambda + 12.24$ | 0.9896 |
| Lateral | $h = 1820.6*\lambda^2 - 65.54*\lambda + 11.08$ | 0.892 |
| Leeward | $h = 1837*\lambda^2 - 92.56*\lambda + 8.17$ | 0.991 |

Figure 3.20 shows linear fit curves for the remaining (data in the interference and skimming flow regime) portion of the CHTC data. The equations for these curves are shown in Table 3.5.

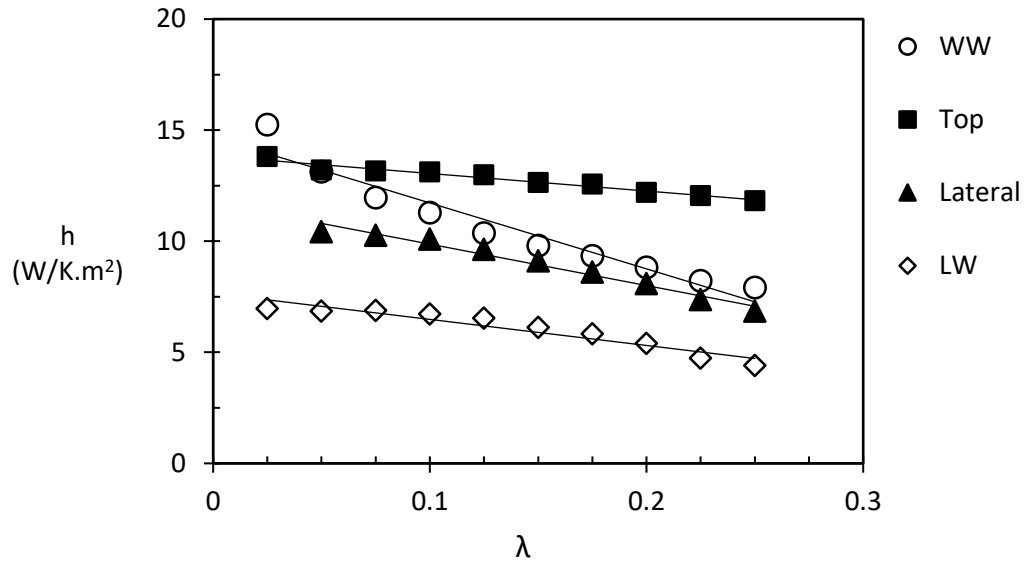


Figure 3.20 Heat transfer coefficient versus wind speed in the interference and skimming flow regimes

Table 3.5 The equations required to fit the data in Figure 3.20.

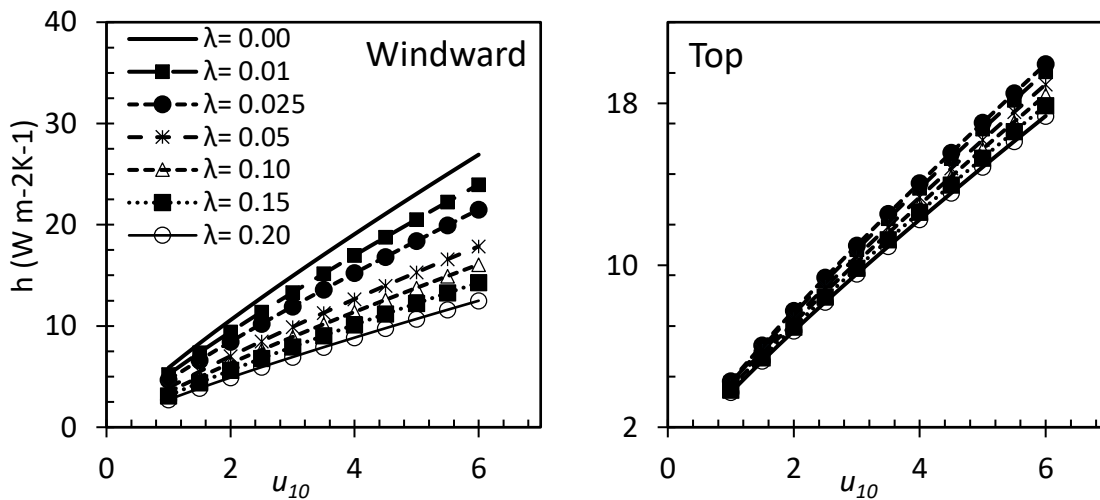
| Surface | Equation | Coefficient of determination (R^2) |
|-----------------|------------------------------|--|
| Windward | $h = -25.36*\lambda + 13.9$ | 0.9756 |
| Top | $h = -7.36*\lambda + 13.74$ | 0.9559 |
| Lateral | $h = -18.64*\lambda + 11.73$ | 0.9716 |
| Leeward | $h = -13.04*\lambda + 7.89$ | 0.9366 |

Overall, the results discussed can be summarized in a single table of correlations. Considering the exponent m obtained from the isolated cube experiment (Figure 3.15, Table 3.3), the equations can be re arranged as in Table 3.6.

Table 3.6 Summary of proposed correlations

| Surface | Isolated roughness flow regime | Interference and skimming flow regime |
|-----------------|--|---|
| Windward | $h = 5.87u_{10}^{0.85}(192.4\lambda^2 - 12.88\lambda + 1)$ | $h = 5.87u_{10}^{0.85}(0.73 - 1.33\lambda)$ |
| Top | $h = 3.72u_{10}^{0.86}(-488\lambda^2 + 17.11\lambda + 1)$ | $h = 3.72u_{10}^{0.86}(1.12 - 0.6\lambda)$ |
| Lateral | $h = 3.32u_{10}^{0.87}(164.3\lambda^2 - 5.92\lambda + 1)$ | $h = 3.32u_{10}^{0.87}(1.06 - 1.68\lambda)$ |
| Leeward | $h = 2.51u_{10}^{0.85}(224.8\lambda^2 - 11.33\lambda + 1)$ | $h = 2.51u_{10}^{0.85}(0.97 - 1.6\lambda)$ |

CHTC plot based on the proposed correlations are shown in Figure 3.21.



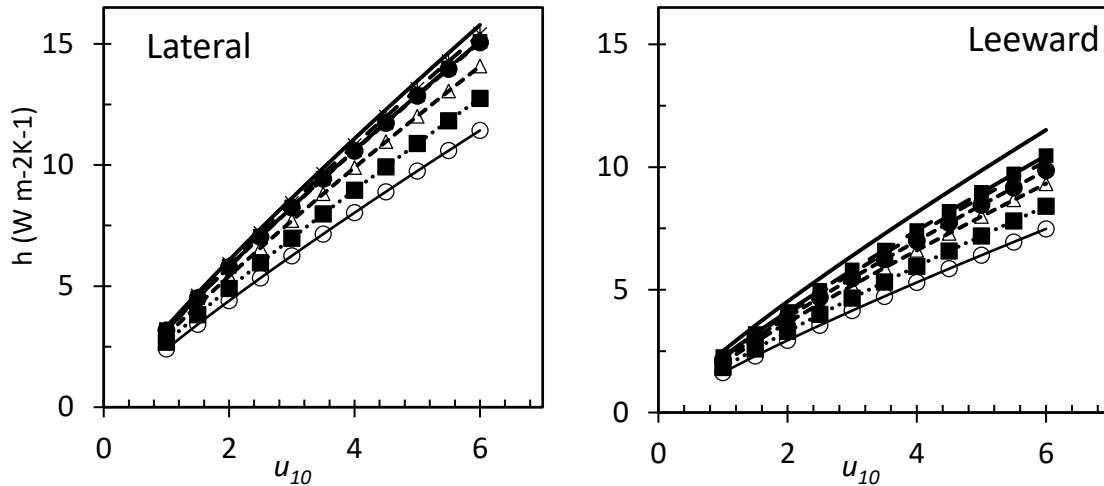
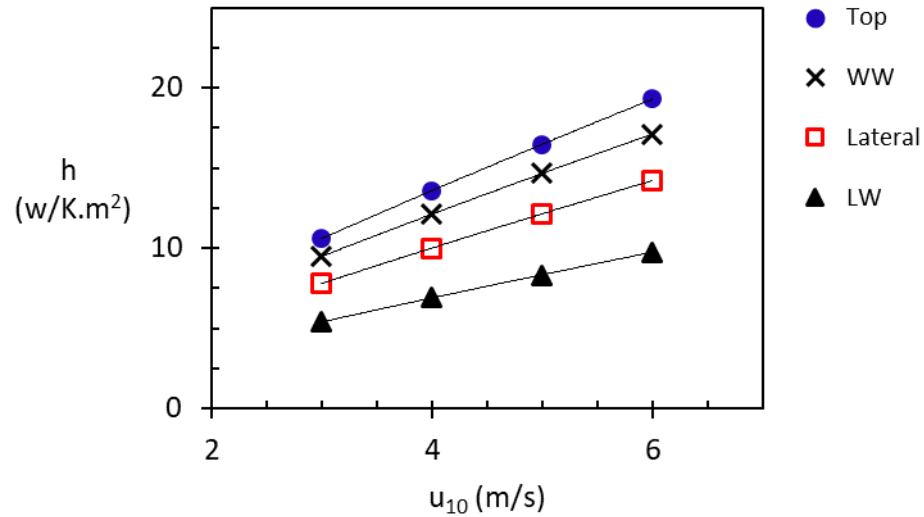


Figure 3.21 CHTC plots based on the proposed correlation in Table 3.6 (all orientations)

3.4.3 Test case for building packing density $\lambda = 0.075$

We have tested the coefficients C and exponent m of the correlation for a density of $\lambda = 0.075$. A comparison of the values of C and m obtained from the proposed correlation (Table 3.6) and the new set of simulations is conducted. The results (Figure 3.22, Table 3.7) indicated that the maximum error in the coefficients (C) is 2.3%, corresponding to the lateral surfaces, and the maximum error in the exponents (m) is 0.58%, corresponding to the top surfaces. This should be anticipated, as the flow field around these surfaces (lateral and top) is affected by recirculation and is also sensitive to turbulence fluctuations.



**Figure 3.22 Power-law curve fit between CHTC and u_{10} for the test case $\lambda = 0.075$
(all surfaces)**

Table 3.7. A power-law expression for the test case at $\lambda = 0.075$

| Surface | Equation | Coefficient of determination (R^2) |
|-----------------|-----------------------------|--|
| Windward | $h = 3.71 * u_{10}^{0.853}$ | 1 |
| Top | $h = 4.08 * u_{10}^{0.865}$ | 0.9999 |
| Lateral | $h = 3.02 * u_{10}^{0.867}$ | 1 |
| Leeward | $h = 2.11 * u_{10}^{0.854}$ | 1 |

3.5 Conclusion

The presence of buildings around another building alters the local microclimate from what it would have been if a building was to be located in an open surrounding. The nature of aggregation or rarefaction of these buildings is parameterized by the packing density. Consequently, the need for accounting the impact of surrounding buildings on the

evaluation of the convective heat transfer coefficient is argued. CFD's capability to enable full-scale simulations in several cases, with better variable control is utilized.

Several packing density cases were chosen to encompass the three flow regimes, namely: isolated flow ($\lambda < 0.027$), interference flow ($0.027 < \lambda < 0.155$), and skimming flow options ($\lambda > 0.155$). The simulation process is validated against previous experimental and numerical work. In general, the RSM turbulence model used in the present simulation performed well in relation to the k-epsilon turbulence model, in approaching the experimental records.

The results of the present work revealed the external CHTC behaves differently in the three regimes, and on the building surfaces. There is a sharp change in CHTC for sparse canopy cases. The trend, in general, indicates an increase of CHTC with density for the top surface, a decrease of CHTC for all other surfaces with an increase in density. For denser canopies, the CHTC decreases gently as density increases for all surfaces. For the highest density considered, the values of CHTC reduce by over 55%, 30%, and 40% from their corresponding benchmark values in the case of isolated building studies for Windward, Lateral and Leeward surfaces respectively. The top surface, however, has its peak CHTC in the middle of the isolated flow regime. The peak top surface CHTC value is 17% higher than the CHTC at the benchmark case or the value at the highest density (which are found very close). Lastly, a correlation of CHTC comprising both wind speed and urban packing density is presented.

This research does only address the impact of a uniform urban form on CHTC, and it does not address the outstanding and more realistic, issues like the introduction of heterogeneity to this model.

References

- Abdi, D. and Bitsuamlak, G.T. (2016). Wind flow simulations in idealized and real built environments with models of various levels of complexity, *Wind & Structures*, 22 (4): 503-524.
- Abdi, D. and Bitsuamlak, G.T. (2014). Numerical evaluation of the effect of multiple roughness changes. *Wind and Structures*, 19(6): 585-601.
- Adamek, K., Vasani, N., Elshaer, A., English, E., and Bitsuamlak, G.T. (2017). Pedestrian level wind assessment through city development: A study of the financial district in Toronto, *Sustainable Cities and Societies*, 35:178-190.
- Allegrini, J., Dorer, V. Carmeliet, J. (2012). Analysis of convective heat transfer at building façades in street canyons and its influence on the predictions of space cooling demand in buildings, *J. Wind Eng. Ind. Aerod.* 104:464-473.
- ASHRAE. 2009. 2009 ASHRAE Handbook – Fundamentals, Chapter 16, Air Flow Around Buildings, Atlanta: American Society of Heating, Refrigerating, and Air-Conditioning Engineers, Inc.
- Awol, D.A., Bitsuamlak, G.T., Tariku, F. (2017). Consistent analytical urban canopy layer velocity profile for dense building arrangement. *Americas Conference on Wind Engineering*, Gainesville, United States, 21-24 May 2017

Blocken, B., Defraeye, T., Derome, D., Carmeliet, J. (2009). High-resolution CFD simulations for forced convective heat transfer coefficients at the facade of a low rise building, *Build. Environ.* 44:2396-2412.

Blocken, B., Stathopoulos, T., Carmeliet, J., Hensen, J.L.M. (2011). Application of computational fluid dynamics in building performance simulation for the outdoor environment: an overview, *Journal of Building Performance Simulation* 4:157-184.

Bordass B., Leaman, A., Ruyssevelt, P. (2001). Assessing building performance in use 5: conclusions and implications, *Building Research & Information*, 29:144 -157.

Bordass B., Leaman, A. (2013). A new professionalism: remedy or fantasy?, *Building Research & Information*, 41:1, 1-7.

Burman, E., Rigamonti, D., Kimpian, J., Mumovic D. (2012). Performance gap and thermal modeling: a comparison of simulation results and actual energy performance for an academy in northwest England, *First Building Simulation and Optimization Conference*, Loughborough, UK, 10-11 September 2012.

Castro, I.P. (2017) Are Urban-Canopy Velocity Profiles Exponential? *Boundary-Layer Meteorol* 164(3):337–351. DOI 10.1007/s10546-017-0258-x

Chen J., Augenbroe G., Wang Q., Song X. (2017) Uncertainty analysis of thermal comfort in a prototypical naturally ventilated office building and its implications compared to deterministic simulation, *Energy and Buildings*, 146:283-294

Cheng, H., Castro, I.P. (2002). Near-wall flow over urban-like roughness. *Boundary-Layer Meteorol* 104(2): 229–259

Chyu, M.K., Natarajan, V. (1991). Local heat/mass transfer distributions on the surface of a wall-mounted cube, *Trans. ASME J. Heat. Transf.* 113:851-857.

Cionco, R.M. (1965). Mathematical Model for Air Flow in a Vegetative Canopy. *J. Applied Meteorol.* 4:517–522

Coceal, O., Belcher S.E. (2004). A canopy model of mean winds through urban areas. *Q J Roy Meteorol Soc* 130(599):1349–1372

Coceal, O., Thomas, T.G., Castro, I.P., Belcher, S.E. (2006). Mean flow and turbulence statistics over groups of urban-like cubical obstacles. *Boundary-Layer Meteorol* 121:491-519

Cowan, I.R. (1968). Mass, heat and momentum exchange between stands of plants and their atmospheric environment. *Q J Roy Meteorol Soc* 94:523–544

Davenport, A. G. (1960). Rationale for determining design wind velocities, *ASCE Journal of the Structural Division*, 86(5):39 – 68

Defraeye, T., Blocken, B., Carmeliet, J. (2011). Convective heat transfer coefficients for exterior building surfaces: Existing correlations and CFD modelling, *Energy Conversion and Management* 52:512–522

Defraeye, T., Blocken, B., Carmeliet, J. (2010). CFD analysis of convective heat transfer at the surfaces of a cube immersed in a turbulent boundary layer, *Int. J. Heat. Mass Transf.* 53:297-308.

van Dronkelaar, C., Dowson, M., Burman, E., Spataru C., Mumovic, D. (2016). A review of the energy performance gap and its underlying causes in non-domestic buildings, *Frontiers in mechanical engineering: review*, 1:17.

Emmel, M.G., Abadie, M.O., Mendes, N. (2007). New external convective heat transfer coefficient correlations for isolated low-rise buildings, *Energ Build.* 39:335-342.

Evangelisti, L., Guattari, C., Gori, P., Bianchi, F. (2017). Heat transfer study of external convective and radiative coefficients for building applications, *Energ Build.* 151:429–438

Franke, J., Hellsten, A., Schlünzen, H., Carissimo, B. (2011). The COST 732 Best Practice Guideline for CFD simulation of flows in the urban environment: a summary, *Int. J. Environ. Pollut.* 44 (2011) 419-427.

Franke, J., Hellsten, A., Schlünzen, H., Carissimo B. (Eds.) (2007). Best practice guideline for the CFD simulation of flows in the urban environment, COST Office, Brussels, 3-00-018312-4.

Hagishima, A., Tanimoto, J. (2003). Field measurements for estimating the convective heat transfer coefficient at building surfaces, *Build. Environ.* 38:873-881.

van Hooff, T., Blocken, B. (2010). On the effect of wind direction and urban surroundings on natural ventilation of a large semi-enclosed stadium, *Computers & Fluids* 39:1146-1155.

Ito, N., Kimura, K., Oka, J. (1972). Field experiment study on the convective heat transfer coefficient on exterior surface of a building, *ASHRAE Trans.* 78:184-192.

Jürges, W. (1924). The heat transfer at a flat wall (Der Wärmeübergang an einer ebenen Wand), Beihefte zum Gesundh.-Ing. 1:19.

Kader, B.A. (1981) Temperature and Concentration Profiles in Fully Turbulent Boundary Layers, *Int. J. Heat Mass Transfer*, 24:1541-1544.

Kahsay, M.T., Bitsuamlak, G., Tariku, F. (2018) Numerical analysis of convective heat transfer coefficient for building facades, *Journal of Building Physics* 1–23

Karava, P., Jubayer, C.M., Savory, E. (2011). Numerical modelling of forced convective heat transfer from the inclined windward roof of an isolated low-rise building with application to photovoltaic/thermal systems, *Appl. Therm. Eng.* 31:1950-1963.

Launder, B., Reece, G. J., Rodi, W. (1975). Progress in the Development of a Reynolds Stress Turbulence Closure, *J Fluid Mech.* 68(3):537 – 566

Leschziner, M.A. (1990). Modelling engineering flows with Reynolds stress turbulence closure, *J. Wind Eng. Ind. Aerodyn.* 35:21-47.

Liu, J., Heidarinejad, M., Gracik, S. Srebric, J. (2015). The impact of exterior surface convective heat transfer coefficients on the building energy consumption in urban neighborhoods with different plan area densities, *Energy Build.* 86:449-463.

Liu, J. Srebric, J. Yu, N. (2013). Numerical simulation of convective heat transfer coefficients at the external surfaces of building arrays immersed in a turbulent boundary layer, *Int. J. Heat. Mass Transf.* 61:209-225.

Liu, Y., Harris, D.J. (2007). Full-scale measurements of convective coefficient on external surface of a low-rise building in sheltered conditions, *Build. Environ.* 42:2718-2736.

Loveday, D.L., Taki, A.H. (1996). Convective heat transfer coefficients at a plane surface on a full-scale building facade, *Int. J. Heat. Mass Transf.* 39:1729-1742.

Macdonald, R.W. (2000). Modelling the mean velocity profile in the urban canopy layer. *Boundary Layer Meteorol* 97(1):25–45

Meinders, E.R., Hanjalic, K., Martinuzzi, R.J. (1999). Experimental study of the local convection heat transfer from a wall-mounted cube in turbulent channel flow, *Trans. ASME J. Heat. Transf.* 121:564-573.

Meinders, E.R. (1998). Experimental Study of Heat Transfer in Turbulent Flows over Wall Mounted Cubes, PhD thesis, Technische Universiteit Delft.

Menezes, A.C., Cripps, A., Bouchlaghem, D., Buswell, R. (2012). Predicted vs. Actual Energy Performance of Non-Domestic Buildings, Third International Conference on Applied Energy, 16-18 May 2011 - Perugia, Italy.

Mirsadeghi, M., Costola, D., Blocken, B., Hensen, J.L.M. (2013). Review of external convective heat transfer coefficient models in building energy simulation programs: implementation and uncertainty, *Appl. Therm. Eng.* 56:134-151.

Montazeri, H. Blocken, B. (2017). New generalized expressions for forced convective heat transfer coefficients at building facades and roofs, *Build Environ.* 119:153-168

Montazeri, H., Blocken, B., Derome, D., Carmeliet, J., Hensen, J.L.M. (2015). CFD analysis of forced convective heat transfer coefficients at windward building facades: influence of building geometry, *J. Wind Eng. Ind. Aerodyn.* 146:102-116.

Moonen, P., Defraeye, T., Dorer, V., Blocken, B., Carmeliet, J. (2012). Urban physics: effect of the microclimate on comfort, health and energy demand, *Frontiers of Architectural Research* 1:197-228.

Murthy, B.N., Joshi, J.B. (2008). Assessment of standard k–e, RSM and LES turbulence models in a baffled stirred vessel agitated by various impeller designs, *Chem Eng Sci.* 63: 5468 – 5495

Nakamura, H., Igarashi, T., Tsutsui, T. (2001). Local heat transfer around a wall-mounted cube in the turbulent boundary layer, *Int. J. Heat. Mass Transf.* 44:3385-3395.

Natarajan, V., Chyu, M.K. (1994). Effect of flow angle-of-attack on the local heat/mass transfer from a wall-mounted cube, *Trans. ASME J. Heat. Transf.* 116:552-560.

Oke, T.R. (1988). Street design and urban canopy layer climate. *Energ Build* 11(1-3)103-113

Palyvos, J.A. (2008). A survey of wind convection coefficient correlations for building envelope energy systems' modeling, *Appl. Therm. Eng.* 28:801-808.

Rodi, W. (1997). Comparison of LES and RANS calculations of the flow around bluff bodies, *J. Wind Eng. Ind. Aerodyn.* 69:55-75.

Sharples, S. (1984). Full-scale measurements of convective energy losses from exterior building surfaces, *Build. Environ.* 19:31-39.

Sparrow, E.M., Ramsey, J.W., Mass, E.A. (1979). Effect of finite width on heat transfer and fluid flow about an inclined rectangular plate, *J. Heat. Transf.* 101:199-204.

- Stathopoulos, T., Wu, H. (1995). Generic models for pedestrian-level winds in built-up regions, *J. Wind Eng. Ind. Aerodyn.* 54-55:515-525.
- Speziale, C.G. (1991). Analytical Methods for the Development of Reynolds-Stress Closures in Turbulence, *Annu Rev Fluid Mech.*, 23:107-157
- Speziale, C.G. (1995). A review of Reynolds stress models for turbulent shear flows, NASA Langley Research Center, NASA Contractor Report 195054, ICASE Report No. 95-15
- Tominaga, Y., Mochida, A., Yoshie, R., Kataoka, H., Nozu, T., Yoshikawa, M., Shirasawa, T. (2008). AIJ guidelines for practical applications of CFD to pedestrian wind environment around buildings, *J. Wind Eng. Ind. Aerodyn.* 96:1749-1761.
- Turner, C., Frankel, M. (2008). Energy performance of LEED for new construction buildings (Final Report), New Buildings Institute, White Salmon (WA)
- Vereecken, E., Janssen, H., Roels, S. (2018). A determination methodology for the spatial profile of the convective heat transfer coefficient on building components, *Indoor Built Environ.*, 27(4):512–527
- Wang W. (2014). Analytically modelling mean wind and stress profiles in canopies. *Boundary-Layer Meteorol* 151(2)239–256
- Wieringa, J. (1992). Updating the Davenport roughness classification, *J. Wind Eng. Ind. Aerodyn.* 41:357-368.

Yang, X.I.A., Sadique, J., Mittal, R., Meneveau, C. (2016). Exponential roughness layer and analytical model for turbulent boundary layer flow over rectangular-prism roughness elements. *J Fluid Mech* 789:127–165

Chapter 4

4 Semi-analytical estimation of external convective heat transfer coefficient for buildings in an urban-like setting

4.1 Introduction

Research on a more reliable urban wind and heat transport models is increasing driven by sustainability interests as a result of vulnerabilities arising from climate change and the associated higher energy demands (Grimmond et al. 2010). A World Bank report shows 70% of the greenhouse gas emission is generated in cities (UN-Habitat 2011). Population growth in cities requires efficient use of space, as cities become denser through time. Adamek et al. (2017), for example, have shown the temporal changes in the density of buildings in the city of Toronto over the past decades, and how variations to the urban morphology affected the urban micro-climate. Micro-climatic variations imply changes to the urban wind flow, heat transport, and pollutant/mass movement. The circumstances are expected to amplify in upcoming decades as forecasts indicate more than 66% of the world population starts to live in urban places by 2050 (UN - DESA 2018). Implications of this could be a severe rise in energy demand and pollution removal needs.

The effect of the urban morphology on the ensuing microclimatic change in urban canopies has been studied with focus on pollutant dispersion (Di Sabatino et al. 2007, Hang et al. 2012, Yuan et al. 2014), pedestrian comfort (Blocken et al. 2012, Arkon et al. 2013, Tsang

et al. 2012, Adamek et al. 2017, Du et al. 2018), indoor wind environment (You et al. 2017) and wind loading (Elshaer et al. 2017). However, there is very limited investigation focusing on the impact of changes in urban morphology on convective heat transfer from buildings. The two exceptions in surveyed literature thus far, to account for urban morphology in the determination of CHTC, are by Lui et al. (2013) and Awol et al. (2019).

On a pioneer work by Oke (1988), the air flow around a pack of idealized buildings is studied. Oke (1988) identified three distinct regimes of flow, having different flow structures based on proximity between the various obstacles. The first is called isolated roughness regime, where the spacing between buildings can be very large compared to the height, in which case the wake from one of the obstacles hardly influences the flow around an obstacle downstream. In this case, the flow field resembles that of around a purely isolated obstacle. The second flow regime is called wake interference. In this case, there is significant interaction between the wake of an upstream obstacle on an obstacle downstream; and this condition is distinguished by pronounced mass exchange (besides momentum / turbulent shear) between the flow under the canopy and the one over it. In the third regime called skimming flow, the flow above the canopy skims over the obstacles and there exists a counter-current vortex trapped in the spaces between the obstacles. Exchanges in momentum due to turbulent shear at the top of the canopy are believed to drive the counter-flow under the canopy. See Table 1.1 for a summary of the flow regimes at different canopy density with schematic descriptions.

Packing density has been used as an expression of aggregation of an urban built system. There are two ways in which packing density has been defined, namely the frontal and planar forms of aggregation.

The presence of bluff bodies in urban environments is commonly simulated in research by idealized roughness elements, an array of an inline or staggered arrangement of small-scale objects (usually considered as cubes) mounted on a wall. Here the cube heights are meant to represent the average height of the roughness. Most of these investigations are laboratory experiments (Yang et al. 2016, Macdonald 2000, Cheng et al. 2002,) and some CFD simulations (Castro 2017, Yang et al. 2016, Abdi and Bitsuamlak 2016, 2014, Coceal et al. 2006).

In general for canopies, the frontal packing density (λ_f), planar packing density (λ_p) are expressed as;

$$\lambda_f = \frac{A_f}{A_d}, \lambda_p = \frac{A_p}{A_d} \quad \text{Eq.4.1}$$

where A_f is the frontal area, A_p is the planar, and A_d is the unit underlying lot area on the ground surface (Figure 4.1).

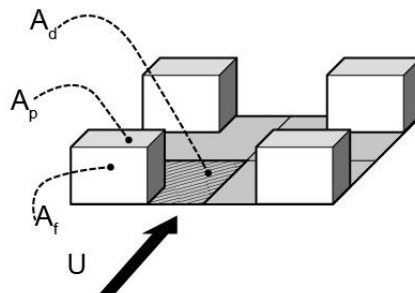


Figure 4.1 Description of areas used to determine a density parameter

The frontal area, A_f , represents the area of obstruction exhibited by the flow due to obstructing elements. Other packing density considerations may employ the planar area

density, A_p ; representing the average area of horizontal planar projection cast by the obstacles. In most urban canopy flow simulations, buildings are represented by arrays of cubes, implying equal frontal and planar area indices ($A_f = A_p$). For which,

$$\lambda_f = \frac{H^2}{(S + H)^2} = \frac{1}{\left(1 + \frac{S}{H}\right)^2} = \lambda_p \quad \text{Eq.4.2}$$

where H is the cube height, and S is the spacing between adjacent cubes.

External convective heat transfer coefficient of buildings has been estimated from several correlations obtained from experimental and numerical simulations (Kahsay et al. 2018, Montazeri et al. 2015, Blocken et al. 2009, Emmel et al. 2007, Nakamura et al. 2001, Natarajan et al. 1994; Meinders et al. 1999, Jurges 1924; Sparrow et al. 1979). An extensive review of CHTC correlations has been provided in Mirsadeghi et al. 2013, Defraeye et al. 2011, and Palyvos 2008. However, reported correlations are found to have significant scatter (Evangelisti et al. 2017, Mirsadeghi et al. 2013, Defraeye et al. 2011, Emmel et al. 2007), mainly due to the specific conditions under which each study is conducted. It is noted that the largest CHTC estimate, from one correlation, could be 5 to 10 times the smallest, from other correlation at the same conditions (Chen et al. 2017). This variation further widens for higher wind speeds.

Most convective heat transfer evaluation correlations outlined in literature are obtained from studies on isolated buildings with open terrain exposure condition and with the absence of other surrounding buildings. However, the changes in urban microclimate can be due to terrain difference, surrounding built form and arrangement (Moonen et al. 2012, Blocken et al. 2011, Franke et al. 2007, Coceal et al. 2004, Macdonald 2000, Stathopoulos

et al. 1995, Oke 1988). Adamek et al. (2017) have shown how a city development can bring about changes in urban form; and consequently, change in the microclimate near buildings.

The CHTC and microclimatic properties in the urban canopy remains to be the two main sources of uncertainty in attaining robust building energy performance (Chen 2017). For instance, u_{10} is directly evaluated using a modified log-law wind profile with adjusted aerodynamic roughness for the typical exposure. However, several researchers have indicated that the velocity profile in urban and plant canopies is never logarithmic and is considerably reduced from the log-law predictions (Castro 2017, Coceal et al. 2004, Macdonald 2000, Oke 1988, Awol et al. 2017, Wang 2014, Coceal et al. 2004, Cheng et al. 2002, Macdonald 2000, Cowan 1968, Cionco 1965). This reduction in flow speed, in turn, influences the values of CHTC computed (Awol et al. 2019).

In this paper, we propose a semi-analytical heat transfer coefficient formulation based on reference velocity derived from the local roughness sub layer (RSL) physics. Awol et al. 2017 derived a one-dimensional turbulence closure canopy flow model, which has been used to obtain turbulence and drag parameters under RSL flow condition. We use the findings from Awol et al. 2017 to find a new heat transfer coefficient model for windward and top surfaces of the building. The new model addresses the urban microclimatic parameters such as morphology, aerodynamic exposure, and reference velocity scale issues. The validity of the heat transfer coefficient correlation obtained is verified by the data obtained from a CFD simulation by Awol et al. (2019).

The main reasons why the study focuses on the windward wall and the roof semi-analytical CHTC derivation are as follows. The windward surface (i) sees the most statistically-stationary wind flow (compared to the other surfaces), hence allows more consistent

discussion and correlations (Kahsay et al. 2019, Montazeri et al. 2015, Nicceno et al. 2002), (ii) usually exhibits the highest value of CHTC (Meinders 1998), and (iii) often used as the sole building convective heat estimation basis, along with leeward values, in BE and HAM tools (Mirsadeghi et al. 2013). The top surface (i) often exhibits the highest or second highest CHTC measure (Wang et al. 2006, Nakamura et al. 2001, Meinders 1998, Chyu et al. 1991) and (ii) is less discussed in CHTC correlation provisions (Mirsadeghi et al., 2013). Moreover, the two surfaces are the most wetted by wind-driven rain, and the coefficients CHTC and CMTC (convective moisture transfer coefficients) are very important (Montazeri et al. 2015, Janssen et al. 2007, Blocken et al. 2004, Künzeli et al. 1996).

4.2 Semi-analytical CHTC model derivation

A convective heat transfer coefficient model will be derived based on mean and turbulent velocity for a representative canopy level. The characteristic location for the vertical windward surface is considered as the location of the average mean velocity between the ground and the canopy top. For the top surface, however, the location of the canopy top itself is adopted as representative of the characteristic location of the flow. The analytical mean wind velocity profile derived by Awol et al. (2017), and a CFD simulation data for CHTC reported in Awol et al. (2019) will be used.

In Awol et al. (2017), space averaged analytical mean stream-wise velocity profile was developed from one-dimensional turbulence closure and linearized drag parametrization that is applied to steady Navier-Stokes equation. In RSL flows, transport phenomenon under the canopy is as a result of momentum exchange in the turbulent shear layer at the

top of the canopy. For an idealized pack of buildings with a given density, the mean velocity profile (u) is given by Eq.4.3.

$$\frac{u}{u_H} = (\alpha/8)\zeta^2 + (1 - \alpha/8) \frac{\ln(\zeta/\zeta_0)}{\ln(1/\zeta_0)} \quad \text{Eq.4.3}$$

where u_H is the velocity at mean roughness (building) height, H ; ζ is the vertical distance from the ground normalized by H ; ζ_0 is the aerodynamic roughness height of the approaching flow normalized by H ; α , the attenuation/linearization coefficient and is related to the physical frontal area index/density, λ_f , of pack of buildings. The relationship between α and λ_f has been obtained by curve fitting several experimentally measured values of the shear length scale, as shown in Eq.4.4 (Awol et al. 2017).

$$\alpha = \frac{8}{(2-b)} \left[\exp\left(-0.097 \ln^2(\lambda_f) + 0.41 \ln(\lambda_f) + 0.87\right) \right] \quad \text{Eq.4.4}$$

where the shear length scale, L_s , is obtained from Eq.4.5.

$$\frac{L_s}{H} = \frac{u_H}{\partial u / \partial \zeta|_{z=1}} = \frac{1}{\alpha/4 + (1 - \alpha/8)b'} \quad \text{Eq.4.5}$$

and, $b = 1/\ln(1/\zeta_0)$.

It is to be noted that the boundary layer portion above the canopy is inertial, and hence is represented by the modified log profile, commonly referred to as displaced log-law velocity profile, given by Eq.4.6;

$$\frac{u}{u_{ref}} = \frac{\ln(\zeta - D/\zeta_0)}{\ln(\zeta_{ref} - D/\zeta_0)} \quad \text{Eq.4.6}$$

where, u_{ref} is the reference velocity measured at ζ_{ref} , the reference height; u_{ref} is related to the meteorological data, measured at 10 m height from the ground. D is the displacement height; and, z_m is where the mean height at which the total surface drag force acts.

4.2.1 Derivation for Convective heat transfer coefficient

The heat transfer coefficient in similarity or integral solution methods, for flow over a horizontal flat plate, has been related to the mean velocity measurement. This has also been empirically proven by several studies on isolated bluff bodies (Wang et al. 2006, Nakamura et al. 2001, Meinders et al. 1999, Loveday et al. 1996, Quintela et al. 1995, Natarajan et al. 1994, Chyu et al. 1991, Ito et al. 1972, Sturrock 1971). The general form of this relationship is,

$$Nu \propto Re^m, \text{ or } h \propto u^m \quad \text{Eq.4.7}$$

where Nu is the Nusselt number, Re is the Reynolds number, h is the convective heat transfer coefficient, and m is a constant coefficient (usually a coefficient of the orientation of the surface). In this derivation, the physics near the windward surface is assumed to be represented by an equivalent horizontal surface situated at the location of the average mean velocity in the canopy.

The heat transfer coefficient can also be expressed in terms of the temperature gradient near the surface. i.e.

$$Nu|_{local} = \frac{hH}{K}|_{local} = -\frac{\partial\theta/\partial z|_s}{\theta_{ref} - \theta_s} H|_{local} \quad \text{Eq.4.8}$$

where K is thermal conductivity of air, θ is temperature, θ_{ref} is the reference temperature measured at the location of reference, the subscript s is for values at the surface of the bluff body, z distance from the surface.

According to Panofsky et al. (1984), Cenedese et al. (1997), and Lo (1995), the gradients of velocity (u) and that of temperature (θ) in atmospheric flow over the ground surface can be related.

$$\frac{\partial\theta/\partial z|_s}{\theta_{ref} - \theta_s} = f(u_*, \theta_*, Pr_t) \left(\frac{1}{u_{ref}} \right) \frac{\partial u}{\partial z}|_s \quad \text{Eq.4.9}$$

where u_* is the friction velocity, θ_* is the dynamical temperature scale (i.e., the temperature variance normalized by the friction velocity), and Pr_t is the turbulent Prandtl number of the flow. Thus,

$$Nu|_{local} = \frac{hH}{K}|_{local} \propto \left(\frac{1}{u_{ref}} \right) \frac{\partial u}{\partial z}|_s f(u_*, \theta_*, Pr_t) \quad \text{Eq.4.10}$$

However, more specific relationships are provided by Simonich et al. (1978) and Karava et al. (2011) in their studies of the effect of turbulence changes on convective heat transfer. The expressions suggested have the form;

$$Nu \propto AI_u + 1 \quad \text{Eq.4.11}$$

where I_u is the turbulent intensity, and A is a constant. The value of A suggested by Karava et al. (2011), for an inclined windward roof surface, is 2.8. Since $I_u = u'/u$, and the

turbulence fluctuation, u' , can be approximated, from mixing length theory, in terms of the mean velocity gradient. The characteristic velocity of turbulence can be written as: $u' = l_m du/dz$; in which, it is assumed that the velocity for the energy-carrying eddies is in the same order as the velocity gradient for the mean flow. The mixing length, l_m , can be approximated with κz . where κ is the von Karman constant and z is the distance from the surface as defined earlier. Thus, Nu becomes as shown in Eq.4.12.

$$Nu \propto (A\kappa z/u_H)\partial u/\partial z + 1 \quad \text{Eq.4.12}$$

where A is a constant coefficient, κ von Karman constant.

The upstream atmospheric boundary layer (ABL) flow undergoes significant alteration in canopies, such that the mean velocity (and the Reynolds number) and the turbulence intensity change significantly (often in orders of magnitude), from conditions at upstream (Awol et al. 2017, Wang 2014, Coceal et al. 2004, Cheng et al. 2002, Macdonald 2000, Cowan 1968, Cionco 1965). Therefore, estimations based on mesoscale measurements may not be adequate to address changes of scale in the local microclimate.

The local heat transfer coefficient can be expressed by combining Eq.4.7 and Eq.4.12; accounting for the mean and turbulence velocity changes in canopies;

$$Nu|_{local} = \frac{hH}{K}|_{local} \propto \left[Re^m \left(\frac{A\kappa z}{u_{ref}} \frac{\partial u}{\partial z}|_s + 1 \right) \right]_{local} \quad \text{Eq.4.13}$$

where the subscript *local* refers to the values of the terms at a specific location in the canopy (also, Re is based on u_{local} and z_{local}). However, CHTC is commonly expressed in surface average measures. The average heat transfer coefficient is assumed to have a similar form as the local heat transfer coefficient, same as in conventional flat plate convection

discussions (Bejan 2004). Also, assuming the characteristic local flow condition to be associated with the average flow velocity and gradient in the canopy layer,

$$\frac{hH}{K} \Big|_{avg} \propto Re_{avg}^m \left[\left(\frac{Akz}{u_{ref}} \right) \frac{\partial u}{\partial z} \Big|_s + 1 \right] \Big|_{avg} \quad \text{Eq.4.14}$$

where the subscript *avg* represents canopy average values of the variables (also, *Re* is based on u_{avg} and z_{avg}). To relate Eq.4.14 to parameters in the canopy flow (from Eq.4.3) and the location of measurement reference (i.e., 10 meters – approaching ABL flow parameters), the average Reynolds number is expanded. Considering the windward surface,

$$Re_{avg}^m = \left[\left(\frac{\mathbf{u}_{avg}}{\mathbf{u}_H} \right) \left(\frac{z_{avg}}{H} \right) \left(\frac{\mathbf{u}_H}{\mathbf{u}_{10}} \right) \left(\frac{H}{z_{10}} \right) \right]^m Re_{10}^m \quad \text{Eq.4.15}$$

$$\propto \left(\frac{\mathbf{u}_{avg}}{\mathbf{u}_H} \right)^m \left[\left(\frac{z_{avg}}{H} \right) \left(\frac{\mathbf{u}_H}{\mathbf{u}_{10}} \right) \left(\frac{H}{z_{10}} \right) z_{10} \right]^m u_{10}^m \quad \text{Eq.4.16}$$

Considering the top surface (i.e., horizontal roof),

$$Re_{avg}^m = Re_H^m = \left[\left(\frac{\mathbf{u}_H}{\mathbf{u}_{10}} \right) \left(\frac{H}{z_{10}} \right) \right]^m Re_{10}^m \quad \text{Eq.4.17}$$

$$\propto \left[\left(\frac{\mathbf{u}_H}{\mathbf{u}_{10}} \right) \left(\frac{H}{z_{10}} \right) z_{10} \right]^m u_{10}^m \quad \text{Eq.4.18}$$

where u_{10} is the value of the mean velocity of the undisturbed approaching flow at a location of $z_{10}=10$ meter (also, Re_{10} is based on u_{10} and z_{10}). Similarly, the gradient term in the square bracket in Eq.4.14 can be expressed as,

$$\left[\left(\frac{A\kappa z}{u_{ref}} \right) \frac{\partial u}{\partial z} \Big|_s + 1 \right] \Big|_{avg} = A\kappa \frac{H}{u_H} \frac{\partial u}{\partial z} \Big|_{avg} + 1 \quad \text{Eq.4.19}$$

Thus, using equation 2,

$$\left(\frac{u_{avg}}{u_H} \right) = \int_{z_o}^H \frac{u dz}{u_H H} = \alpha [b - 2/3]/8 + (1-b) \quad \text{Eq.4.20}$$

The turbulence intensity approximation for the windward surface is,

$$\kappa \frac{H}{u_H} \frac{\partial u}{\partial z} \Big|_{avg} \Big|_v = \kappa [\alpha(2(z_{avg}/H) - b)/8 + b/(z_{avg}/H)] \quad \text{Eq.4.21}$$

and for the horizontal roof (top) surfaces is,

$$\kappa \frac{H}{u_H} \frac{\partial u}{\partial z} \Big|_{avg} = \kappa \frac{H}{u_H} \frac{\partial u}{\partial z} \Big|_H = \kappa [\alpha(2 - b)/8 + b] \quad \text{Eq.4.22}$$

From Eq.4.3 and Eq.4.22;

$$\left(\frac{z_{avg}}{H} \right)^2 = 1/3 - (8/\alpha - 1) b (\ln(z_{avg}/H) + 1) \quad \text{Eq.4.23}$$

Equation 4.23 can be solved by iterative procedures for specific values of α . Equation 4.23 can be replaced by a simplified curve fit expression with data analysis. The upper bound

(i.e., at $\alpha = 8$) and lower bound (i.e., at $\alpha = 0$) values of z_{avg}/H become $\sqrt{1/3}$ and e^{-1} respectively. Using the reciprocal of shear length scale parameter (i.e., $\alpha(2 - b)/8 + b$), z_{avg}/H curve fits the form given in Eq.4.24.

$$z_{avg}/H = a_1 [[\alpha(2 - b)/8 + b]^{a_2}] \quad \text{Eq.4.24}$$

The resulting equation has list square coefficients of $a_1 = 0.5$ and $a_2 = 0.2$. A plot of the iterative solution and the new replacement equation are shown in Figure 4.2.

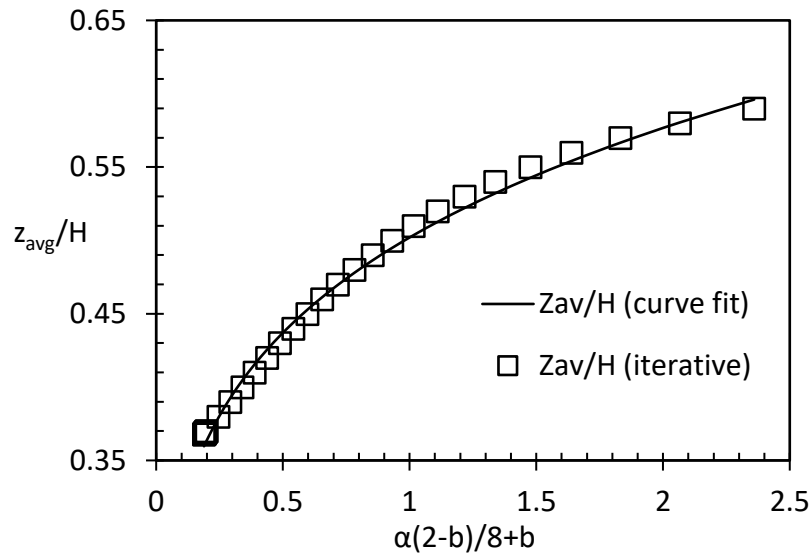


Figure 4.2 Iterative solution data and curve fit representation for z_{avg}/H Eq.4.23

The estimation of CHTC (from Eq.4.14) requires the determination of relation for u_H/u_{10} , either from experimental or CFD simulation data. Presently, the u_H/u_{10} data is extracted from the CFD results by chapter 2, and it is plotted against $\alpha(2 - b)/8 + b$ (a reciprocal of the shear length scale parameter). The best fit curve is shown in Figure 4.3, and its equation is,

$$u_H/u_{10} = -0.218 \ln[\alpha(2-b)/8 + b] \quad \text{Eq.4.25}$$

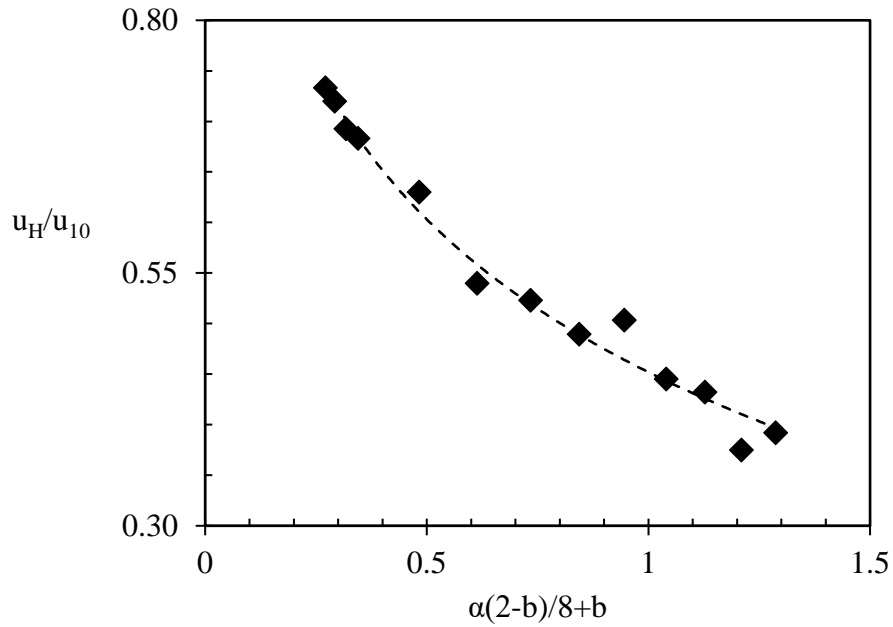


Figure 4.3 Curve fit equation for u_H/u_{10} from CFD simulation

Thus, substituting in Eq.4.14, for the windward surface,

$$h = C_s \left(\frac{u_{avg}}{u_H} \right)^m \left(\frac{z_{avg}}{H} \right)^m \left(\frac{u_H}{u_{10}} \right)^m \left(\frac{H}{z_{10}} \right)^{m-1} \left(Ak \frac{H}{u_H} \frac{\partial u}{\partial z} \Big|_{avg} + 1 \right) u_{10}^m \quad \text{Eq.4.26}$$

for top surface,

$$h = C_s \left(\frac{u_H}{u_{10}} \right)^m \left(\frac{H}{z_{10}} \right)^{m-1} \left(Ak \frac{H}{u_H} \frac{\partial u}{\partial z} \Big|_H + 1 \right) u_{10}^m \quad \text{Eq.4.27}$$

C_s , the surface related coefficient has unique values for each surface of the building. The uniqueness of these values for each surface is due to the orientation of each surface in relation to the flow, which would put them in a relatively different flow condition.

4.2.2 Determination of exponent m

Determination of m requires control of density, building height, z_{10} , and z_0 . In the case of the single isolated building (i.e., density, $\alpha \sim 0$), each bracketed term in Eq.4.27 reduces to a constant, and the equation reduces to Eq.4.28.

$$h = C_{s,i} u_{10}^m \quad \text{Eq.4.28}$$

where $C_{s,i}$ is the surface coefficient in the isolated building scenario. Eq.4.28 is the conventional CHTC model for buildings. A set of CFD simulations is conducted with atmospheric boundary layer inlet conditions. The velocities at 10 m height, from the ground, for the inlet profiles are set as 1, 2, 3, 4, and 5 m/s. The aerodynamic roughness height considered for all cases is $z_0 = 0.01$ m. the height of the building in these simulations is $H = 13.45$ m. Mean velocity and turbulence data are extracted from ESDU. The turbulence intensities and length scale tensor are extracted and are used to compute the Reynolds stress components. The RSM turbulence closure is used to solve the steady RANS system. The details of the simulation procedure are outlined in chapter 3.

The resulting CHTC value versus u_{10} data is fit to a power-law curve. The values of m for the faces of the building became 0.85 and 0.86 for windward and top surfaces, respectively. The values of $C_{s,i}$ obtained for the windward and top surfaces of the building, respectively, are 5.86 and 3.75. Monatzeri et al. (2015) conducted a simulation to find the CHTC values on windward surfaces of isolated buildings, and the values obtained here match those findings. Figure 4.4 shows the CHTC versus mean wind speed data. Table 4.1 summarizes the correlations obtained.

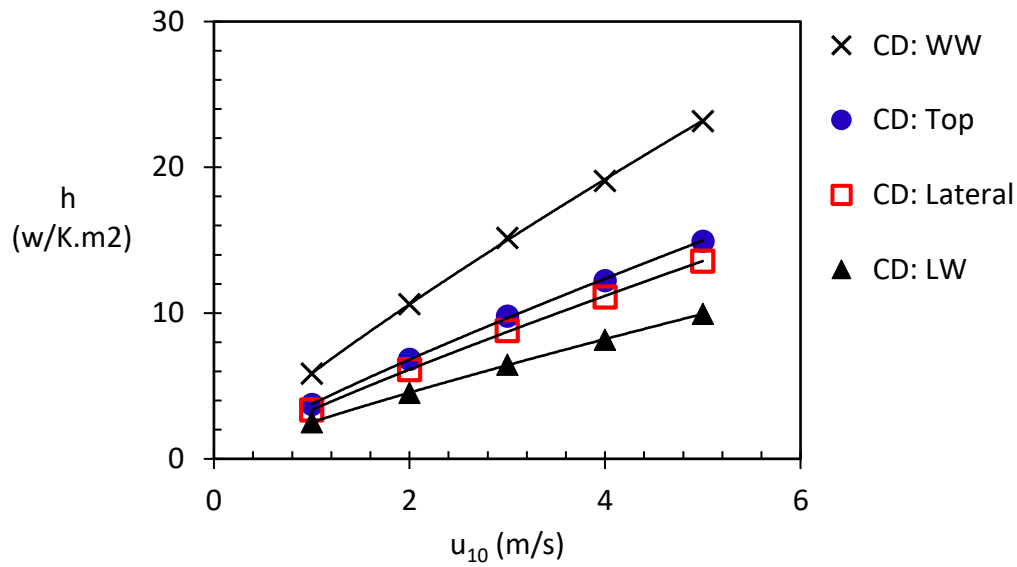


Figure 4.4 Heat transfer coefficient versus wind speed for an isolated cube

Table 4.1 The equations required to fit the data in Figure 4.4.

| Surface | Equation | Coefficient of determination (R^2) |
|----------|----------------------------|--|
| Windward | $h = 5.86 * u_{10}^{0.85}$ | 0.9999 |
| Top | $h = 3.75 * u_{10}^{0.86}$ | 0.9997 |

4.2.3 Determination of coefficient C_s

In the isolated building case where $\alpha \sim 0$, the values of each bracketed term in Eq.4.27 is a constant. Since $b = 1/\ln(H/z_0) = 0.1388$, and by taking $A = 2.8$ (Karava et al. 2011); the coefficient $C_{s,i}$ in Eq.4.28 can be expressed in terms of C_s . Thus, for the windward surface,

$$C_{s,i} = C_s(0.8612)^m(0.3303)^m(0.8844)^m(1.345)^{m-1}[1.4707] \quad \text{Eq.4.29}$$

and, for the top surface,

$$C_{s,i} = C_s(0.8844)^m(1.345)^{m-1}[1.1555] \quad \text{Eq.4.30}$$

Thus, the values of C_s for each surface of the building can be found by inserting the corresponding values of m and $C_{s,i}$ from Table 4.1 into Eq.4.29. Table 4.2 summarizes the values of the model constants m , $C_{s,i}$, and C_s for each surface (windward and top) of the building.

Table 4.2 Model constants for windward and top surfaces

| | Surface | |
|-----------|----------|------|
| Parameter | Windward | Top |
| m | 0.85 | 0.86 |
| $C_{s,i}$ | 5.86 | 3.75 |
| C_s | 13.46 | 3.76 |

4.3 Verification of the model

The validity of the overall procedure is confirmed by comparing the predictions of the model against values obtained from CFD simulation with a range of densities. To this end, additional set of CFD simulations with several densities ranging from very sparse building arrangement (equivalent to $\lambda = 0.1$, where $\lambda = \lambda_f = \lambda_p$) to dense cases up to $\lambda = 0.25$ are considered. Spacings between buildings and computational domains are maintained the same, while the width and height of buildings are changed according to changes in

densities. The densities considered are 0.01, 0.02, 0.025, 0.05, 0.1, 0.15, 0.2, 0.25, and building heights of 4.25, 6, 6.725, 9.5, 13.45, 16.45, 19, 21.25, 23.25, respectively.

An atmospheric boundary layer inlet condition with mean wind speed, u_{10} , of 4 m/s, and an aerodynamic roughness, z_o , of 0.1 is applied for all the CFD simulation cases. Turbulence intensity and length scale tensor data from Engineering Science Data Unit (ESDU) are used to compute the input values of Reynolds stress in the principal directions. The turbulence model employed is the Reynolds stress model (RSM), due to its demonstrated superiority of representing flows with highly 3D motion and strong secondary circulation. More details of the CFD simulation process and results can be found in chapter 3.

The CHTC values computed from the current model at each density are compared against the corresponding values obtained from the CFD simulation. Figure 4.5 (a and b) show the comparison of predicted data against data from CFD simulation for each surface, and Figure 4.6 shows the CHTC scatter plot for both surfaces. The results indicate the predicted model data for both surfaces of the building closely matches the values from CFD. The model is able to capture the rapid falling of CHTC in windward facades and a very gentle decreasing CHTC curve in top surfaces against the increase of density. It is, however, observed that there is a small deviation near $\lambda = 0.5$ and at a very dense canopy scenario. This may be attributed to the current model's assumption of a unified physics for all densities, despite the regimes of canopy flow, in which the trend (slope) of CHTC may vary for different ranges of densities (namely: isolated roughness flow, wake interference, and skimming flow regimes). Given, the value of $A = 2.8$, suggested by Karava et al. (2011) and adopted here, is obtained for an inclined roof surface, the agreement suggests the value

of A is not significantly altered by the orientation of the surfaces under dense building scenarios. The relatively small deviation in the curves may also be attributed to such local effects as separation, reattachment, and wake; that cannot be addressed with the current 1D analytical model.

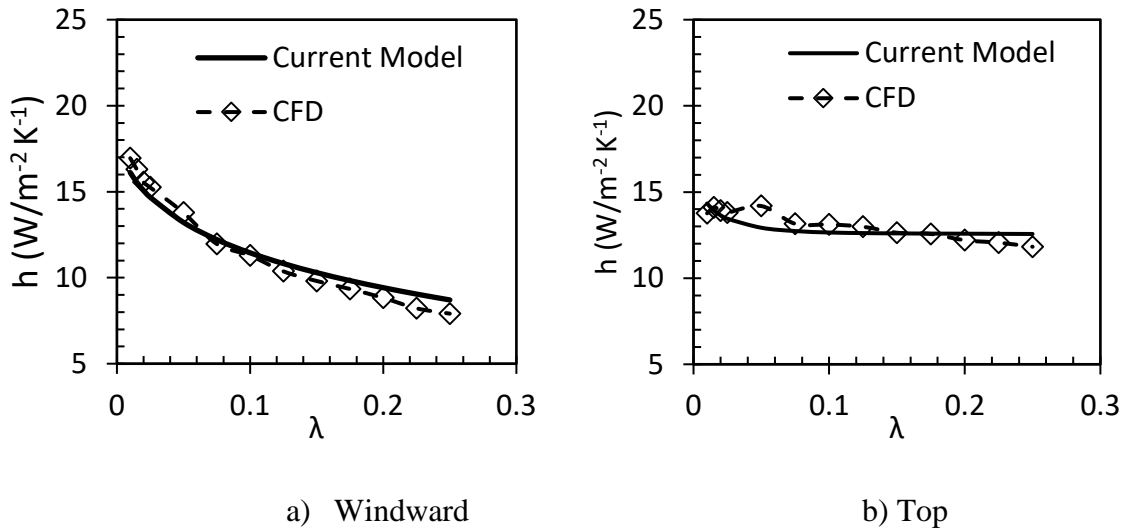


Figure 4.5 Comparison of CHTC data from model prediction and CFD simulation

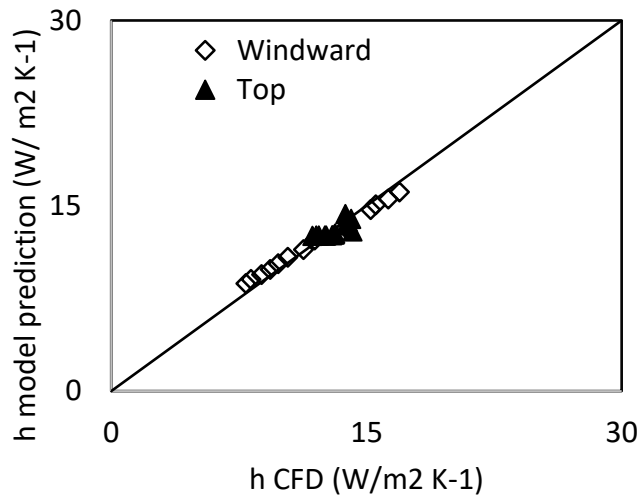


Figure 4.6 The scatter plot for CHTC of two surfaces

The sensitivity of a recurring parameter, the Jensen number, in the model is tested for orders of magnitude changes. The Jensen number (H/z_o) represents the relative roughness sizes of the built study area (H) and that of the upstream (background) approaching flow (z_o). The deviation of CHTC of the windward and top surfaces for errors of Jensen number within one order of magnitude amount to a maximum of 6% and 3%, respectively. Figure 4.7 shows the curves of CHTC calculated from the model for three H/z_o values of the windward surface. Therefore, smaller errors in H/z_o does not affect the CHTC results much.

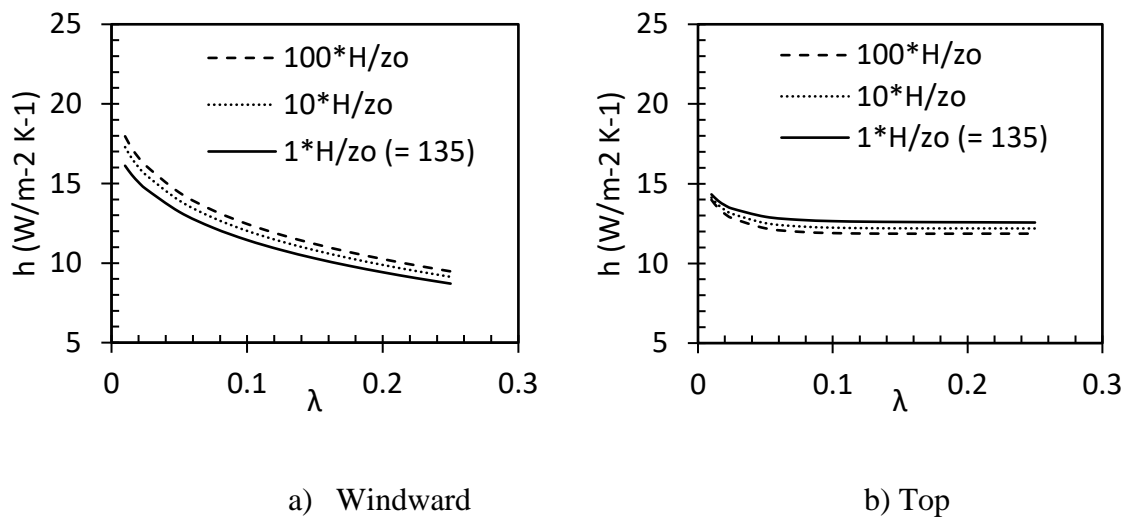


Figure 4.7 Sensitivity of H/z_o on CHTC for the windward and top surfaces

4.4 Conclusion

A semi-analytical model is developed for the computation of the convective heat transfer coefficient from buildings in an urban setting. The model is derived based on fundamental empirical conclusions found in literature, and an analytical mean velocity profile model developed recently. The results of the current model are verified against CFD simulation data reported recently. Considering the simplifying assumptions made, the agreements

achieved for both windward and top surfaces of the building are acceptable. The sensitivity of a recurring parameter in the model, i.e., Jenson number (H/z_o), is conducted, and its effect on CHTC is found to be minimal for very small changes. Both analytical mean velocity profile and the CFD simulation has been obtained for building like surfaces of cubical bluff bodies. The real heterogeneity of the urban form has not yet been investigated, and thus, the results of the current model remain better estimations, only to such conditions.

References

- Abdi, D., and Bitsuamlak, G.T. (2016). Wind flow simulations in idealized and real built environments with models of various level of complexity, *Wind & Structures*, 22 (4): 503-524.
- Abdi, D. and Bitsuamlak, G.T. (2014). Numerical evaluation of the effect of multiple roughness changes. *Wind and Structures*, 19(6): 585-601.
- K. Adamek, N. Vasan, A. Elshaer, E. English, G. T. Bitsuamlak (2017), Pedestrian level wind assessment through city development: A study of the financial district in Toronto, *Sustainable Cities and Societies*, 35:178-190.
- C. A. Arkon and Ü. Özkol (2013) Effect of urban geometry on pedestrian-level wind velocity, *Architectural Science Review*; 57:1, 4-19
- D. A. Awol, G. T. Bitsuamlak, F. Tariku (2017). Consistent analytical urban canopy layer velocity profile for dense building arrangement. *Americas Conference on Wind Engineering*, Gainesville, United States, 21-24 May 2017

D. A. Awol, G. T. Bitsuamlak, F. Tariku (2019). A More Reliable Estimate For External Convective Heat Transfer Coefficient From Building Surfaces in an Urban-Setting. CFD Society of Canada Conference, London, Canada, 2-5 June 2019.

A. Bejan (2004) Convective heat transfer, third edition, *John Wiley & Sons*.

B. Blocken, J. Carmeliet (2004) Pedestrian Wind Environment around Buildings: Literature Review and Practical Examples. *J Thermal Envelope and Building Science*; 28(2):107-159

B. Blocken, T. Stathopoulos, J. Carmeliet, J. L. M. Hensen (2011) Application of computational fluid dynamics in building performance simulation for the outdoor environment: an overview, *Journal of Building Performance Simulation* 4:157-184.

B. Blocken, T. Defraeye, D. Derome, J. Carmeliet (2009) High-resolution CFD simulations for forced convective heat transfer coefficients at the facade of a low rise building, *Build. Environ.* 44:2396-2412.

B. Blocken, W.D. Janssen T. van Hooff (2012) CFD simulation for pedestrian wind comfort and wind safety in urban areas-General decision framework and case study for the Eindhoven University campus, *Environmental Modelling & Software*; 30:15-34

I. P. Castro (2017) Are Urban-Canopy Velocity Profiles Exponential? *Boundary-Layer Meteorol* 164(3):337–351. DOI 10.1007/s10546-017-0258-x

A. Cenedese, G. Cosemans, H. Erbrink, R. Stubi (1997) Vertical profiles of wind, temperature and turbulence, COST Action 710: Preprocessing of Meteorological Data for Dispersion Modelling - Report of Working Group 3, October 1997

- L. Chen, J. Hang, M. Sandberg, L. Claesson, S. Di Sabatino, H. Wigo (2017) The impacts of building height variations and building packing densities on flow adjustment and city breathability in idealized urban models, *Build. Environ.*; 118:344-361
- H. Cheng, I. P. Castro (2002) Near-wall flow over urban-like roughness. *Boundary-Layer Meteorol* 104(2): 229–259
- M. K. Chyu, V. Natarajan (1991) Local heat/mass transfer distributions on the surface of a wall-mounted cube. *Trans ASME J Heat Trans*; 113(4):851–7.
- R. M. Cionco (1965) Mathematical Model for Air Flow in a Vegetative Canopy. *J. Applied Meteorol.* 4:517–522
- O. Coceal, S. E. Belcher (2004) A canopy model of mean winds through urban areas. *Q J Roy Meteorol Soc* 130(599):1349–1372
- O. Coceal, T. G. Thomas, I. P. Castro, S. E. Belcher (2006) Mean flow and turbulence statistics over groups of urban-like cubical obstacles. *Boundary-Layer Meteorol* 121:491-519
- I. R. Cowan (1968) Mass, heat and momentum exchange between stands of plants and their atmospheric environment. *Q J Roy Meteorol Soc* 94:523–544
- T. Defraeye, B. Blocken, J. Carmeliet (2011). Convective heat transfer coefficients for exterior building surfaces: Existing correlations and CFD modelling, *Energy Conversion and Management* 52:512–522

- S. Di Sabatino, R. Buccolieria, B. Pulvirentib, R. Britte (2007) Simulations of pollutant dispersion within idealized urban-type geometries with CFD and integral models, *Atmospheric Environment*; 41:8316–8329
- Y. Du, C. M. Mak, B. Tang (2018) Effects of building height and porosity on pedestrian level wind comfort in a high-density urban built environment, *BUILD SIMUL*; 11: 1215–1228
- A. Elshaer, A. Gairola, K. Adamek, G. Bitsuamlak (2017) Variations in wind load on tall buildings due to urban development. *Sustainable cities and society*; 34, 264-277.
- J. Franke, A. Hellsten, H. Schlünzen, B. Carissimo (Eds.) (2007) Best practice guideline for the CFD simulation of flows in the urban environment, COST Office, Brussels, 3-00-018312-4.
- M. G. Emmel, M. O. Abadie, N. Mendes (2007) New external convective heat transfer coefficient correlations for isolated low-rise buildings, *Energ Build*. 39:335-342.
- L. Evangelisti, C. Guattari, P. Gori, F. Bianchi (2017) Heat transfer study of external convective and radiative coefficients for building applications, *Energ Build*. 151:429–438
- S.B. Grimmond, M. Roth, T.R. Oke, Y.C. Au, M. Best, R. Betts, G. Carmichael, H. Cleugh, W. Dabberdt, R. Emmanuel, E. Freitas, K. Fortuniak, S. Hanna, P. Klein, L.S. Kalkstein, C.H. Liu, A. Nickson, D. Pearlmutter, D. Sailor and J. Voogt (2010) *Climate and More Sustainable Cities: Climate Information for Improved Planning and Management of Cities (Producers Capabilities Perspective)*; *Procedia Environmental Sciences*; 1:247–274

J. Hang, Y. Li, M. Sandberg, R. Buccolieri, S. Di Sabatino (2012) The influence of building height variability on pollutant dispersion and pedestrian ventilation in idealized high-rise urban areas, *Build. Environ.*; 56:346-360

N. Ito, K. Kimura, J. Oka (1972) A field experiment study on the convective heat transfer coefficient on exterior surface of a building. *ASHRAE Trans*; 78(1):184–91

H. Janssen, B. Blocken, J. Carmeliet (2007) Conservative modelling of the moisture and heat transfer in building components under atmospheric excitation, *Inter J Heat Mass Trans* 50:1128–1140

W. Jürges (1924) The heat transfer at a flat wall (*Der Wärmeübergang an einer ebenen Wand*), *Beihefte zum Gesundh.-Ing.* 1:19.

Kahsay, M.T., Bitsuamlak, G.T., Tariku F. (2018). Numerical analysis of convective heat transfer coefficient for building facades. *Journal of Building Physics*, 10.1177/1744259118791207.

Kahsay, M.T., Bitsuamlak, G.T., Tariku F. Effect of local exterior convective heat transfer on high-rise building energy consumption. *Building Simulation*, in publication.

P. Karava, C. M. Jubayer, E. Savory (2011) Numerical modelling of forced convective heat transfer from the inclined windward roof of an isolated low-rise building with application to photovoltaic/thermal systems. *Applied Thermal Engineering*; 31:1950-1963

H.M. Künzl, K. Kiessl (1997) Calculation of heat and moisture transfer in exposed building components. *Int. J. Heat Mass Transf.*, 40:159–167

J. Liu, J. Srebric, N. Yu (2013) Numerical simulation of convective heat transfer coefficients at the external surfaces of building arrays immersed in a turbulent boundary layer, *Int. J. Heat. Mass Transf.* 61:209-225.

A. K. Lo (1995) Determination of zero-plane displacement and roughness length of a forest canopy using profiles of limited height. *Boundary-Layer Meteorol*; 75(4):381–402

D. L. Loveday, A. H. Taki (1996) Convective heat transfer coefficients at a plane surface on a full-scale building facade. *Int J Heat Mass Trans*; 39(8):1729–42

R. W. Macdonald (2000) Modelling the mean velocity profile in the urban canopy layer. *Boundary Layer Meteorol* 97(1):25–45

E. R. Meinders (1998) Experimental Study of Heat Transfer in Turbulent Flows over Wall Mounted Cubes, PhD thesis, Technische Universiteit Delft.

E. R. Meinders, K. Hanjalic, R. J. Martinuzzi (1999) Experimental study of the local convection heat transfer from a wall-mounted cube in turbulent channel flow. *Trans ASME J Heat Trans*; 121(3):564–73.

M. Mirsadeghi, D. Costola, B. Blocken, J. L. M. Hensen (2013) Review of external convective heat transfer coefficient models in building energy simulation programs: implementation and uncertainty, *Appl. Therm. Eng.* 56:134-151.

H. Montazeri, B. Blocken, D. Derome, J. Carmeliet, J. L. M. Hensen (2015) CFD analysis of forced convective heat transfer coefficients at windward building facades: influence of building geometry, *J. Wind Eng. Ind. Aerodyn.* 146:102-116.

- P. Moonen, T. Defraeye, V. Dorer, B. Blocken, J. Carmeliet (2012) Urban Physics: Effect of the micro-climate on comfort, health and energy demand. *Frontiers of Architectural Research*; 1:197–228
- H. Nakamura, T. Igarashi, T. Tsutsui (2001) Local heat transfer around a wall-mounted cube at 45° to flow in a turbulent boundary layer. *Int J Heat Mass Trans*; 24(6):807–15.
- V. Natarajan, M. K. Chyu (1994) Effect of flow angle-of-attack on the local heat/mass transfer from a wall-mounted cube. *Trans ASME J Heat Trans*; 116(3): 552–60.
- B. Nicceno, A.D.T. Dronkers, K. Hanjali (2002) Turbulent heat transfer from a multi-layered wall-mounted cube matrix: a large eddy simulation, *Int J Heat and Fluid Flow*, 23(2)173-185
- T. R. Oke (1988) Street design and urban canopy layer climate. *Energ Build* 11(1-3)103-113
- J. A. Palyvos (2008) A survey of wind convection coefficient correlations for building envelope energy systems' modeling, *Appl. Therm. Eng.* 28:801-808.
- H. A. Panofsky and J.A. Dutton (1984) *Atmospheric turbulence*. Wiley, New York
- D. A. Quintela, D. X. Viegas (1995) Convective heat losses from buildings. In: J.E. Cermak, A.G. Davenport, E. J. Plate, D. X. Viegas, editors. *Wind climate in cities*. The Netherlands: Kluwer Academic Publishers; p. 503–22.
- J. C. Simonich, P. Bradshaw (1978) Effect of free-stream turbulence on heat transfer through a turbulent boundary layer, *Journal of Heat Transfer*; 100:671-677.

E. M. Sparrow, J. W. Ramsey, E. A. Mass (1979) Effect of finite width on heat transfer and fluid flow about an inclined rectangular plate, *J. Heat. Transf.* 101:199-204.

T. Stathopoulos, H. Wu (1995) Generic models for pedestrian-level winds in built-up regions, *J. Wind Eng. Ind. Aerodyn.* 54-55:515-525.

N. S. Sturrock (1971) Localized boundary layer heat transfer from external building surfaces. PhD Thesis, University of Liverpool

C.W. Tsang, K.C.S. Kwok, P.A. Hitchcock (2012) Wind tunnel study of pedestrian level wind environment around tall buildings: Effects of building dimensions, separation and podium, *Build. Environ.*; 49:167-181

UN Department of Economic and Social Affairs (UN - DESA): World urbanization prospectus: The 2018 revision, May 2018 New York.

UN-Habitat, Cities and Climate Change: Global Report on Human Settlements 2011(Earthscan: London and Washington, D.C., 2011), 92

X. I. A. Yang, J. Sadique, R. Mittal, C. Meneveau (2016) Exponential roughness layer and analytical model for turbulent boundary layer flow over rectangular-prism roughness elements. *J Fluid Mech* 789:127–165

W. You, Z. Gao, Z. Chen and W. Ding (2017) Improving Residential Wind Environments by Understanding the Relationship between Building Arrangements and Outdoor Regional Ventilation, *Atmosphere*; 8:102

C. Yuan, E. Ng, L. K. Norford (2014) Improving air quality in high-density cities by understanding the relationship between air pollutant dispersion and urban morphologies, *Build. Environ.*; 71:245-258

W. Wang (2014) Analytically modelling mean wind and stress profiles in canopies. *Boundary-Layer Meteorol* 151(2)239–256

K. Wang, R. Chiou (2006) Local mass/heat transfer from a wall-mounted block in rectangular channel flow. *Heat Mass Trans*; 42(7):660–70.

Chapter 5

5 External convective heat transfer coefficient from surfaces of building stocks in quasi-heterogeneous setting

5.1 Introduction

The need for consideration of the influence of urban microclimate on CHTC from building surfaces has been argued in some studies (Moonen et al. 2012, Blocken et al. 2011, van Hoof et al. 2010). Chen et al. (2017) maintained the critical nature of this influence. The effect of the sheltering from neighboring buildings has been considered in site/configuration specific studies (Mirsadeghi et al. 2013, Liu et al. 2015, Allegrini et al. 2012, Liu et al. 2007). Awol et al. (2019) and chapter 3 stated the significant scatter in existing CHTC correlations have roots in the challenge of sufficiently addressing the microclimatic influences. Changes in CHTC are also reported by recent attempts to account for the impact of the height of buildings alone by Montazeri et al. (2015) and Meseret et al. (2017). Efforts have also been made to address the issue through a local velocity reference condition. The results of this effort also demonstrate a discrepancy among reported estimates of CHTC (Ito et al. 1972, Sharples 19994, Loveday et al. 2004, Liu and Harris 2007).

The alteration that occurs to the local wind field is responsible for the changes that would arise on the CHTC from the building surfaces. The surrounding built arrangement (size, orientation, and packing), in turn, is responsible for the changes to the wind field. This has been recognized in several studies (Castro 2017, Adamek et al. 2017, Awol et al. 2017, Franke et al. 2007, Coceal et al. 2006, Coceal et al. 2004, Cheng et al. 2002, Macdonald 2000, Cionco et al. 1998, Stathopoulos et al. 1995, Oke 1988). Several of the CHTC correlations in literature are obtained from laboratory and field studies (Vereecken et al. 2018, Evangelisti et al. 2017, Liu et al. 2007, Hagishima et al. 2003, Loveday et al. 1996, Jayamaha et al. 1996, Chyu et al. 1991, Sharples 1984, Sparrow et al. 1979, Kelnhofer and Thomas 1976, Ito et al. 1972, Jürges 1924). However, recently, validated CFD simulations has been used to successfully develop correlations for CHTC (Kahsay et al. 2018, Montazeri et al. 2017, Montazeri et al. 2015, Liu et al. 2013, Karava et al. 2011, Defraeye et al. 2010, Blocken et al. 2011, Blocken et al. 2009, Emmel et al. 2007). Further, Mirsadeghi et al. 2013, Defraeye et al. 2011, and Palyvos 2008 have conducted an extensive review of literature on the external convective heat transfer coefficient.

Meinder (1998) conducted an experiment on a row of cubes to investigate the effect of neighboring obstacles on CHTC from a cube surface. Lui et al. (2013) examined the effect by considering a 2D array of cubes. The numerical study in chapter 2 and the analytical study by Awol et al. 2017 have shown the effect of urban packing density on CHTC (from building surfaces) for homogenous packing densities, more specifically for cases with equal frontal and planar densities ($\lambda_f = \lambda_p$, i.e., cubical buildings). The frontal packing density (λ_f), planar packing density (λ_p) are expressed as;

Figure 5.1 and Eq.5.1 and Eq.5.2 show definitions frontal and planar density; and how practical urban form translated into simplified homogeneous built arrays.

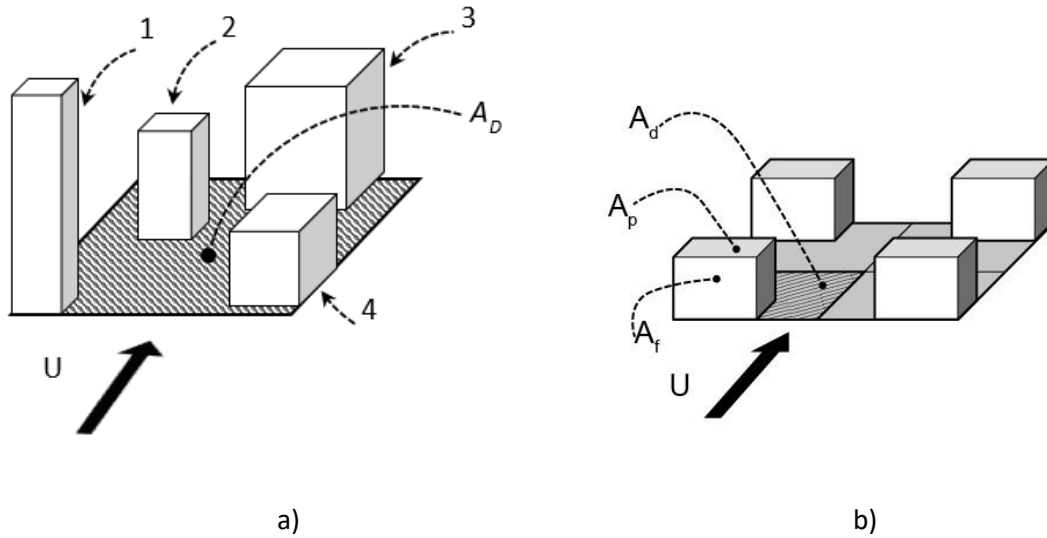


Figure 5.1 Definitions of frontal and planar density a) the schematic heterogeneous form b) the simplified homogeneous representation

$$A_D = \sum_1^n A_{d,i} \quad \text{Eq.5.1}$$

$$\lambda_f = \frac{\sum_1^n A_{f,i}}{A_D} = \frac{A_F}{A_D}, \quad \lambda_p = \frac{\sum_1^n A_{p,i}}{A_D} = \frac{A_P}{A_D} \quad \text{Eq.5.2}$$

where $A_{f,i}$ is the frontal area per each building, $A_{p,i}$ is the planar, and $A_{d,i}$ is the unit underlying lot area on the ground surface per each building. The representative frontal and planar area densities at neighborhood level are then found from the ratio of the total frontal (A_F) and the total top (A_P) surface areas for the total lot area, respectively.

Although the cubical building system may be a pragmatic first step in the idealization of the urban topology, it is an oversimplified one. Sets of more plausible nonhomogeneous idealizations are examined in this study numerically. This paper presents two sets of CFD based investigations to assess (i) the effect of change in frontal density on CHTC on building surfaces by only varying λ_f while λ_p is fixed, and (ii) the effect of change in planar density by varying only λ_p while λ_f is fixed, respectively. An array of planar and frontal density pair are simulated from various representative flow regimes. The same input conditions and the computational domain is set up for all cases, to limit the numerical effects on each simulation. The validation, the test sets, the computational setup, and the results of the study are discussed in the following sections.

5.2 Validation of the CFD model

The current CFD models are compared against the experimental findings of Merinders (1998) for validation purposes. First, the experiments from literature are briefly described, and second, the computational model that mimicked the experimental study is presented.

Meinders (1998) experiment was conducted in a chamber with a 500 mm x 50 mm test section. Nine cubes were aligned along the longitudinal flow direction and in the middle of the vertical channel wall. The cube size and the spacing between the cubes were 15 mm each. The outer layer of the cube was a 1.5 mm epoxy shell, and a copper core formed the inner part of the cube. The copper core was maintained at a temperature of 75 °C, and the conductivity of the epoxy material was approximately 0.24 W/m.K.

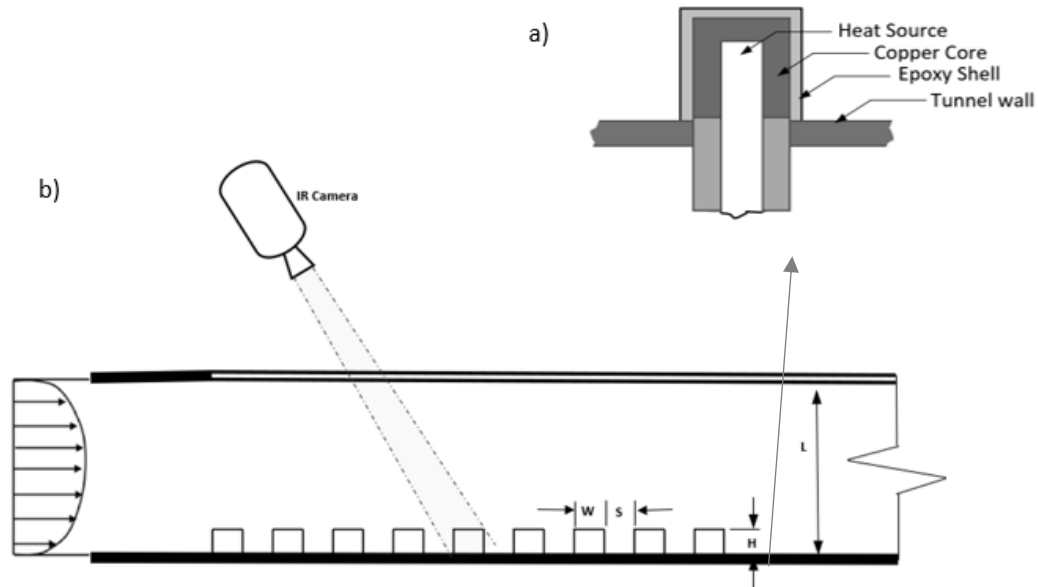


Figure 5.2 Schematic drawing of a) each cubical element, b) the setup of the experimental tunnel (plan view).

An infrared camera was used to scan the external surfaces of the cubes to provide the temperature distribution used to calculate the convective heat transfer coefficient; after accounting for radiative losses from supply flux. The inlet was supplied with a bulk velocity of 5.1 m/s, corresponding to an approximate Reynolds number of 5065 based on the height of the cubes. The temperature of oncoming flow at the inlet was set at 21 °C. Additional detail information can be found in Meinders (1998).

The computational model used for validation comprised a one to one scale replica of the tunnel section with the downstream fetch size of 20H to ensure the full inclusion of the downstream wake effects within the computational domain. Upstream fetch of 5H is considered, according to Tominaga et al. (2008) and Franke et al. (2011). The wall, on which the cubes are mounted, is oriented vertically to match the condition in the experiment as shown in Figure 5.3. The properties of epoxy material are applied to the cubical shell

model, to allow for the calculation of conduction heat transfer through the shell. The inner surface of all cube shells is set to be at a temperature of 75 °C. A temperature of 21 °C is applied to the incoming airflow. The outlet conditions are kept at zero pressure gradient. All lateral, top and bottom faces of the computational domain are considered adiabatic, no-slip wall boundaries. The outer surfaces of the cubes are set as no-slip walls and with non-adiabatic environmental conditions.

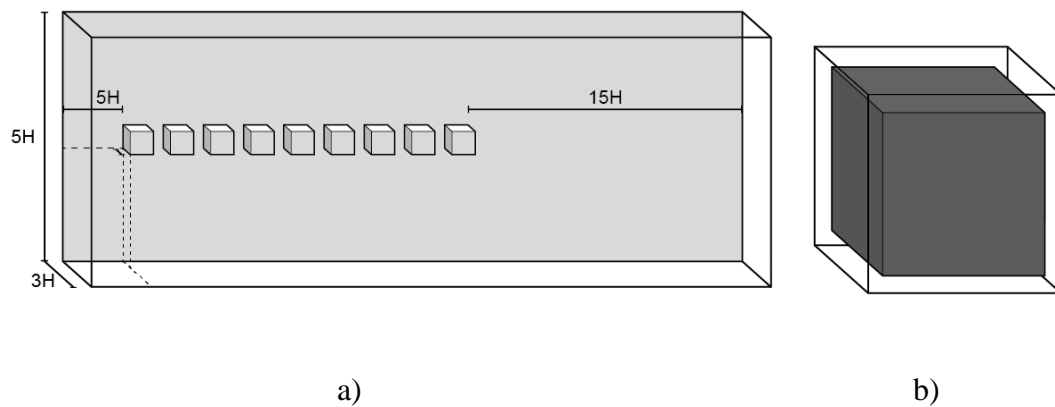


Figure 5.3 CFD implementation of the Meinders (1998) experimental setup a) the tunnel chamber b) each cubical shell element.

The lower near logarithmic and the middle uniform portions of the inlet velocity profiles are directly applied from the digitized table of the experimental inputs; provided in Meinders (1998). The upper laminar portion of the profile is obtained in the same manner, as mentioned in (chapter 2). The velocity and turbulent kinetic energy inputs are shown in Figure 5.4.

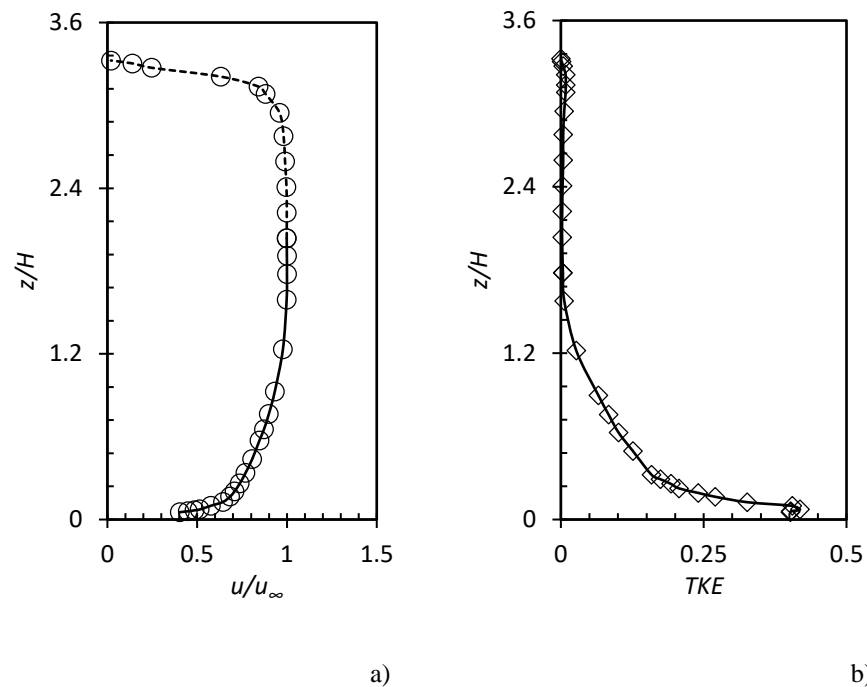


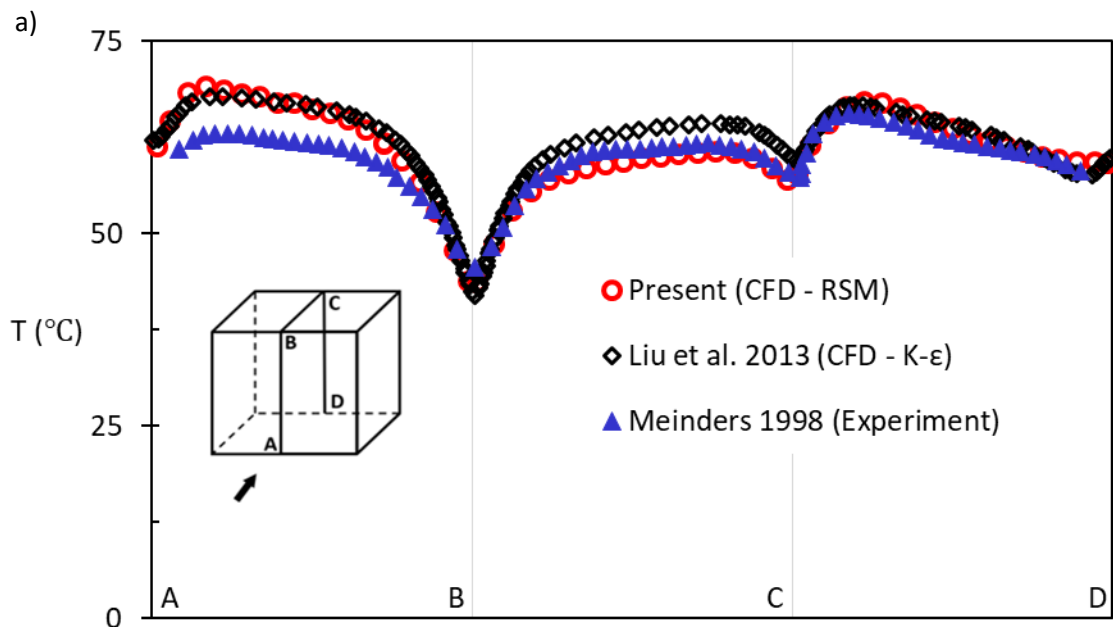
Figure 5.4 A) The adopted mean inlet velocity and B) turbulent kinetic energy profiles (solid line: data from the experiment; broken line: obtained from re-cycling method; symbol: input implemented in CFD)

Comparison is made against the records of temperature at the surfaces of the 5th cube in the row. The results are collected at the lines of intersection (AB, BC, and CD) between the cube and a longitudinally running vertical plane bisecting the cube, as shown in Figure 5.5. Liu et al. (2013) conducted the same measurement in a CFD environment with a k-epsilon, k-omega, and LES turbulence models. They found the k-epsilon model to perform better than the other two-equation model (k-omega). The results of the present measurement with Meinders (1998) and Liu et al. (2013), data obtained using the k-epsilon turbulence model, are indicated in Figure 5.5. On the top and leeward surfaces, the present RSM simulation can predict the experimental results well and better than the k-epsilon turbulence model simulation results. In the windward face, however, both the CFD

simulations match but with a margin of error from the experimental records. This may have been due to uncertainty both from spatial coordinate (experimental cube and spacing are very small in size) and temperature measurement itself (Meinders 1998). The artificial introduction of inlet data in the uppermost boundary layer through the method of recycling may have some effects.

More data has been gathered from a horizontal mid-line on the windward (EF), lateral (FG, HE), and leeward (GH) surfaces of the 5th cube as shown in Figure 5.5b; corresponding to the horizontal section plane cutting mid-height of the cubes. The results of this data emphasize the remarks made above.

In general, the present simulation reasonably predicts the temperature distribution on the surface of the building with an average deviation of less than 4 % from the experimental values. (additional information regarding this section can be found from chapter #3, and Meinders 1998)



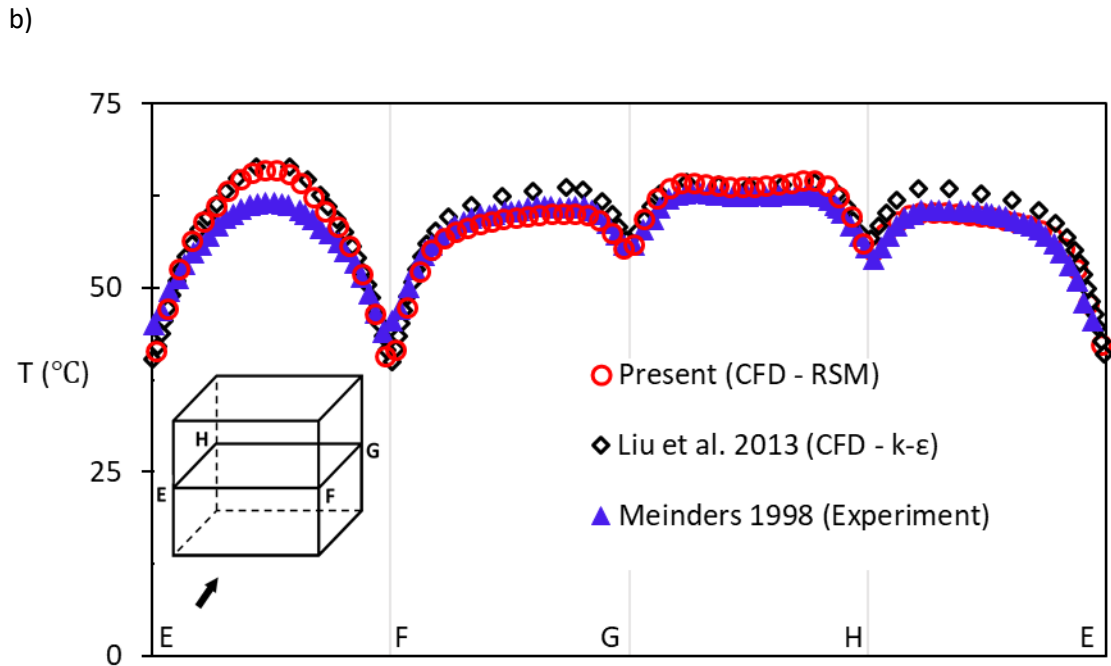


Figure 5.5 Comparison of simulated and experimental results along the paths: a) ABCD b) EFGHE

5.3 Description of simplified quasi-heterogeneous urban model

In this study, the nonhomogeneous urban topology (Figure 5.5a) is represented by an equivalent but simplified homogenous arrangement (Figure 5.5b). The equivalency is determined by maintaining equal frontal and planar density between the actual and simplified topology as defined in equations (2) and (3). The frontal and planar density parameters for nonhomogeneous urban packing density are described in Figure 5.5.

5.3.1 Set of densities considered

A planar-frontal density pair matrix is generated. The two sets of densities are generated corresponding to the two main objectives of the study, namely (i) effect of changing frontal density at fixed planar density and (ii) effect of changing planar density at fixed frontal density. A planar-frontal density pair matrix is generated representing these sets.

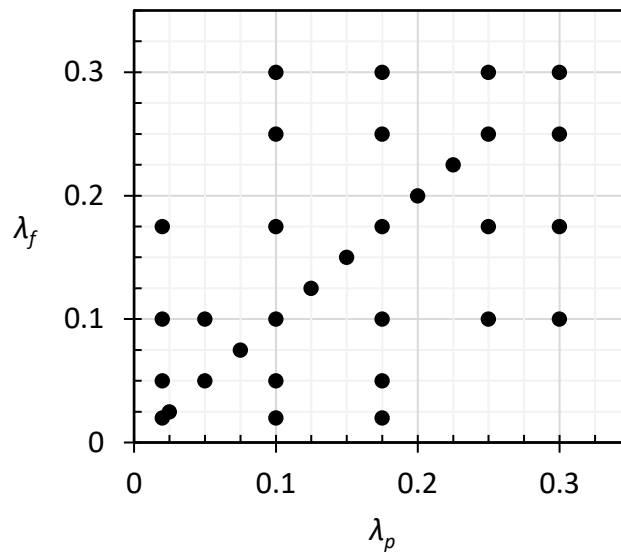


Figure 5.6 plot of λ_p versus λ_f showing the extent of the simulation set conducted

More specifically, the impact of changes in (i) frontal density (λ_f) and (ii) planar density (λ_p) on CHTC from building surfaces are tested. In each of the three scenarios, the planar density is kept fixed while varying the frontal densities. Figure 5.6 and Table 5.1 show the test scenarios considered.

Table 5.1 The sets of simulations conducted based on constant λ_p or λ_f

| Density Set | λ_f | λ_p |
|-------------|-------------|-------------|
| | 0.01 | 0.01 |
| A | 0.02 | 0.02 |
| | | 0.1 |
| | | 0.175 |
| B | 0.025 | 0.025 |
| C | 0.05 | 0.02 |
| | | 0.05 |
| | | 0.1 |
| | | 0.175 |
| D | 0.075 | 0.075 |
| E | 0.1 | 0.02 |
| | | 0.5 |
| | | 0.1 |
| | | 0.175 |
| | | 0.25 |
| | | 0.3 |
| F | 0.125 | 0.125 |
| G | 0.15 | 0.15 |
| H | 0.175 | 0.02 |
| | | 0.1 |
| | | 0.175 |
| | | 0.25 |
| | | 0.3 |
| I | 0.2 | 0.2 |
| J | 0.225 | 0.225 |
| K | 0.25 | 0.1 |
| | | 0.175 |
| | | 0.25 |
| | | 0.3 |
| L | 0.3 | 0.1 |
| | | 0.175 |
| | | 0.25 |
| | | 0.3 |

5.3.2 Computational domain, boundary conditions, and physics model

The representative urban density in each case is obtained from a hypothetical 2D array of buildings with 14 in stream-wise and infinite size in transverse. For this type of arrangement, the simplified representative flow can be obtained from the simulation of a single longitudinal strip of the array. For this to be a sound representation, the two parallel planes normal to the transverse direction those are placed half spacing away from the selected row on either side need to be assumed planes of symmetry (as shown in

Figure 5.7). The limits of the simulation domain are shown in

Figure 5.7, and the dimensions are shown in Figure 5.8.

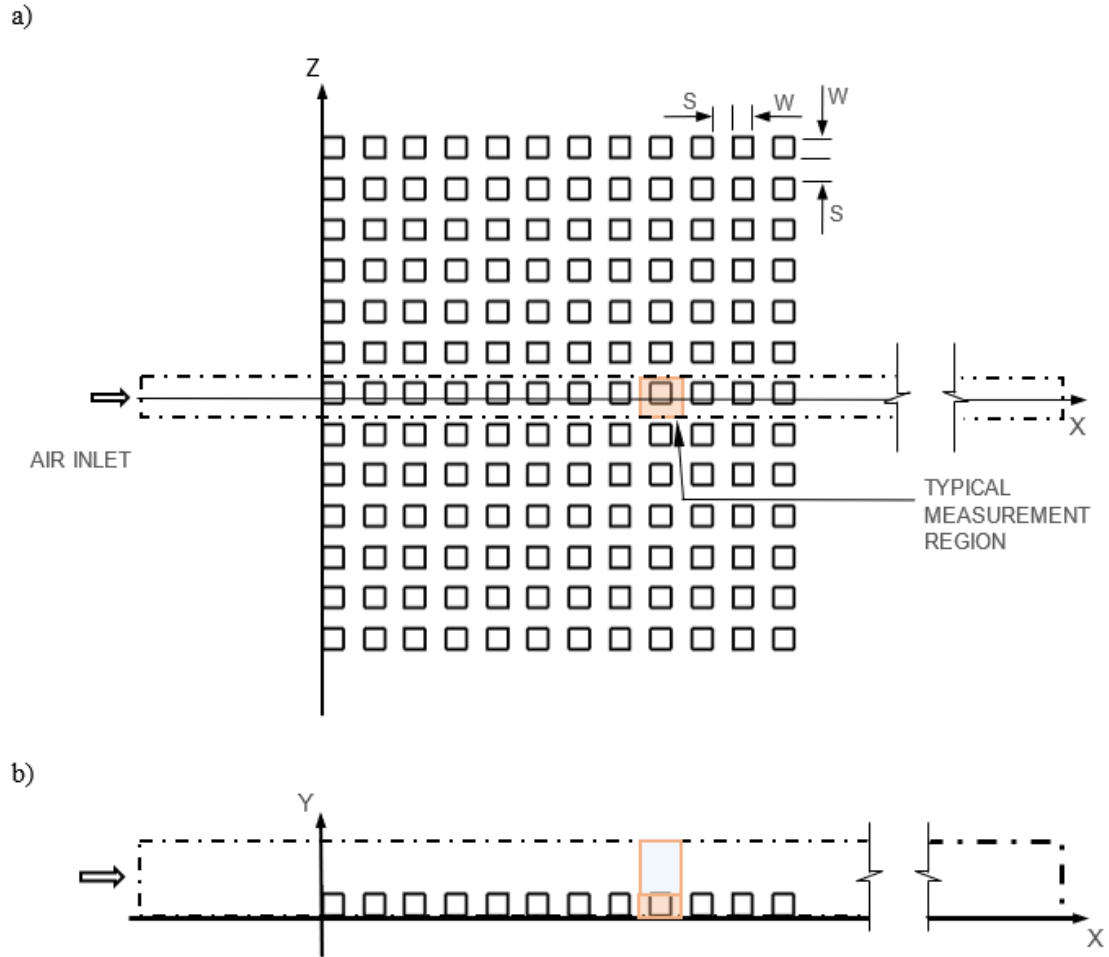


Figure 5.7 The building array with the study section (broken lines) and spacing parameters indicated on a) plan and b) elevation views.

The choice of the blocks' dimensions is such that the same domain and boundary conditions are used for all computational simulations. Accordingly, the domain is set up for the highest density (building size) case considered using Tominaga et al. (2008) and Franke et al. (2011).

The top surface of the domain is kept far enough from the top of the building and is assumed a symmetry plane. The bottom surface of the domain is set as an adiabatic no-slip wall. The block surfaces are wall boundaries at a uniform temperature of 30 °C. The

outlet of the domain is assigned a pressure outlet boundary condition (zero gradient along the stream).

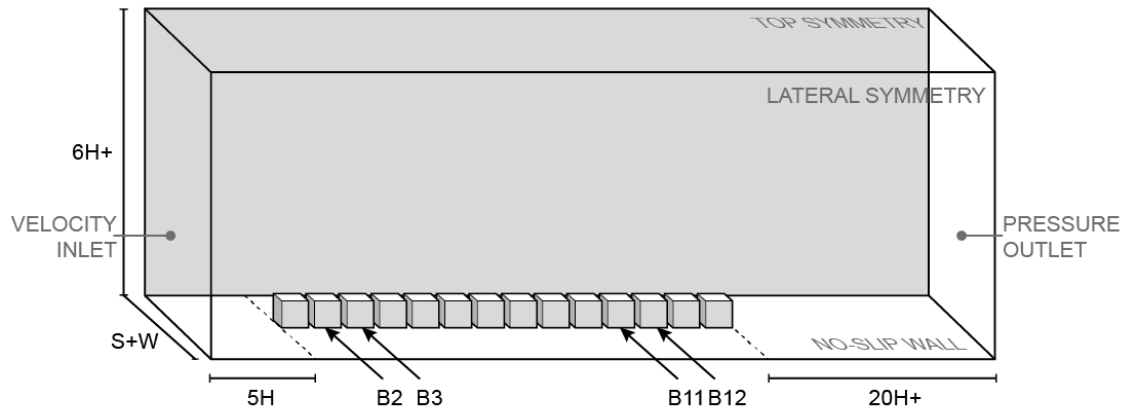


Figure 5.8 The computational domain, its dimensions, and boundary conditions (H height of cubic = 21.25 m).

The inlet boundary is an atmospheric boundary layer wind extracted from Engineering Science Data Unit (ESDU). The mean velocity profile has a velocity $u_{10} \approx 4.7$ m/s at 10 m height in an open terrain exposure condition (of aerodynamic roughness, $z_0 = 0.01$). The turbulence values applied at the inlet are the three principal components of the Reynolds stress tensor. These values are reduced from the components of turbulent intensity and length scale tensor values provided by ESDU (corresponding to the mean velocity and aerodynamic roughness combination mentioned above). Figure 5.9 shows the mean velocity and the principal components of the Reynolds stress values implemented.

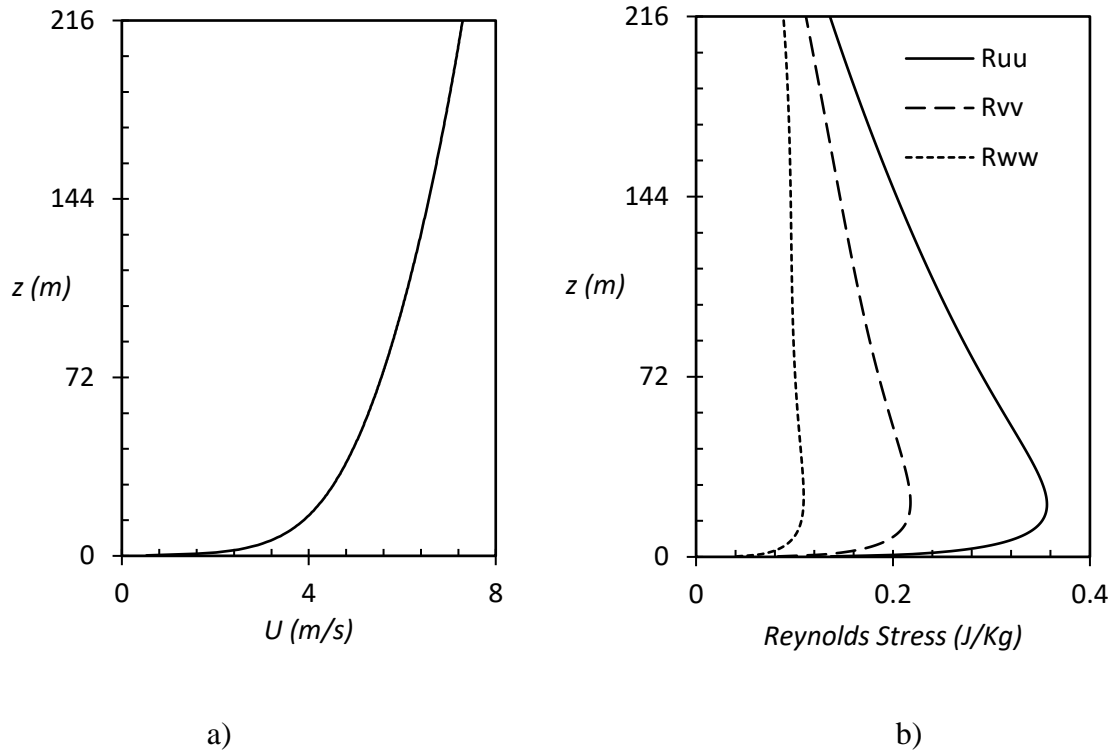


Figure 5.9 The inlet profiles of mean velocity and the principal components of Reynolds stress

Approximately $1.5 \cdot 10^6 - 2.5 \cdot 10^6$ polyhedral grid cells are generated. The grids are refined based on a volume around the blocks, the block surfaces, block edges, the wake region, and the computational domain wall boundary. Five prismatic layers of grids are applied near the wall boundaries (i.e., running parallel to the local surface). The width of the nearest cell to the surface is stretched by about 1.5 times its thickness. The resulting computational mesh has a y^+ value of 40 - 110, among which the lowest values are found near the block bases. An example of the computational grid used in one of the simulations is shown below (Figure 5.10).

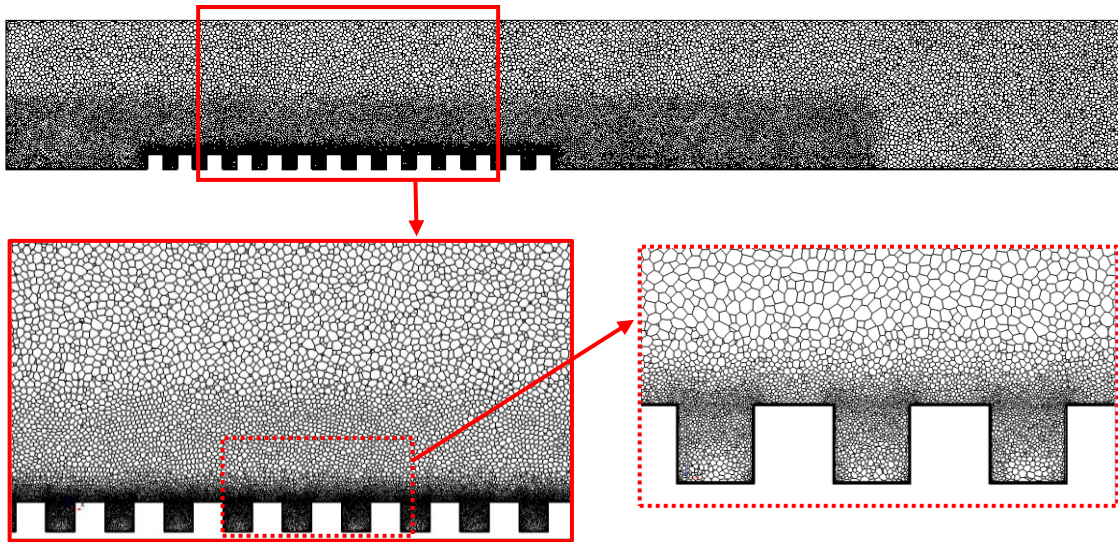


Figure 5.10 Elevation view of a sample mesh section

Steady Reynolds Averaged Navier-Stokes (RANS) and the energy equations are implemented to solve the problem in a CFD environment. The turbulence scheme used in the study is the second-moment closure method, Reynolds stress turbulence model (RSM). This method is important for flows like the present investigation where secondary flows and anisotropic turbulence are substantial (Speziale 1995, Speziale 1991, Murthy et al. 2008, Leschziner 1990, Launder et al. 1975). (more information regarding this section can be found from chapter #3).

5.4 Results and discussions

The results of the current study are plotted along with the data obtained from the equivalent uniform density (cubical array) simulations. Figure 5.11 shows the CHTC trend on each block along the longitudinal direction for all the surfaces. The CHTC values analyzed are those recorded from the downstream end of the arrays (11th and 12th blocks), at which the flow is considered fully developed.

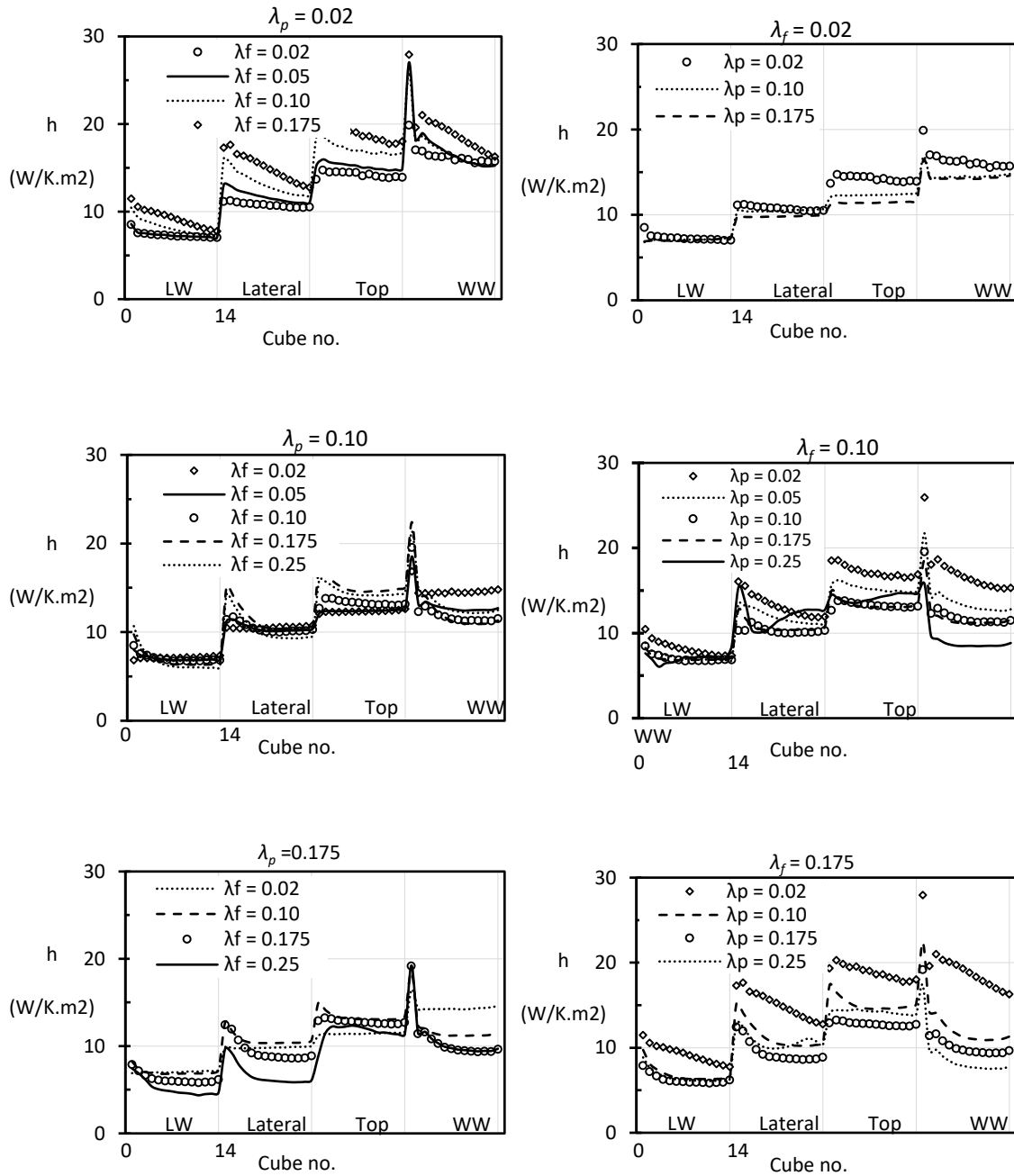
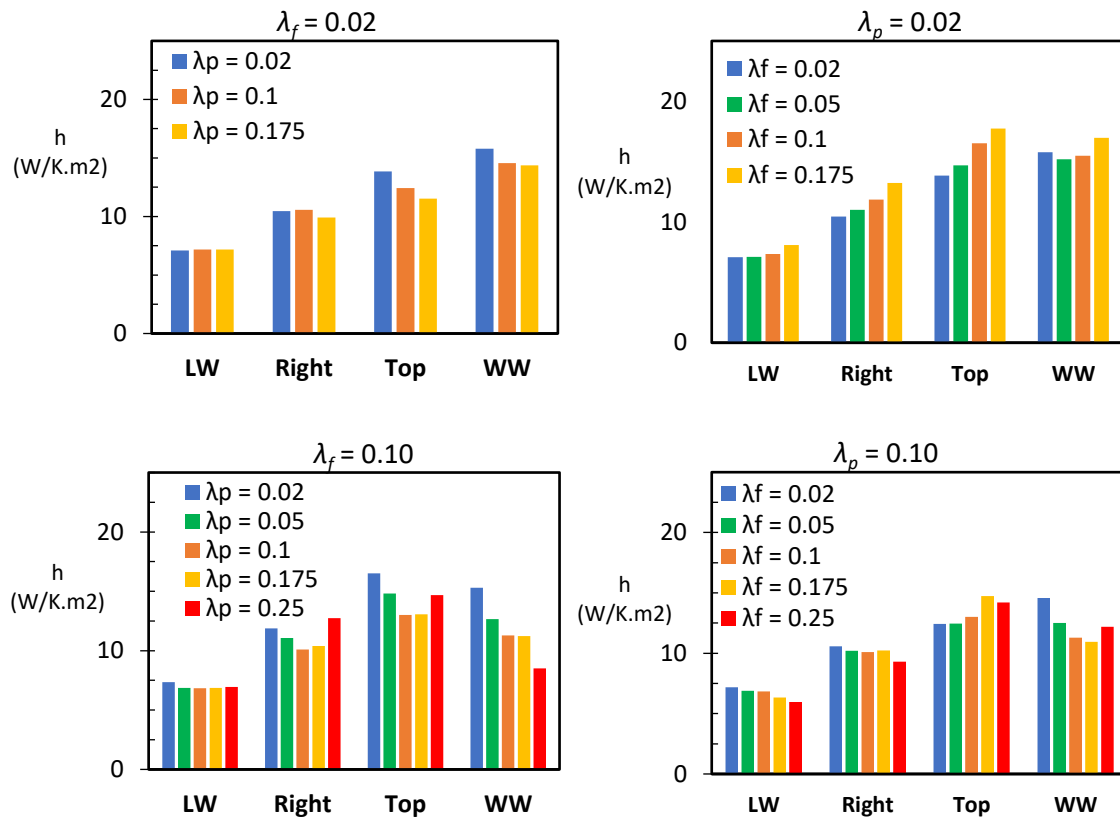


Figure 5.11 CHTC trend on each cube along the longitudinal direction for three densities in each category

Plots of CHTC for selected case outlined in Table 5.1 are shown in Figure 5.12

5.4.1 Effect of planar density

Figure 5.12 shows that the surface averaged CHTC consistently decreases with an increase in planar density for windward and leeward surfaces (with varying slopes at different frontal density ranges - regimes). An increase of planar density decreases the canopy flow space (cavity volume), which displaces a volume of the flow to the top inertial flow layer, thereby decreasing the momentum/flow speed under the canopy. This decrease in mean flow under the canopy thus results in lower CHTC compared to the lesser planar density case.



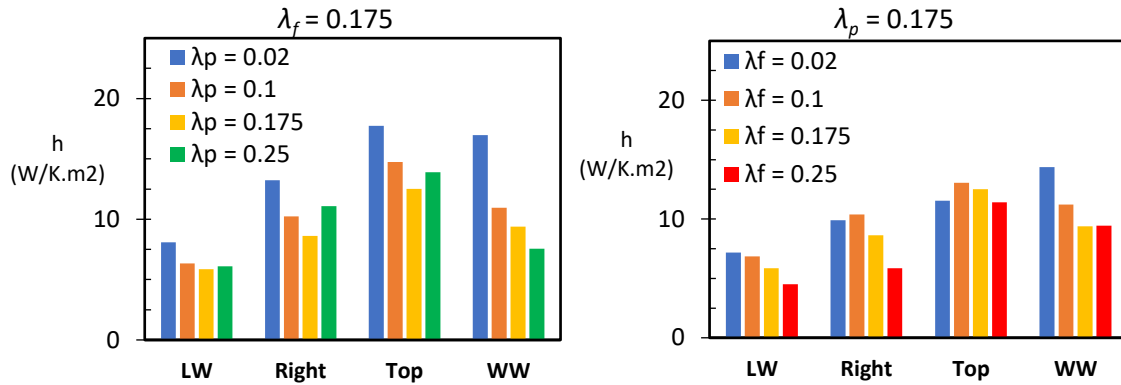


Figure 5.12 CHTC trend per planar/frontal density at each frontal/planar density regime for all surfaces

CHTC slightly decreases and then increases with planar density at all frontal densities, for the top and lateral surfaces. Larger planar densities are associated with higher aspect surfaces on the top and lateral sides. High aspect ratio surfaces, in turn, allow for increased attached flow, thus higher convective transfer.

5.4.2 Effect of frontal density

At lower planar density, an increase in frontal density resulted in a corresponding increase in CHTC for all surfaces. A higher frontal density combined with lower planar area density implies slender buildings with relatively larger spacing between themselves. The outcome being the flow surrounding the building surfaces is of a nearly isolated roughness regime, in which the flow system approaching the building is the full-blown ABL flow. Moreover, due to its slenderness, the higher portion of the building gets immersed into the higher wind velocity level of the ABL flow.

At higher planar densities, however, the CHTC decrease with an increase in frontal densities at different rates, except for Top and lateral surfaces for which the CHTC

increases before going to the decreasing trend. At higher planar densities, the corresponding flow space is considerably reduced because of the obstacles such that there is significantly limited flow in the canopy, hence lower CHTC.

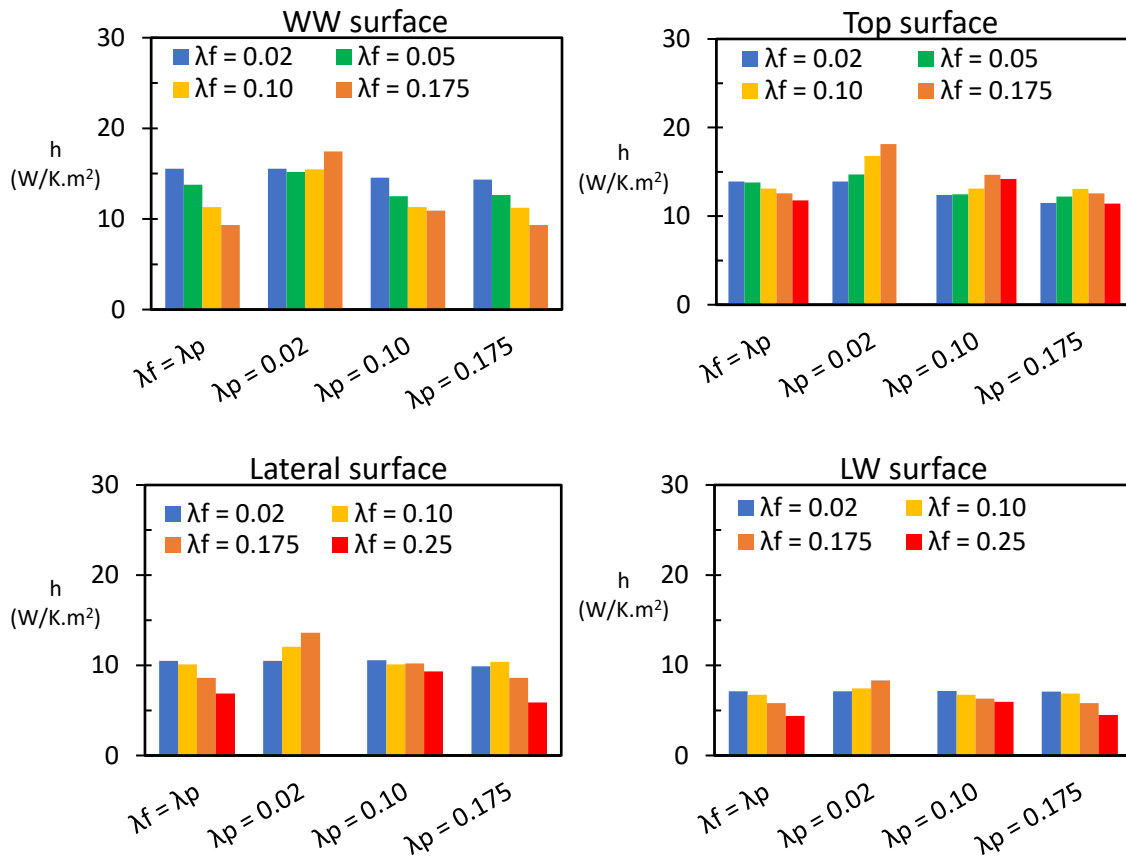


Figure 5.13 CHTC trend per frontal density at each planar density regime for each surface

5.5 Discussion

5.5.1 CHTC response surface

The above discussion hints, for each mean wind speed, that CHTC needs to be viewed as a three-dimensional response surface as a function of planar and frontal densities. The resulting mean CHTC response surface for the four surfaces of the building, generated from

a cubic polynomial fit of the simulated data, as shown in Figure 5.14. The figure indicates the ratio of CHTC at a given canopy density and the CHTC at the isolated building state (h_{dense}/h_{iso}) against the two packing density representations. The results are also shown in contour plots for additional clarity in Figure 5.15.

As shown in Figure 5.14 (and Figure 5.15), in general, for all surfaces, the highest CHTC value is obtained at a combination of high frontal and low planar density. The Lateral and top surface has additional peak CHTC points near high planar but low frontal densities. The lowest CHTC happens when the highest of the two densities (very dense scenario) overlap. The value of CHTC is found to be intermediate at the combination of low densities from both dimensions (frontal and planar).

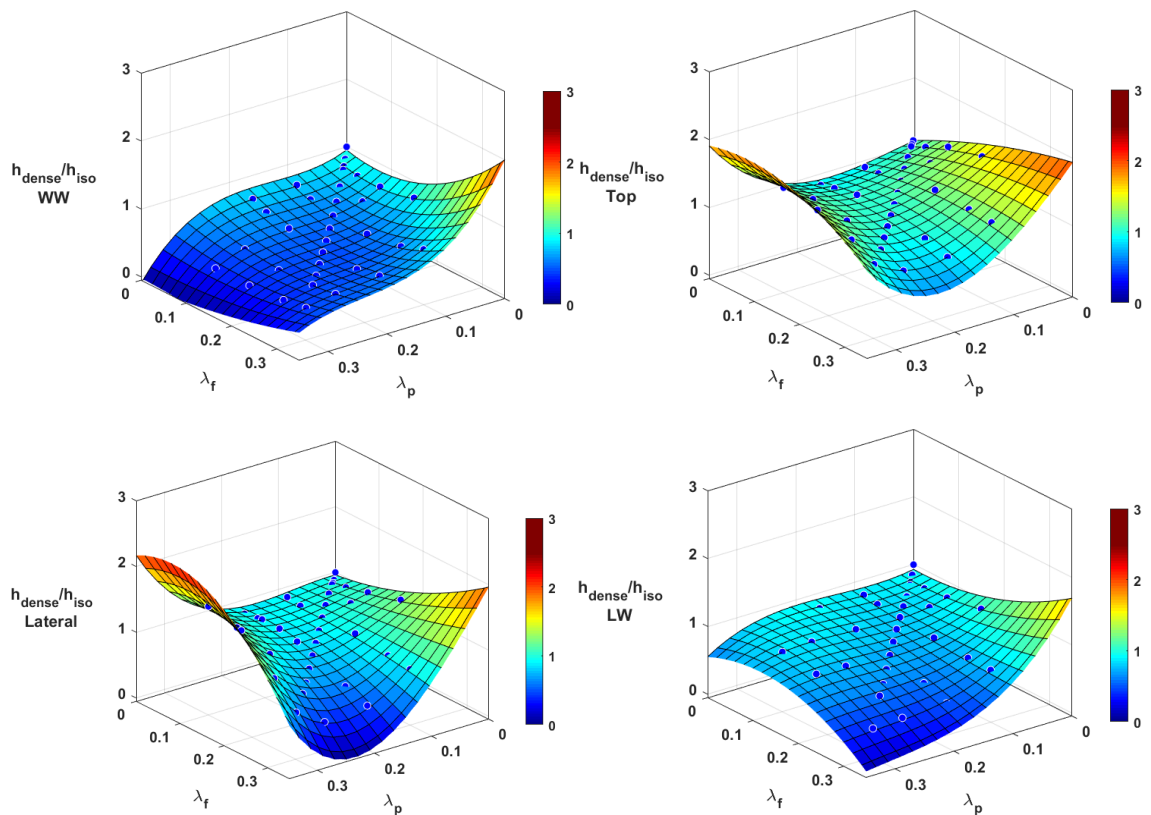


Figure 5.14 3D plots of CHTC for each surface per the value at the isolated condition

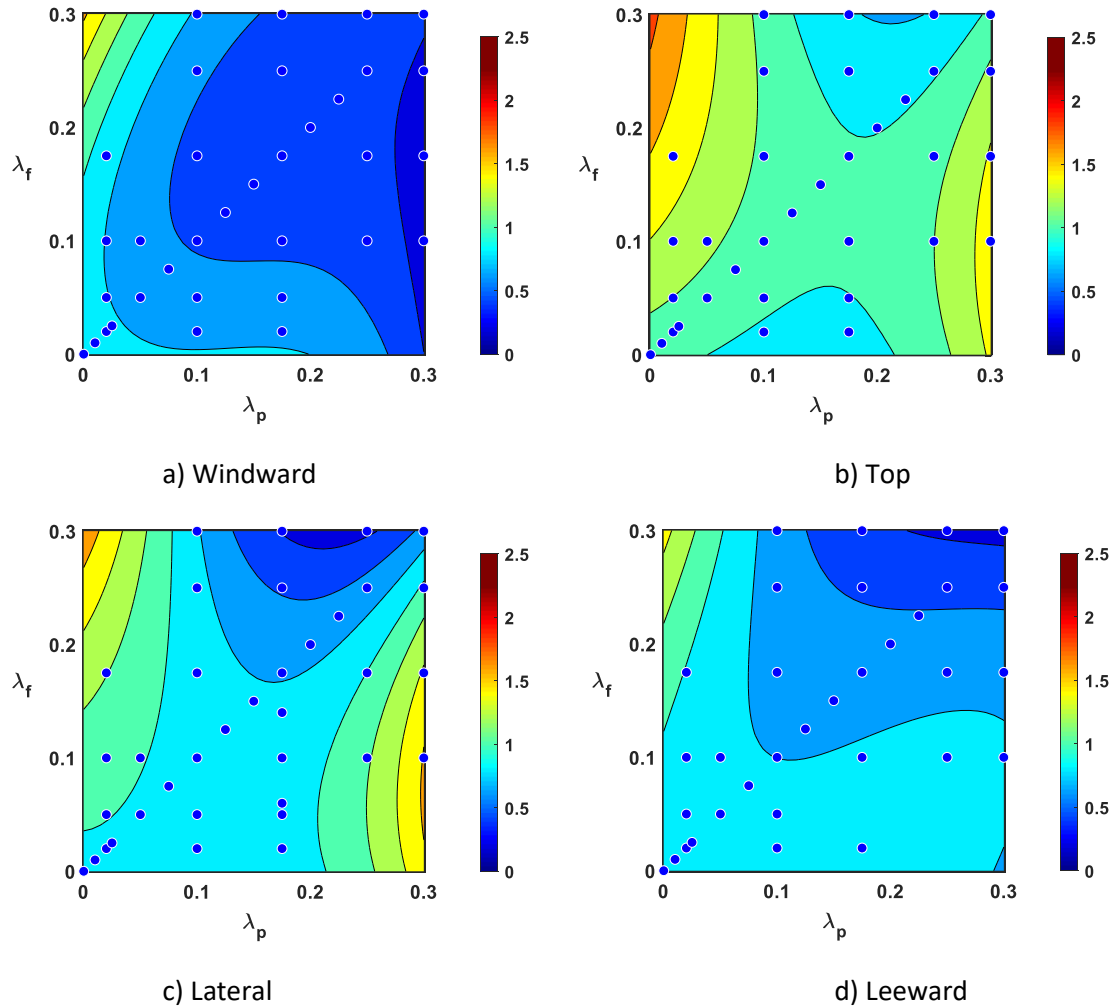


Figure 5.15 Contour plots of CHTC for each surface per the value at the isolated condition

The low-planar and high-frontal density combination (isolated slender buildings) give rise to a less disturbed ABL flow in the canopies. The relative slenderness of the obstacles under this scenario makes the tops of the buildings extend into the high velocity portion of the ABL flow. These two may be the reasons why the CHTC is relatively higher under this combination of densities. Figure 5.16 has the schematic representation of four extreme densities, along with the CHTC contours for the four surfaces. Figure 5.16 also shows the least flow space occurs when the density pair both become the highest, i.e., large footprint and tall buildings. This is also when the most disturbance to the ABL happens, hence

resulting in lowest mean velocity. This scenario, thus, corresponds to the lowest CHTC. However, there is an additional peak zone for lateral and top surfaces near high-planar and low-frontal density combination. This corresponds to short but large footprint buildings, with the longest side aligned to along wind direction. As shown in Figure 5.16, this zone can be described as having corresponded to relatively higher aspect lateral and top surfaces. The relative enlargement of these surfaces means a larger flow attachment region, and consequently, higher convection.

The simulation results also reveal the common claim that the windward surface provides the highest CHTC may not be a general fact. Thus, the windward CHTC contribution may be exceeded by CHTC from other surfaces depending on the density combinations. Figure 5.17 shows the global CHTC as the sum from all surfaces per the global value at the isolated building case. Moreover, Figure 5.18 indicates the CHTC from each surface in relation to the windward values (i.e., $\text{CHTC}_{\text{WW}}/\text{CHTC}_{\text{Surface}}$). The Windward value of CHTC may be exceeded by the top and Lateral values of CHTC at the high-planar and low-frontal density corner.

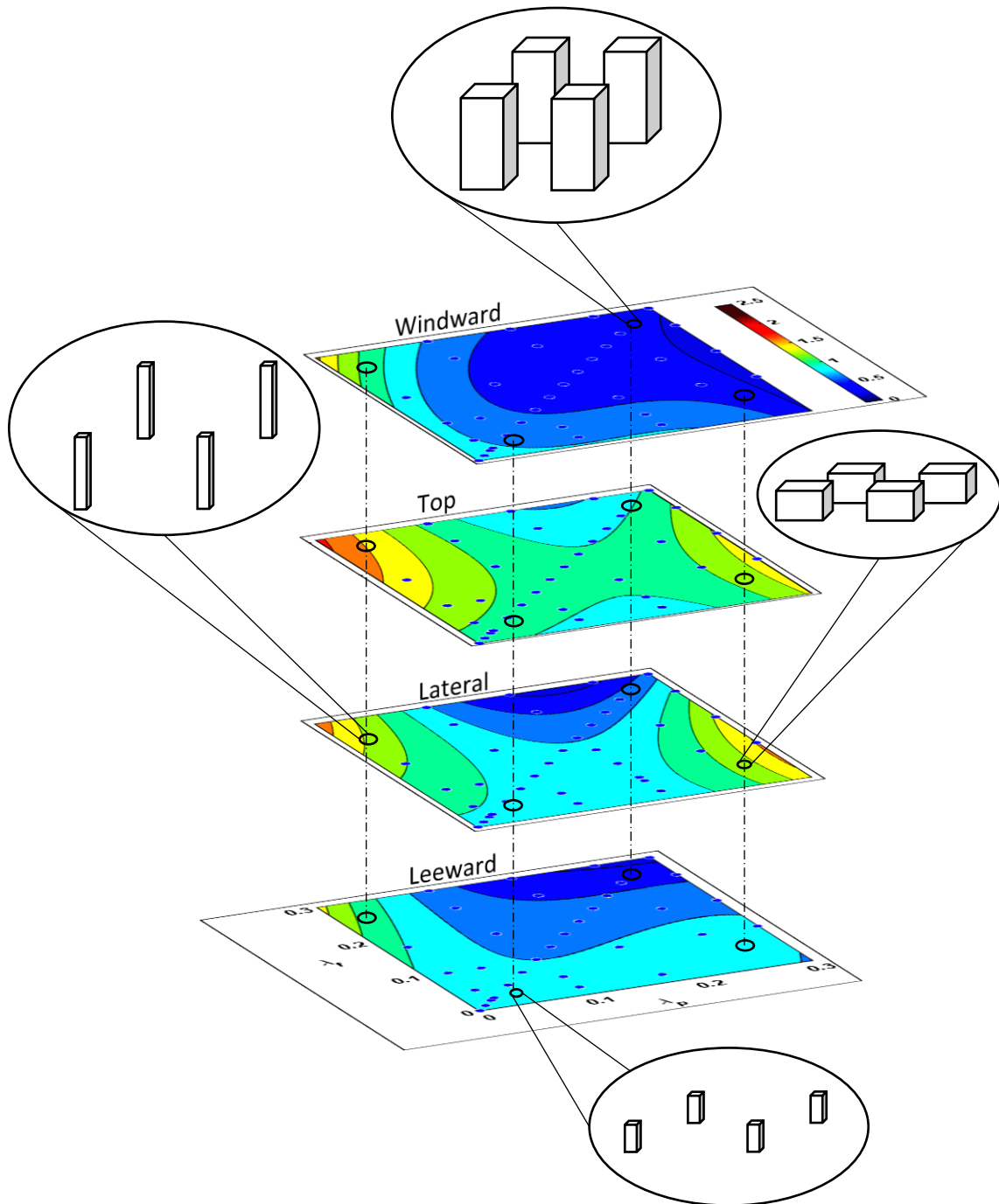


Figure 5.16 Contour plots of CHTC for each surface along with schematic representation densities at various corners

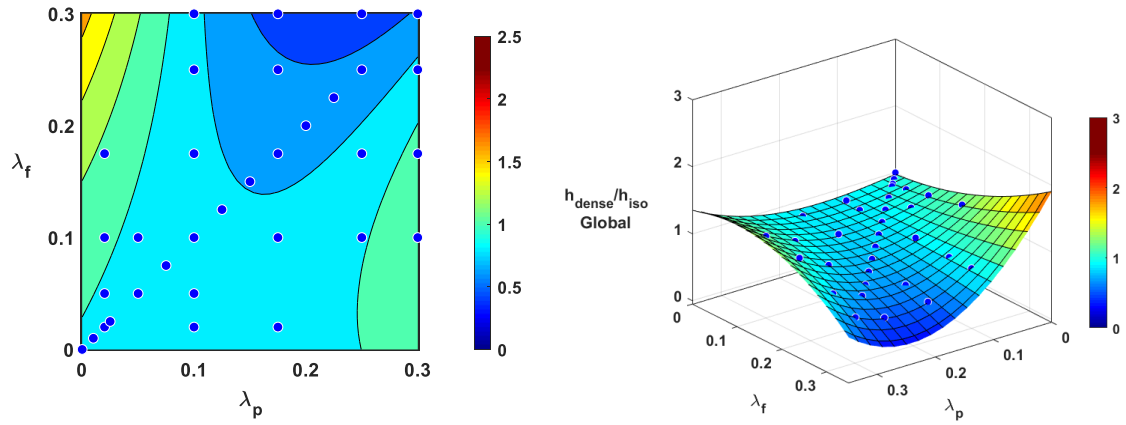


Figure 5.17 Contour and 3D plots of the global CHTC value per the value at the isolated condition

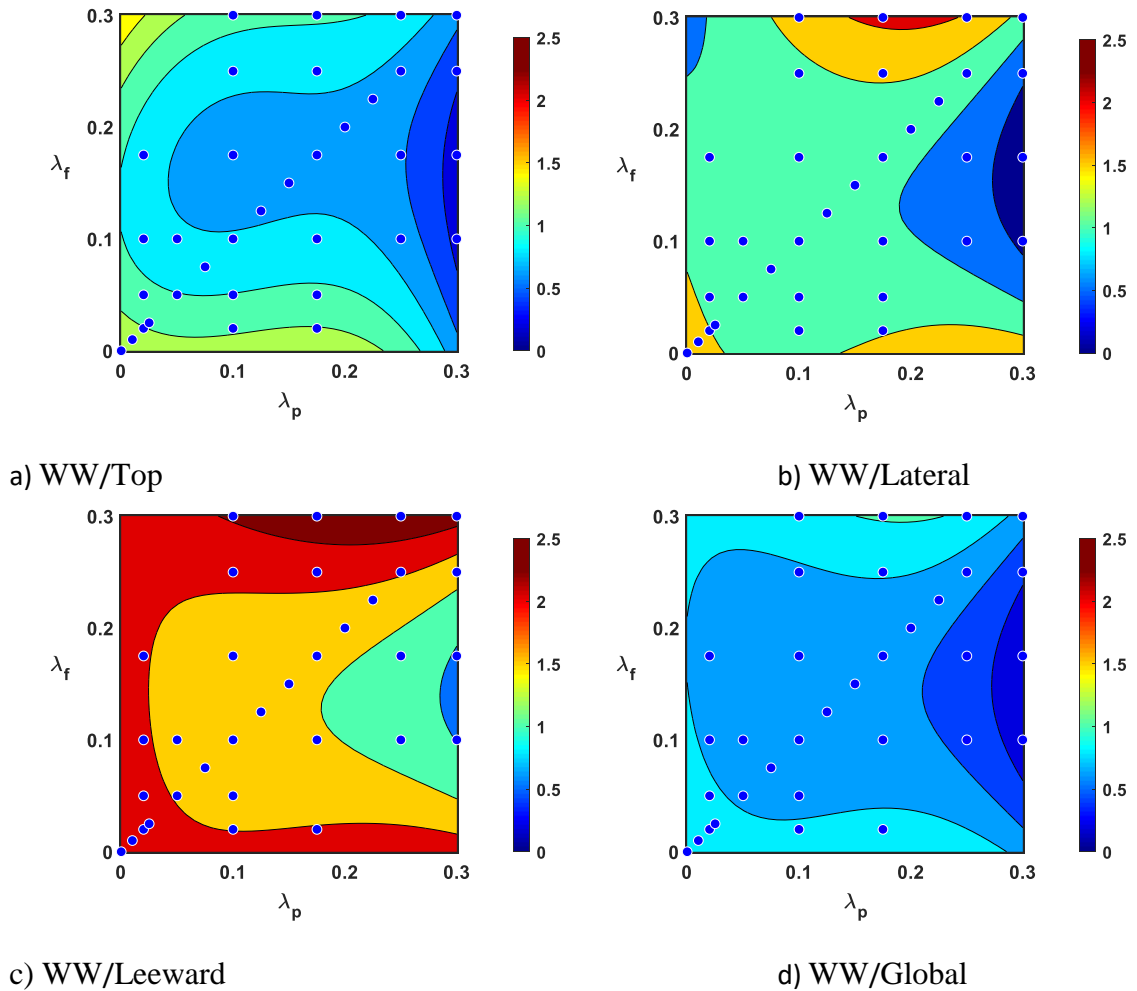


Figure 5.18 Contour plots of CHTC for each surface per the windward CHTC value at the same density

5.5.2 The CHTC surface fit equations

The resulting response surface ($CHTC/h_{iso}$) is fit to a homogeneous bivariate cubic polynomial model, corresponding to “Poly32” in MATLAB. The coefficients of the polynomial and bounds per 95% confidence are shown in the Table 5.2. The values of the goodness fit for the surface along all orientations is included. The polynomial has a form:

$$f(\lambda_f, \lambda_p) = p_{00} + p_{10} * \lambda_f + p_{01} * \lambda_p + p_{20} * (\lambda_f)^2 + p_{11} * \lambda_f * \lambda_p + p_{02} * (\lambda_p)^2 + p_{30} * (\lambda_f)^3 + p_{21} * (\lambda_f)^2 * \lambda_p + p_{12} * \lambda_f * (\lambda_p)^2$$

Table 5.2 Coefficients for the polynomials fit for the simulated CHTC data

| Coefficients (95% confidence) | Surfaces/orientation | | | |
|----------------------------------|----------------------------|-----------------------------|----------------------------|-----------------------------|
| | Windward | Top | Lateral | Leeward |
| p ₀₀ | 0.9551 (0.9441, 0.9662) | 1.101 (1.074, 1.128) | 0.968 (0.9519, 0.984) | 0.914 (0.8908, 0.9373) |
| p ₁₀ | -4.157 (-4.878, -3.436) | -2.136 (-3.917, -0.3537) | 0.4681 (-0.5824, 1.519) | -1.006 (-2.525, 0.5124) |
| p ₀₁ | -1.964 (-2.644, -1.284) | 3.268 (1.588, 4.949) | 0.1198 (-0.8709, 1.111) | -0.7509 (-2.183, 0.6814) |
| p ₂₀ | 38.3 (27.25, 49.35) | 1.366 (-25.93, 28.66) | -14.31 (-30.4, 1.784) | 11 (-12.27, 34.27) |
| p ₁₁ | -23.65 (-31.81, -15.49) | -15.56 (-35.72, 4.601) | -10.76 (-22.65, 1.127) | -10.16 (-27.35, 7.025) |
| p ₀₂ | 14.88 (11.22, 18.54) | -1.962 (-11, 7.077) | 11.75 (6.42, 17.08) | 10.21 (2.507, 17.92) |
| p ₃₀ | -106.8 (-149.6, -64.04) | 30.5 (-75.22, 136.2) | 51.28 (-11.05, 113.6) | -35.17 (-125.3, 54.94) |
| p ₂₁ | 87.75 (55.3, 120.2) | 32.41 (-47.75, 112.6) | 100.5 (53.23, 147.7) | 80.58 (12.25, 148.9) |
| p ₁₂ | -36.37 (-68.81, -3.921) | -23.82 (-104, 56.34) | -130.5 (-177.7, -83.23) | -87.89 (-156.2, -19.56) |
| Goodness fit | | | | |
| SSE | 0.004159 | 0.02538 | 0.008824 | 0.01844 |
| R-square | 0.9964 | 0.945 | 0.9901 | 0.9728 |
| Adjusted R ² | 0.9958 | 0.9357 | 0.9884 | 0.9681 |
| RMSE | 0.009407 | 0.02324 | 0.0137 | 0.01981 |

When the polynomial equation is expressed based on the benchmark case CHTC for isolated cube;

$$h = (C * u_{10}^m) * [p_{00} + p_{10} * \lambda_f + p_{01} * \lambda_p + p_{20} * (\lambda_f)^2 + p_{11} * \lambda_f * \lambda_p + p_{02} * (\lambda_p)^2 + p_{30} * (\lambda_f)^3 + p_{21} * (\lambda_f)^2 * \lambda_p + p_{12} * \lambda_f * (\lambda_p)^2]$$

5.5.3 The CHTC surface versus Land-use class designation of a neighborhood

Table 5.3 presents planar and frontal densities of city neighborhoods from different parts of North America. The table indicates the most practical range densities fall in the higher planar, but between low and high frontal densities. Thus, indicating the common assumption to use isolated buildings, and tests in the low planar density zone are less representative. The distribution of this densities on a λ_p versus λ_f graph is shown in Figure 5.19

Table 5.3 Practical frontal and planar density combinations of various neighborhoods of North American cities

| Locations | Land-use Class | λ_p | λ_f | Reference |
|-----------------------|----------------------|-------------|-------------|---|
| Vancouver, BC, Canada | Suburban residential | 0.62 | 0.19 | Voogt and Oke (1997), Grimmond and Oke (1999) |
| Sacramento, CA | Suburban residential | 0.58 | 0.23 | Grimmond and Oke (1999) |
| Arcadia, CA | Suburban residential | 0.53 | 0.33 | Grimmond and Oke (1999) |
| Chicago, IL (#1) | Suburban residential | 0.47 | 0.28 | Grimmond and Oke (1999) |
| Chicago, IL (#2) | Suburban residential | 0.38 | 0.21 | Grimmond and Oke (1999) |
| San Gabriel, CA | Suburban residential | 0.36 | 0.14 | Grimmond and Oke (1999) |
| Miami, FL | Suburban residential | 0.35 | 0.16 | Grimmond and Oke (1999) |
| Tucson, AZ | Suburban residential | 0.33 | 0.19 | Grimmond and Oke (1999) |
| Los Angeles, CA | Mixed residential | 0.29 | 0.25 | Burian et al. (2002a) |

Figure 5.19 Plots practical frontal and planar density combinations of various city neighborhoods

By corresponding the findings of the present work with the densities of the cities indicated, the density combinations of the cities fall in the range where the lateral and top surfaces contribute the larger CHTC than that of the windward surface (Figure 5.20).

In addition, Figure 5.20 may be used to zone CHTC values of buildings based on the built type (land-use class) of the neighborhood. As indicated by the green colored oval circle, the lowest CHTC values correspond to buildings in downtown, i.e., relatively tall and large footprint structures. The red colored circle region of low frontal density and mid-to-high planar density corresponds to industrial neighborhoods that have CHTC value comparable or slightly larger than the windward values. These structures are large footprint but low blockage. The high planar density but mid frontal density zone, shown by the blue circle, in between the above two zones refer to the suburban residential neighborhoods. In this region, the CHTC for top and lateral surfaces is larger than that of the windward. The yellow circle near the mid-planar and low-and-mid frontal density range correspond to the mixed residential neighborhoods.

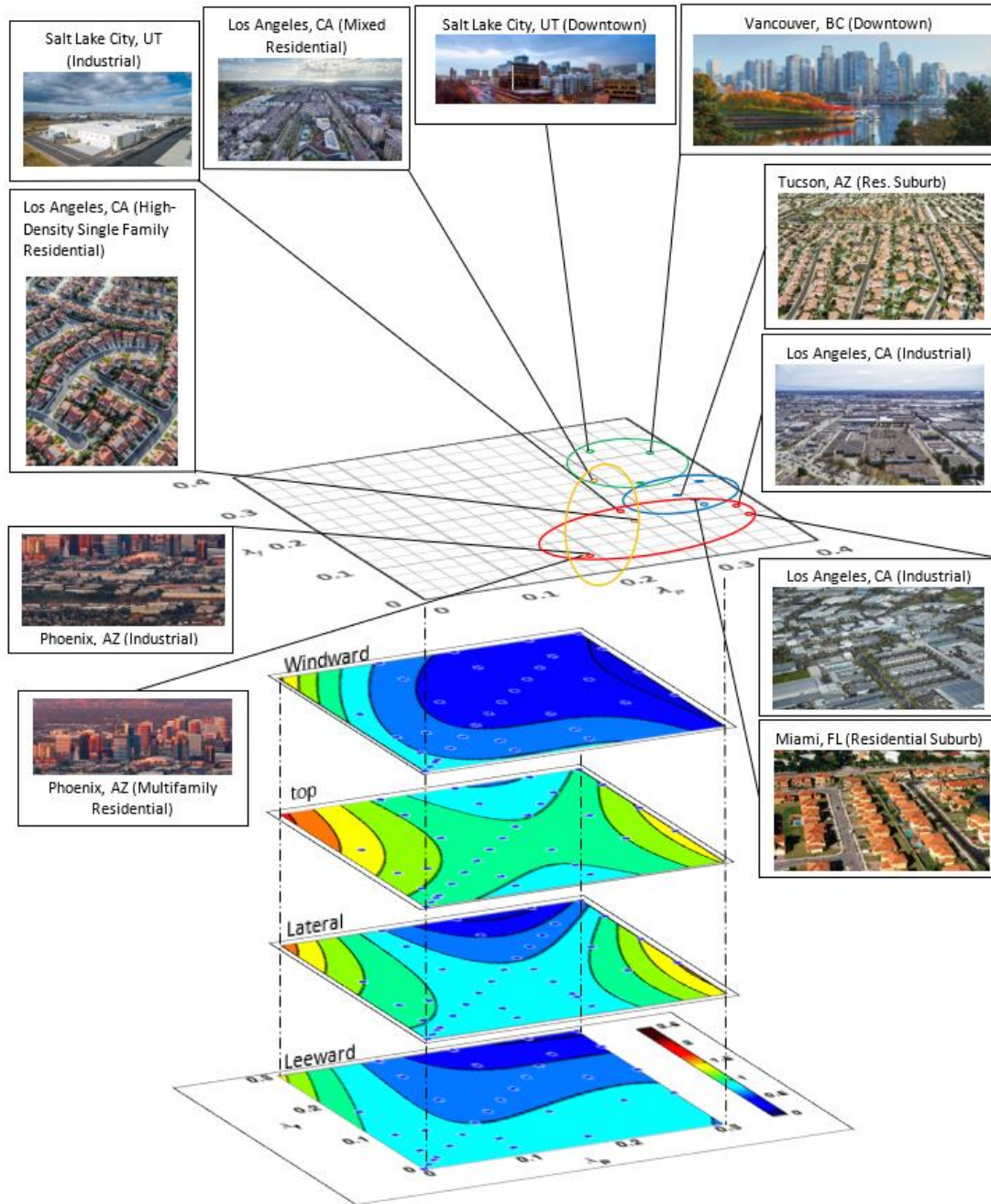


Figure 5.20 CHTC plots for each surface and distribution of density of urban neighborhoods (by land-use class)

5.6 Conclusion

The aim of the current work was to investigate the effect of broader changes in the urban surface form (built packing density) on the CHTC from surfaces of buildings. Previous studies found the importance of considering the presence of surrounding buildings in the estimation of CHTC from building surfaces in an urban place; through CFD simulation of uniform urban-like cubical obstacles. In this study, the obstacle size is modified to avoid the simplistic but useful approximation of the urban form by uniform cubical obstacles. The present modification presents a condition of unequal sets of frontal and planar densities.

The results of the study primarily reveal that CHTC is affected both by changes in planar as well as frontal densities. These changes might lead to up to 2.5 times higher or approximately an order of magnitude lower CHTC compared to the conventional U_{10} formulations (h_{iso} , which are mostly done without considering density effects). It is observed the least CHTC values for the windward, and leeward surfaces lie at higher planar densities, whereas the highest CHTC corresponds to the combination of the lowest planar and highest frontal densities. An increase in planar area density increases the CHTC at smaller frontal densities for top and lateral surfaces. The study shows the overall CHTC estimate from conventional models may have mostly been overestimated from the real values in city neighborhoods. Moreover, the general adoption of the windward CHTC as the dominant value among all surfaces may not be the case at higher planar densities, where most practical city neighborhood densities fall.

This research can be advanced by considering additional heterogeneity in the form of randomness to the urban form and by adopting transitions of density as in changes from the outskirts to the downtown.

References

Adamek, K., Vasan, N., Elshaer, A., English, E., and Bitsuamlak, G.T. (2017), Pedestrian level wind assessment through city development: A study of the financial district in Toronto, *Sustainable Cities and Societies*, 35:178-190.

Allegrini, J., Dorer, V. Carmeliet, J. (2012) Analysis of convective heat transfer at building façades in street canyons and its influence on the predictions of space cooling demand in buildings, *J. Wind Eng. Ind. Aerod.* 104:464-473.

Awol, D.A., Bitsuamlak, G.T., Tariku, F. (2017). Consistent analytical urban canopy layer velocity profile for dense building arrangement. *Americas Conference on Wind Engineering*, Gainesville, United States, 21-24 May 2017

Blocken, B., Defraeye, T. Derome, D. Carmeliet, J. (2009) High-resolution CFD simulations for forced convective heat transfer coefficients at the façade of a low-rise building, *Build. Environ.* 44:2396-2412.

Blocken, B., Stathopoulos, T., Carmeliet, J., Hensen, J.L.M. (2011) Application of computational fluid dynamics in building performance simulation for the outdoor environment: an overview, *Journal of Building Performance Simulation* 4:157-184.

Burian, S.J., Brown, M.J., and Linger, S.P. (2002a). Morphological analyses using 3D buildingdatabases: Los Angeles, California. LA-UR-02-0781, Los Alamos National Laboratory, Los Alamos, NM.

Burian, S.J., Velugubantla, S.P., and Brown, M.J. (2002b). Morphological analyses using 3D building databases: Salt Lake City, Utah. LA-UR-, Los Alamos National Laboratory, Los Alamos, NM.

Burian, S.J., Velugubantla, S.P., and Brown, M.J. (2002c). Morphological analyses using 3D building databases: Phoenix, Arizona. LA-UR-02-6726, Los Alamos National Laboratory, Los Alamos, NM.

Castro, I.P. (2017) Are Urban-Canopy Velocity Profiles Exponential? *Boundary-Layer Meteorol* 164(3):337–351. DOI 10.1007/s10546-017-0258-x

Chen, L., Hang, J., Sandberg, M., Claesson, L., Di Sabatino, S., Wigo, H. (2017) The impacts of building height variations and building packing densities on flow adjustment and city breathability in idealized urban models, *Build. Environ.*; 118:344-361

Cheng, H., Castro, I.P. (2002) Near-wall flow over urban-like roughness. *Boundary-Layer Meteorol* 104(2): 229–259

Chyu, M.K., Natarajan, V. (1991) Local heat/mass transfer distributions on the surface of a wall-mounted cube, *Trans. ASME J. Heat. Transf.* 113:851-857.

Cionco, R.M. and Ellefsen, R. (1998). “High resolution urban morphology data for urban wind flow modeling.” *Atmospheric Environment*, 32(1): 7-17.

- Coceal, O., Belcher S.E. (2004) A canopy model of mean winds through urban areas. *Q J Roy Meteorol Soc* 130(599):1349–1372
- Coceal, O., Thomas, T.G., Castro, I.P., Belcher, S.E. (2006) Mean flow and turbulence statistics over groups of urban-like cubical obstacles. *Boundary-Layer Meteorol* 121:491-519
- Defraeye, T., Blocken, B., Carmeliet, J. (2010) CFD analysis of convective heat transfer at the surfaces of a cube immersed in a turbulent boundary layer, *Int. J. Heat. Mass Transf.* 53:297-308.
- Emmel, M.G., Abadie, M.O., Mendes, N. (2007) New external convective heat transfer coefficient correlations for isolated low-rise buildings, *Energ Build.* 39:335-342.
- Evangelisti, L., Guattari, C., Gori, P., Bianchi, F. (2017) Heat transfer study of external convective and radiative coefficients for building applications, *Energ Build.* 151:429–438
- Franke, J., Hellsten, A., Schlünzen, H., Carissimo, B. (2011) The COST 732 Best Practice Guideline for CFD simulation of flows in the urban environment: a summary, *Int. J. Environ. Pollut.* 44 (2011) 419-427.
- Franke, J., Hellsten, A., Schlünzen, H., Carissimo B. (Eds.) (2007) Best practice guideline for the CFD simulation of flows in the urban environment, COST Office, Brussels, 3-00-018312-4.
- Grimmond, S. and Oke, T. (1999). “Aerodynamic properties of urban areas derived from analysis of surface form.” *J. Appl. Met.*, 38: 1262-1292.

- Hagishima, A., Tanimoto, J. (2003) Field measurements for estimating the convective heat transfer coefficient at building surfaces, *Build. Environ.* 38:873-881.
- Van Hooff, T., Blocken, B. (2010) On the effect of wind direction and urban surroundings on natural ventilation of a large semi-enclosed stadium, *Computers & Fluids* 39:1146-1155.
- Ito, N., Kimura, K., Oka, J. (1972) Field experiment study on the convective heat transfer coefficient on exterior surface of a building, *ASHRAE Trans.* 78:184-192.
- Jayamaha, S.E.G., Wijeysondera, N. E., Chou, S. K. (1996) Measurement of the heat transfer coefficient for walls, *Build. Environ.*, 31:399-407.
- Jürges, W. (1924) The heat transfer at a flat wall (*Der Wärmeübergang an einer ebenen Wand*), *Beihefte zum Gesundh.-Ing.* 1:19.
- Karava, P., Jubayer, C.M., Savory, E. (2011) Numerical modelling of forced convective heat transfer from the inclined windward roof of an isolated low-rise building with application to photovoltaic/thermal systems, *Appl. Therm. Eng.* 31:1950-1963.
- Launder, B., Reece, G. J., Rodi, W. (1975) Progress in the Development of a Reynolds Stress Turbulence Closure, *J Fluid Mech.* 68(3):537 – 566
- Leschziner, M.A. (1990) Modelling engineering flows with Reynolds stress turbulence closure, *J. Wind Eng. Ind. Aerodyn.* 35:21-47.
- Liu, J., Heidarinejad, M., Gracik, S. Srebric, J. (2015) The impact of exterior surface convective heat transfer coefficients on the building energy consumption in urban neighborhoods with different plan area densities, *Energ Build.* 86:449-463.

- Liu, J. Srebric, J. Yu, N. (2013) Numerical simulation of convective heat transfer coefficients at the external surfaces of building arrays immersed in a turbulent boundary layer, *Int. J. Heat. Mass Transf.* 61:209-225.
- Liu, Y., Harris, D.J. (2007) Full-scale measurements of convective coefficient on external surface of a low-rise building in sheltered conditions, *Build. Environ.* 42:2718-2736.
- Loveday, D.L., Taki, A.H. (1996) Convective heat transfer coefficients at a plane surface on a full-scale building façade, *Int. J. Heat. Mass Transf.* 39:1729-1742.
- Macdonald, R.W. (2000) Modelling the mean velocity profile in the urban canopy layer. *Boundary Layer Meteorol* 97(1):25–45
- Meinders, E.R. (1998) Experimental Study of Heat Transfer in Turbulent Flows over Wall Mounted Cubes, PhD thesis, Technische Universiteit Delft.
- Mirsadeghi, M., Costola, D., Blocken, B., Hensen, J.L.M. (2013) Review of external convective heat transfer coefficient models in building energy simulation programs: implementation and uncertainty, *Appl. Therm. Eng.* 56:134-151.
- Montazeri, H. Blocken, B. (2017) New generalized expressions for forced convective heat transfer coefficients at building facades and roofs, *Build Environ.* 119:153-168
- Montazeri, H., Blocken, B., Derome, D., Carmeliet, J., Hensen, J.L.M. (2015) CFD analysis of forced convective heat transfer coefficients at windward building facades: influence of building geometry, *J. Wind Eng. Ind. Aerodyn.* 146:102-116.

Moonen, P., Defraeye, T., Dorer, V., Blocken, B., Carmeliet, J. (2012) Urban physics: effect of the microclimate on comfort, health and energy demand, *Frontiers of Architectural Research* 1:197-228.

Murthy, B.N., Joshi, J.B. (2008) Assessment of standard k–e, RSM and LES turbulence models in a baffled stirred vessel agitated by various impeller designs, *Chem Eng Sci.* 63: 5468 – 5495

Oke, T.R. (1988) Street design and urban canopy layer climate. *Energ Build* 11(1-3)103-113

Palyvos, J.A. (2008) A survey of wind convection coefficient correlations for building envelope energy systems' modeling, *Appl. Therm. Eng.* 28:801-808.

Rodi, W. (1997) Comparison of LES and RANS calculations of the flow around bluff bodies, *J. Wind Eng. Ind. Aerodyn.* 69:55-75.

Sharples, S. (1984) Full-scale measurements of convective energy losses from exterior building surfaces, *Build. Environ.* 19:31-39.

Sparrow, E.M., Ramsey, J.W., Mass, E.A. (1979) Effect of finite width on heat transfer and fluid flow about an inclined rectangular plate, *J. Heat. Transf.* 101:199-204.

Stathopoulos, T., Wu, H. (1995) Generic models for pedestrian-level winds in built-up regions, *J. Wind Eng. Ind. Aerodyn.* 54-55:515-525.

Speziale, C.G. (1991) Analytical Methods for the Development of Reynolds-Stress Closures in Turbulence, *Annu Rev Fluid Mech.*, 23:107-157

Speziale, C.G. (1995). A review of Reynolds stress models for turbulent shear flows, NASA Langley Research Center, NASA Contractor Report 195054, ICASE Report No. 95-15

Tominaga, Y., Mochida, A., Yoshie, R., Kataoka, H., Nozu, T., Yoshikawa, M., Shirasawa, T. (2008) AIJ guidelines for practical applications of CFD to pedestrian wind environment around buildings, *J. Wind Eng. Ind. Aerodyn.* 96:1749-1761.

Vereecken, E., Janssen, H., Roels, S. (2018) A determination methodology for the spatial profile of the convective heat transfer coefficient on building components, *Indoor Built Environ.*, 27(4):512–527.

Voogt, J. and Oke, T. (1997). “Complete urban surface temperatures.” *J. Appl. Met.*, 36: 1117-1132.

Chapter 6

6 Conclusion and future work

6.1 Conclusion

A summary of the conclusions for the findings of the overall thesis is presented in this section. The thesis has four major contributions, and the following paragraphs discuss conclusions from each process.

A new analytical model for airflow in the canopy layer for sparse densities has been developed from first principles with few key assumptions. The one-dimensional model obtained for steady state, homogeneous turbulence in the roughness sublayer flow considers, for sparse canopies, the local Reynolds stress by the square of local space-averaged mean velocity does not vary much from the corresponding value at the top of the canopy. The model respects the near ground velocity predictions as per ABL considerations (dynamic scale velocity); and approaches the apparent log-law atmospheric boundary-layer profile at very low packing densities. These physical realities have not been demonstrated by previously developed one-dimensional analytical models.

The current analytical model is validated through comparison with experimental data obtained from the literature, and the sensitivity of the mean velocity profile is investigated against changes in the shear length scale (L_s/H), and the aerodynamic roughness length

scale (z_o/H). Both of these processes demonstrated the present model gives acceptable results.

These findings affect the evaluation of transport parameters in areas like convective heat transfer, mass and pollutant dispersion in vegetative and urban canopies, and other urban wind flow topics (PLW, wind energy, and wind-driven rain).

The presence of buildings around another building alters the local microclimate, from what it would have been if the building were in the open surroundings. The nature of aggregation or rarefaction of these buildings is parameterized by the packing density. Consequently, the need for accounting the impact of surrounding buildings on the evaluation of the convective heat transfer coefficient is argued. CFD's capability to enable full-scale simulations in several cases with better variable control is utilized.

Several packing density cases were chosen to encompass the three flow regimes, namely: isolated flow ($\lambda < 0.027$), interference flow ($0.027 < \lambda < 0.155$), and skimming flow options ($\lambda > 0.155$). The simulation process is validated against previous experimental and numerical work. In general, the RSM turbulence model used in the present simulation performed well in relation to the k-epsilon turbulence model, in approaching the experimental records.

The results of the present work revealed the external CHTC behaves differently in the three regimes, and on the building surfaces. There is a sharp change in CHTC for sparse canopy cases. The trend, in general, indicates an increase of CHTC with density for the top surface, a decrease of CHTC for all other surfaces with an increase in density. For denser canopies, the CHTC decreases gently as density increases for all surfaces. For the highest density

considered, the values of CHTC reduce by over 55%, 30%, and 40% from their corresponding benchmark values in the case of isolated building studies for Windward, Lateral and Leeward surfaces respectively. The top surface, however, has its peak CHTC in the middle of the isolated flow regime. The peak top surface CHTC value is 17% higher than the CHTC at the benchmark case or the value at the highest density (which are found very close). Lastly, a correlation of CHTC comprising both wind speed and urban packing density is presented.

A semi-analytical model is developed for the computation of the convective heat transfer coefficient from buildings in an urban setting. The model is derived based on fundamental empirical conclusions found in literature, and an analytical mean velocity profile model developed as part of this work (chapter 2). The results of the current model are verified against CFD simulation data reported earlier (chapter 3). Considering the assumptions made, the agreements achieved for both windward and top surfaces of the building are acceptable. The sensitivity of a recurring parameter in the model, i.e., Jensen number (H/z_o), is conducted, and its effect on CHTC is found to be minimal for very small changes.

With an aim to investigate the effect of broader changes in the urban surface form (built packing density) on the CHTC from surfaces of buildings. The obstacle size is modified to avoid the, too simple but useful, approximation of the urban form by uniform cubical obstacles. The modification presents a condition of unequal sets of frontal and planar densities.

The results of the study primarily reveal that CHTC is affected both by changes in planar as well as frontal densities. These changes might lead to up to 2.5 times higher or approximately an order lower CHTC compared to the conventional U_{10} formulations (h_{iso} ,

which are mostly done without considering density effects). It is observed that the least CHTC values for the windward and leeward surfaces lie at higher planar densities, whereas the highest CHTC corresponds to the combination of the lowest planar and highest frontal densities. An increase in planar area density increases the CHTC at smaller frontal densities for top and lateral surfaces. The study shows the overall CHTC estimate from conventional models may have mostly been overestimated from the real values in city neighborhoods. Moreover, the general adoption of the windward CHTC as the dominant value among all surfaces may not be the case at higher planar densities, where most practical city neighborhood densities fall.

The main contributions of the overall research are:

- Convective heat transfer is affected by the built microclimate, buildings packing density.
- Convective heat transfer coefficient behaves differently in different roughness regimes.
- Estimation of CHTC from an isolated cube studies overestimates convective heat loads for windward and leeward faces; may underestimate the value from lateral and top surfaces.
- A new canopy (local) scale velocity may be used to characterise the microclimatic velocity field near buildings.
- CHTC may be expressed by a local velocity scale at the canopy to obtain density effects.
- Both planar and frontal densities of canopies influence CHTC.

- Large frontal but low planar area (slender) building stock exhibit the largest CHTC (for all orientation).
- Large frontal and large planar (large foot print) buildings exhibit the lowest CHTC for at least windward and leeward surfaces.
- The windward CHTC may not be the dominant value as is mostly considered. CHTC from lateral and top surfaces may dominate in the contribution, for mid-frontal and large-planar densities.
- Convectonal isolated block studies have been dealing with the low-density extreme of density pair matrix, where real neighbourhoods hardly exist. CHTC zone may assigned for various land-use class designated areas in various cities.

6.2 Future work

This new analytical canopy wind flow model can be further investigated within topics that include the determination of displaced log-law parameters, improvement in the boundary-layer profile through better turbulent mixing-length scale representation, roughness, or canopy density transitions, etc. An improved version of this model is being considered for a wider range of packing densities.

Both analytical mean velocity profile and the CFD simulation has been obtained for building like surfaces of homogeneous or quasi-heterogeneous bluff bodies. Additional simulations at very large densities may be conducted to address the applicability of the model to a broader range.

The real heterogeneity of the urban form (the randomness of variability in height) has not yet been investigated, and thus, the results of the current model remain better estimations,

only to such conditions. This research can be advanced by considering additional heterogeneity in the form transitions of density, as in changes from the outskirts to the urban downtown.

Appendices

Appendix A: Reynolds Stress Transport Equation

The transport equation for the Reynolds stress tensor \mathbf{R} is:

$$\frac{\partial}{\partial t}(\rho\mathbf{R}) + \nabla \cdot (\rho\mathbf{R}\bar{\mathbf{V}}) = \nabla \cdot \mathbf{D} + \mathbf{P} - \frac{2}{3}\mathbf{I}\gamma_M + \underline{\boldsymbol{\varphi}} + \rho\underline{\boldsymbol{\varepsilon}} + \mathbf{S}_R$$

where: ρ is the density, $\bar{\mathbf{V}}$ is the mean velocity, \mathbf{D} is the Reynolds Stress Diffusion, \mathbf{P} is the Turbulent Production, \mathbf{G} is the Buoyancy Production, \mathbf{I} is the identity tensor, γ_M is the Dilatation Dissipation, $\underline{\boldsymbol{\varphi}}$ is the pressure strain tensor, $\underline{\boldsymbol{\varepsilon}}$ is the turbulent dissipation rate tensor, \mathbf{S}_R is a source term.

For the Linear Pressure Strain models, the dissipation is simply:

$$\underline{\boldsymbol{\varepsilon}} = \frac{2}{3}\varepsilon\mathbf{I}$$

Seven equations must be solved (as opposed to the two equations of a K-Epsilon or a K-Omega model): six equations for the Reynolds stresses (symmetric tensor) and one equation for the isotropic turbulent dissipation ε .

Reynolds Stress Diffusion

The following simple isotropic form of the turbulent diffusion is adopted, i.e.

$$\mathbf{D} = \left(\mu + \frac{\mu_t}{\sigma_k}\right)\nabla\mathbf{R}$$

where: μ is the dynamic viscosity, σ_k is a Model Coefficient.

The turbulent viscosity μ_t is computed as: $\mu_t = \rho C_\mu \frac{k^2}{\varepsilon}$

where: C_μ is a Model Coefficient.

The turbulent kinetic energy k is defined as:

$$k = \frac{1}{2} \text{tr}(\mathbf{R})$$

where $\text{tr}(\mathbf{R})$ is the trace of the Reynolds stress tensor (sum of the squares of the diagonal terms).

Turbulent Production

The turbulent production is obtained directly, without recourse to modeling as follows:

$$\mathbf{P} = -\rho(\mathbf{R} \cdot \nabla \bar{\mathbf{V}}^T + \nabla \bar{\mathbf{V}} \cdot \mathbf{R}^T)$$

Isotropic turbulent dissipation rate (ε) equation

The isotropic turbulent dissipation rate is obtained from a transport equation analogous to the K-Epsilon model (and with identical boundary conditions):

$$\frac{\partial}{\partial t}(\rho\varepsilon) + \nabla \cdot (\rho\varepsilon\bar{\mathbf{V}}) = \nabla \cdot \left[\left(\mu + \frac{\mu_t}{\sigma_\varepsilon} \right) \nabla \varepsilon \right] + \frac{\varepsilon}{k} \left[C_{\varepsilon 1} \left(\frac{1}{2} \text{tr}(\mathbf{P}) \right) - C_{\varepsilon 2} \rho \varepsilon \right]$$

where: σ_ε , $C_{\varepsilon 1}$, and $C_{\varepsilon 2}$ are Model Coefficients.

Dilatation Dissipation Rate

The dilatation dissipation γ_M is modeled as:

$$\gamma_M = \rho C_M \frac{k\varepsilon}{c^2}$$

where: C_M is a Model Coefficient, c is the speed of sound.

Table A.1: Model Coefficients

| <i>Coefficient</i> | <i>Linear Pressure Strain Two Layer</i> |
|----------------------|---|
| σ_k | 0.82 |
| σ_ε | 1 |
| C_M | 2 |
| C_s | 0.2 |
| $C_{\varepsilon 1}$ | 1.44 |
| $C_{\varepsilon 2}$ | 1.92 |
| C_μ | 0.09 |

Appendix B

Curriculum vitae

Name: **Anwar Demsis Awol**

Post-secondary Education and Degrees: The University of Western Ontario
 London, Ontario, Canada
 2013-2019
 Ph.D.
 Civil and Environmental Engineering

Indian Institute of Technology Bombay (IITB)
 Mumbai, India
 2006 – 2008
 Master of Technology
 Thermal and Fluid Engineering

| | |
|--------------------------|--|
| | Arba Minch University Arba Minch, Ethiopia 1997-2002 B.Sc. Mechanical Engineering |
| Honor and Awards: | Western Engineering Scholarship Ontario Center of Excellence through Early Career Award and SOSCIP grants 2013 – 2019 Alan G. Davenport award for excellence Civil and Environmental Engineering, University of Western, London, Canada 2014 |
| Related Works: | Research and Teaching Assistant Western University 2013- 2019 Lecturer and Research Assistant Adama University 2006 - 2013 |
| Publications: | <ul style="list-style-type: none"> ▪ Awol, D.A., Bitsuamlak, G.T., Tariku, F. (2019) Numerical estimation of the external convective heat transfer coefficient for buildings in an urban-like setting. Building and Environment 169:106557 ▪ D. A. Awol, G. T. Bitsuamlak, F. Tariku (2019). A More Reliable Estimate For External Convective Heat Transfer Coefficient From Building Surfaces in an Urban-Setting. CFD Society of Canada Conference, London, Canada, 2-5 June 2019. |

- Awol, D.A., Bitsuamlak, G.T., and Tariku, F.(2018). Realistic Analytical Model for Air Flow in Canopies of Wide Range of Packing Densities. Submitted to: Journal of Boundary Layer Meteorology.
- Awol, D.A., Bitsuamlak, G.T., and Tariku, F.(2017). Consistent analytical urban canopy layer velocity profile for dense building arrangement. 2017 Americas Conference on Wind Engineering, Gainesville, United States
- Anwar Demsis Awol, William Lubitz & Girma Bitsuamlak. (2014), External Pressure Distribution and Wind-driven Ventilation of a Venlo Multi-span Greenhouse. CSME Conference 2014, Toronto, Canada. No. 216.
- Demsis, A., Verma, B., Prabhu, S. V., & Agrawal, A. (2009). Experimental determination of heat transfer coefficient in the slip regime and its anomalously low value. Physical Review E, 80(1), 016311.
- Verma, B., Demsis, A., Agrawal, A., & Prabhu, S. V. (2009). Semiempirical correlation for the friction factor of gas flowing through smooth microtubes. Journal of Vacuum Science & Technology A: Vacuum, Surfaces, and Films, 27(3), 584-590.
- Demsis, A., Verma, B., Prabhu, S. V., & Agrawal, A. (2010). Heat transfer coefficient of gas flowing in a circular tube under rarefied condition. International Journal of Thermal Sciences, 49(10), 1994-1999.

- Demsis A., Prabhu, S. V., & Agrawal, A. (2010). Influence of wall conditions on friction factor for flow of gases under slip condition. *Experimental Thermal and Fluid Science*, 34(8), 1448-1455.

- Anwar Demsis Awol, (2008), Experimental study of rarefied gas flow with application to microchannel. Indian Institute of Technology Bombay, M. Tech. Thesis 2008.